Fragmentation Dynamics of Triatomic Molecules in Femtosecond Laser Pulses Probed by Coulomb Explosion Imaging

by

Reza Karimi

A thesis
presented to the University of Waterloo
in fulfillment of the
thesis requirement for the degree of
Doctor of Philosophy
in
Physics

Waterloo, Ontario, Canada, 2013

AUTHOR'S DECLARATION

I hereby declare that I am the sole author of this thesis. This is a true copy of the thesis, including any required final revisions, as accepted by my examiners.

I understand that my thesis may be made electronically available to the public.

Abstract

In this thesis we have utilized few-cycle pulses in the range 10^{-15}s, to initiate CE to allow us to image the structure, dynamics, and kinetics of ionization and dissociation of triatomic molecules. We have made a series of measurements of this process for CO_2 and N_2O, by varying the laser pulse duration from 7 to 500 fs with intensity ranging from 2.5×10^{14} to 4×10^{15} (W/cm^2), in order to identify the charge states and time scales involved. This is a new approach in CEI introducing a multi-dimensional aspect to the science of non-perturbative laser-molecule interaction. We refer to this approach as FEmtosecond Multi-PUlse Length Spectroscopy (FEMPULS). The use of a time and position sensitive detector allow us to observe all fragment ions in coincidence. By representing the final fragmentation with Dalitz and Newton plots, we have identified the underlying break up dynamics. Momentum conservation has been used to extract the correlated fragment ions which come from a single parent ion. This is achieved by considering that the total momentum of all correlated fragments must add up to zero.

One of the main outcomes of our study is observation of charge resonance enhanced ionization (CREI) for triatomic molecules. In the case of CO_2, we found that for the 4+ and higher charge states, 100 fs is the time scale required to reach the critical geometry R_{CO}= 2.1Å and Θ_{OCO} =163º (equilibrium CO_2 geometry is R_{CO}= 1:16Å and Θ_{OCO} =172º. The CO_2^{3+} molecule, however, appears always to begin dissociation from closer than 1.7 Å indicating that dynamics on charge states lower than 3+ is not sufficient to initiate CREI. Finally, we make quantum ab initio calculations of ionization rates for CO_2 and identify the electronic states responsible for CREI. Total kinetic energy (KER) has been measured for channels (1, 1, 1) to (2, 2, 2) and it was found that the (1, 1, 1) channel is not Coulombic, while (2, 2, 2) channel is very close to Coulombic (KER close to 90% of the coulombic potential).

As another outcome of our study, for the case of N_2O, we observed for the first time that there are two stepwise dissociation pathways for N_2O^{3+}: (1) $N_2O^{3+} \rightarrow N^+ + NO^{2+} \rightarrow N^+ + N^+ + O^+$ and (2) $N_2O^{3+} \rightarrow N_2^{2+} + O^+ \rightarrow N^+ + N^+ + O^+$ as well as one for $N_2O^{4+} \rightarrow N^{2+} + NO^{2+} \rightarrow N^{2+} + N^+ + O^+$. The N_2^{2+} stepwise channel is suppressed for longer pulse length, a phenomenon which we attribute to the influence which the structure of the 3+ potential has on the dissociating wave packet propagation. Finally, by observing the KER for each channel as a function of pulse duration, we show the increasing importance of CREI for channels higher than 3+.

Acknowledgements

I would like to express my humble gratitude to my supervisor Professor Joseph Sanderson for supporting me in all steps of my Ph.D. studies. Not only did I benefit from his knowledge but also I learnt a lot from his personality.

I would like to thank my Ph.D. advisory committee Professor W. K. Liu, Professor Walter Duley, Professor Donna Strickland, and Professor Marcel Nooijen for their guidance during my studies.

I am really grateful for the support and help of my family, particularly my wife, whether she was here with me or back in my home country taking care of our children, patiently waiting for me to finish my thesis.

I appreciate great help of all my group mates especially Benji Wales who helped me the most during this time.

Moreover, I thank Professor Francois Légaré for providing the ALLS facility and for helping me with his precious ideas and scientific support.

I appreciate the tireless effort of the machine shop group with leadership of Harmen Vander Heide and technicians specially Peter Kessel. Also I appreciate the tireless effort of the electronics group with leadership of Jacek Szubra.

I thank all department of physics' staff particularly Judy McDonnell for kindly assisting me with administrative tasks.

And finally I thank all of my friends and relatives who helped me in every possible way to fulfill my degree successfully.

Dedication

This work is dedicated to my mother Batool, my wife Zohreh, my son Ali, and my daughter Sara.

Table of Contents

List of Figures

List of Acronym

CEI	Coulomb Explosion Imaging
FEMPULS	FEmtosecond Multi-PUlse Length Spectroscopy
CREI	Charge Resonance Enhanced Ionization
KER	Total Kinetic Energy Released
HCI	Highly Charged Ion
PSD	Position and time-Sensitive Detector
TOF	Time of Flight
CAMAC	Computer Automated Measurement and Control
MCSCF	Multi-Configurational Self-Consistent-Field
MOLPRO	A package of *ab initio* programs
MBWC	Modified Backgammon Weighted Capacitor
ECR	Electron Cyclotron Resonance
MPI	Multiphoton Ionization
TI	Tunneling Ionization
OTBI	Over the Barrier Ionization
TDSE	Time Dependent Schrödinger Equation
CR	Charge-Resonance
MO	Molecular Orbital
MRMI	Mass-Resolved Momentum Imaging
TOF	Time of Flight
TOFMS	Time of Flight Mass Spectrometer
GAMESS	General Atomic and Molecular Electronic Structure System
PES	Potential Energy Surface
CPA	Chirped Pulse Amplification
MCP	Micro Chanel Plate
ALLS	Advanced Light Laser Source
TDC	Time to Digital Converter
DLD	Delay Line anode Detector
CFD	Constant Fraction Discriminator
TDDFT	Time-Dependent Density Functional Theory

SAOP	statistical average of orbital potential
HOMO	Highly Occupied Molecular Orbital
LUMO	Low Unoccupied Molecular Orbital
RCAP	Raman Chirped Adiabatic Passage
ARP	Adiabatic Rapid Passage
TMU	Tokyo Metropolitan University

Chapter 1
Introduction

The fields of spectroscopy and quantum mechanics have been extraordinarily successful in advancing our basic knowledge of molecular structure over the past nearly hundred years. The advances can perhaps best be summed up by the body of work published by the Nobel Prize winning scientist Gerhard Herzberg such as *Molecular Spectra and Molecular Structure*: Infrared and Raman spectra of polyatomic molecules [1–3]. Nevertheless the science of directly mapping molecular structure independently of spectroscopy and with particular emphasis on single molecule imaging has become increasingly active particularly since the advent of high intensity ultrafast laser pulses [4].

The field began in the 1970s, when Coulomb repulsion between the nuclei of a molecule whose electrons have been stripped away, was introduced as the basis of the modern technique. Depending on the type of electron stripping and consequent ionization, three major techniques have emerged. Chronologically, the beam foil technique was the first direct method of molecular imaging which was based on the stripping of the electrons of a high energy molecular beam passing through a beam foil. However, this technique requires very expensive facilities to achieve molecular beams with the MeV energy necessary to progress the experiments. Later on, a more feasible method employing highly charged ions (HCI) was introduced. This technique was based on ionization of the target molecules using a highly charged ion beam, e.g. Ar^{8+}, colliding with the target molecules. This technique is much more effective in the determination of the molecular structure than beam foil, because the molecule under study is not ionized and accelerated to high speed. Additionally, different ionization mechanisms can be used by choosing the type of ion and collision energy. In parallel, the technique of laser assisted coulomb explosion has been introduced and is making rapid development. The advantage of this technique is that it is possible to control the laser pulse very precisely and additionally generate multiple pulses following one another to pump and probe a molecule. Both of these properties give the promise of measuring the timescales of specific dynamics.

In the early 1990's, development of intense short pulse laser systems led to laser pulse lengths of the range of femtoseconds (10^{-15}s). This range is comparable to the vibrational period of molecules (10^{-14} s) and smaller than the range of rotational movement of a molecule which is normally on the order of 10^{-12}s. Similar to a simple photographic camera, in which a longer shutter speed than an

object's movement gives blurry images, it is important to image molecules with pulses which are shorter than the timescale of molecular movement. The use of laser beams of very short pulse (7fs) for ionization of molecules allows more accurate determination of the molecular structure immediately after ionization, in which the nuclei can be deemed nearly frozen. That is, the ionized molecule is really close to its neutral ground state geometry. This technique has many advantages over previous mentioned techniques. For instance, the ionization process of the target molecule can be tailored by adjustment of laser pulse duration. Also, the most precious and unique advantage of this technique is the ability to portray molecular dynamics during an ionization process. In addition to molecular structure, molecular dynamics of previously studied simple diatomic (H_2, N_2) and straight symmetric triatomic (CS_2, CO_2) molecules have been extensively elucidated. Although molecular structure and dynamics of asymmetric triatomic molecules have been addressed, there exist more subtle questions on which light can be shed for N_2O. Furthermore, there are only a few systematic studies addressing the ionization processes of polyatomic molecules (such as C_2H_2), offering them as an almost pristine field of study for the emerging new generation of the laser systems, such as those generating free electron laser and attosecond pulse duration.

In this thesis, we have made a series of measurements of the ionization and fragmentation of the asymmetric triatomic molecule N_2O and the symmetric but isoelectronic molecule CO_2, in intense femtosecond laser radiation. The laser pulse duration was varied from 7fs to 500fs and time and position sensitive detection was utilized to observe all fragments in coincidence. Dalitz and Newton plots were utilized to represent final dissociation geometry and identify the underlying break up dynamics. The content of the thesis is organized in 6 chapters including this chapter. Chapter 2 reviews the development of Coulomb Explosion techniques for molecular imaging with particular emphasis on the underlining theory and experimental achievements in the field of laser assisted coulomb explosion. Chapter 3 presents the experimental set-up, data acquisition, and data analysis techniques which have been used in our studies. In chapter 4 charged resonance enhanced ionization (CREI) of the CO_2 molecule has been theoretically and experimentally studied through laser assisted coulomb explosion. Total kinetic energy released for different ionization channels ranging from (1, 1, 1) to (2, 2, 2) has been obtained and used to identify the doorway state to CREI. In chapter 5 we study the ionization process of N_2O molecule with the same approach but focus more on the behavior of the diverse break up processes associated with the asymmetric system. Using Dalitz and Newton plots, we have been able to observe the metastable fragmentation of

$N_2O^{3+} \rightarrow N^+ + NO^{2+}$, and the metastable fragmentation of $N_2O^{3+} \rightarrow N_2^{2+} + O^+$ and their behavior as a function of pulse length. The difference between total kinetic energy released for channels (2, 1, 1) and (1, 2, 1), which were not measured before, have also been made accessible by the use of Dalitz plots. In chapter 6 the outcomes of the experiments are summarized and possible future work is discussed.

Chapter 2
Coulomb Explosion Imaging Techniques

2.1 Introduction

In Coulomb explosion imaging (CEI), the electronic cloud of a species is stripped away from its nuclei. Accordingly, the Coulomb repulsion between nuclei leads to disintegration of the original molecule into fragment ions[5–26]. Depending on the method of electron stripping, Coulomb explosion techniques are divided in three major categories: Beam-foil, HCI impact, and laser induced Coulomb explosion. The mechanism of removal of electrons has been explained in each related category. In this chapter we briefly explain the first two methods and then elaborate the laser induced method which will be the subject of the rest of this thesis.

2.2 Beam-foil

The first CEI has been demonstrated by using the Beam-foil technique [5]. In this technique, small molecular ions moving with $\sim 10^6$ eV energy pass through a thin foil [5–7]. In this experiment, all ionization took place within ~100 as. Measured momenta of fragment ions resulting from multiple ionization of the parent ion were used to reconstruct the initial structure of the molecule before explosion. The interaction potential of the charged particles during the explosion is crucial for the reconstruction process. Usually the Coulomb potential is used to ease the process.

Beginning in the 1970's, Zeev Vager and coworkers from the Weisman institute, carried out a set of experiments to map the molecular structure of targets such as H_2^+, CH_4^+, H_2O^+, N_2^+, $C_2H_3^+$ C_2H_2, H_2 C_3^+ and HeH molecules [6–10]. The experiments were carried out at Argonne National Laboratory. In the case of CH_4^+ [8], an accelerated projectile with 2% of the velocity of light was guided and passed through a molecularly thin aluminum foil (30Å). Using the Bohr's theory approach, the authors discussed the electron stripping mechanism from the projectile and concluded that if the orbital velocity of an electron is less than that of the projectile, the electron would be stripped off.

The time required for passing of the projectile through the solid film and consequently stripping (10^{-16}s) is less than the timescale of the vibrational (10^{-14}s) and rotational motions (10^{-12}s) of the nuclei. Thus, the binding electrons will be stripped away within the solid film. The electron-stripped ions then experience Coulomb explosion when they come out of the thin solid foil. The simple schematic view of this method is presented in Figure 2-1.

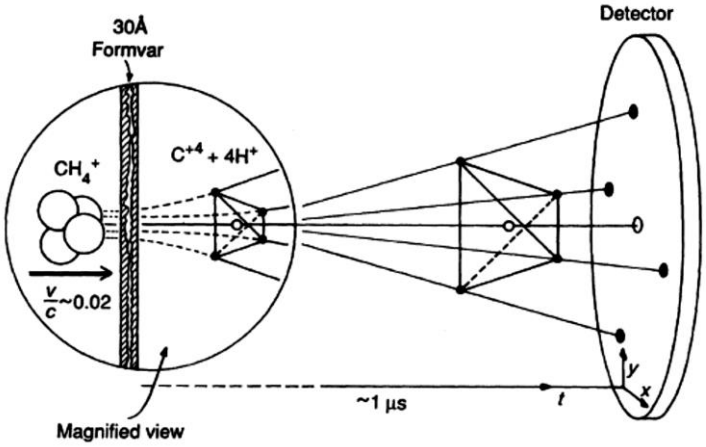

Figure 2-1 A schematic view of beam foil technique CE experiment, molecular beam, thin solid film, and detector (Reprinted with permission from [8]).

Once explosion happens for the ions, the position-time sensitive detector (PSD) is used to detect the fragment ions. The PSD measures the position (x, y) and the time of flight (TOF) t of all fragment ions. Using x, y, and t, the 3D momentum of the fragment ions was measured and employed to infer the structure of the projectile molecules before explosion. Rather than representing bond lengths and bend angles, the authors plotted CH_4^+ geometry in velocity space, indicating two asymmetric geometries coexist with the expected tetrahedral shape of CH_4. This experiment, although a highly accomplished achievement, demonstrates the inherent problem with the method. That is, it requires the target molecule to be an ion, which may have inherently different structure to the neutral molecule. This and the rarity and cost of ion storage rings, has limited the spread of this method. Nevertheless the authors have used the necessity of studying ions, to their advantage to continue to make progress into the 2000s. In some cases they neutralized the ion, such as in [9] where the negatively ionized acetylene molecule was neutralized by a pulse from an IR laser before the beam foil. This allowed the non-decaying vinylidene structure, characterized by hydrogen migration to the opposite end of the molecule to be observed. Further work on H_3^+ [10] showed that the technique could be used to observe vibronic cooling which takes place in the storage ring, making the Coulomb imaging method an important diagnostic for such systems. The random nature of the collision also means that the stationary state of the small molecules can be measured. It cannot easily look at dynamics.

2.3 Highly Charged Ion (HCI) Impact

The HCI technique is based upon collision of a highly charged ion e.g. Ar^{q+} or Xe^{q+}, (where q can be as high as the number of electrons in the neutral projectile) and a molecular gas target. Figure 2-2 shows a schematic view of an HCI impact process on an arbitrary atom. In this process, some of atom B electrons are transferred to the projectile beams of kV to MV HCI, in this case Ar^{q+}. Afterwards, some of the electrons captured by the HCI are kicked out in the form of Auger electrons. The resultant Auger electrons are usually used as a trigger for the experimental apparatus to indicate the detection of the fragment ions, in this case ionized B^{n+}.

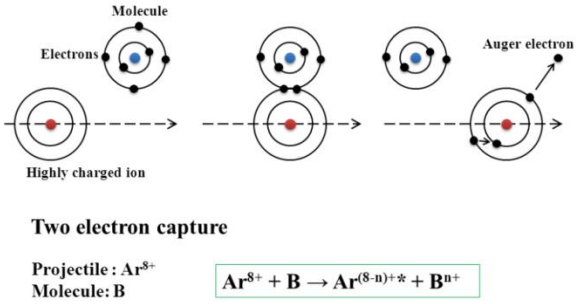

Figure 2-2 Schematic view of an HCI impact process on an arbitrary atom

The fragmentation dynamics of a collision-induced CE process is dominated by the repulsion between the resultant positive ions. As with the beam-foil method, Coulombic forces between point charges are used as a coarse basis for geometry reconstruction using the KER of the fragment ions. The projectile and details of dissociation processes are not taken into account in this model. The rotational and vibrational periods of the molecule is much greater than instantaneous character of the molecule and HCI impact interaction processes ($\tau_{col} < 10^{-17}$s), which is the main basis for this method. In fact, a complete fingerprint of the molecule at the time of fragmentation can be obtained by kinematically complete measurements, which is the process of calculating the momenta of all particles involved in the measurement.

In the late 1980's and early 1990's, a substantial amount of experimental studies on HCI impact primarily with atomic targets were carried out by mostly three groups: the groups of Horst Schmidt Böcking (University of Frankfurt, Frankfurt, Germany) and coworkers at the UNILAC accelerator of

GSI, Darmstadt in Germany, the group of Lutz at Bielefeld university, Bielefeld Germany [11–15], and CIMAP group at Université de Caen-Basse Normandie, Caen, France [27]. The experimental setup (except the source of interaction), data acquisition and analysis methods were innovative and shared certain elements. Thus, in this section we only introduce the common features of these developments highlighting the important details.

Figure 2-3 represents a schematic view of an experimental set-up for HCI impact process [11]. After ionization of the molecule, fragment ions and electrons generated in the collision of an HCI beam with a gas target molecule are guided to the detector plane. This is done by a DC electric field (so called Wiley Mclarren) [29]. In some cases, there exists a field-free area in order to enhance the resolution of the spectrometer. The Channeltron is responsible for detection of electrons and the time-position-sensitive detector on the other side is responsible for detection of positive ions. A pair of multi-capillary plates (MCPs) is combined with an etched crossed-wire delay line consisting of independent *x* and *y* wires and gives independent positional information through individual preamplifiers and a CAMAC interface to a PC. The benefit of this etched crossed-wire anode structure is the possibility of simultaneous detection of particles arriving at the same time (although this is not necessarily practical). Then, each position on the detector (x_i, y_i) and the time-of-flight t_i corresponds to a positive fragment triggered by the first recorded Auger electron signal (the time of the electron detection is used as a start trigger).

The initial velocity vectors of the correlated fragments can be calculated through measured positions (x_i, y_i) and flight times t_i using classical mechanics. The detailed mechanism of data acquisition and analysis is similar to the methods of the earlier Beam-foil experiments. Momentum vectors are generated for each particle detected in coincidence [12], [30].

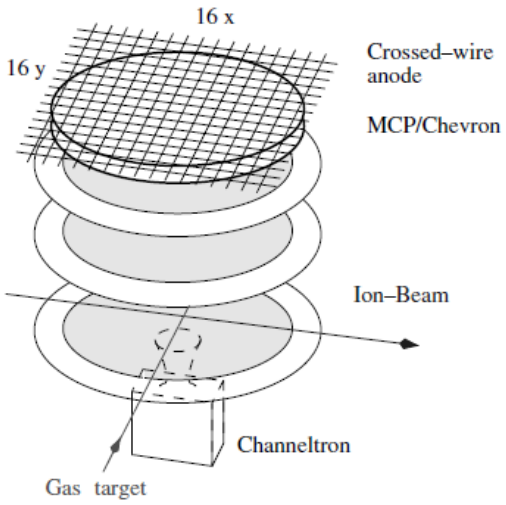

Figure 2-3 Schematic view of the CE experiment using HCI impact (Reprinted with permission from [11])

There are a large number of parameters to be used in the complete analysis of the results from HCI impact CE process. Among them, B. Siegmann and coworkers employed three independent parameters of KER and the angles χ and θ_v in velocity space to analyze the fragmentation dynamics of a three-body dissociation reaction [11], [15], [28]. Figure 2-4 represents the schematic geometry of the explosion of the multiply ionized CO_2 molecule; χ is the angle between the relative velocity v_{OO} of the two terminal ions (O^{q+}- O^{r+}) and the velocity of the central ion (v_C) and θ_v stands for the angle between the two relative velocities v_{CO} (O^{q+} –C^{P+}). Employing θ_v and χ parameters they recognized whether the molecule experiences bending and whether the bonds dissociate in the same time in either a concerted reaction or in sequential process. In the latter process the original molecule breaks up into two fragments, initially, followed by another dissociation process which occurs at such distance that the original fragments hardly interact anymore ($CO_2^{(q+p+r)+} \rightarrow CO^{(q+p)+} + O^{r+} \rightarrow O^{q+} + C^{p+} + O^{r+}$).

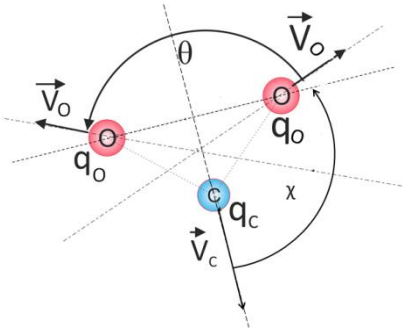

Figure 2-4 Schematic view definition of the measured parameters χ and θ_v in velocity space

As water is a comparatively simple molecule and approximately only the O fragment has an electronic structure, U. Werner and co-workers [16] conducted a series of CE experiments for the first time using ionization with H^+, He^+ (100keV) and O^{q+} (126keV) projectiles.

In the case of H^+ and He^+ they observed the break up of H_2O into $H_f^+ + H_b^+ + O^+$ and $H_f^+ + H_b^+ + O^{2+}$; and in the case of O^{6+} and O^{7+} projectiles complete fragmentation up to $H^+ + H^+ + O^{5+}$ was observed. CE model was found inadequate to elucidate the obtained energy and angular spectra. Using ab initio multi-configurational self-consistent field (MCSCF) calculations a better accordance was achieved. In this calculations several molecular states of the fragmenting HCI of $H_2O^{(q+2)+}$ were taken into account. Using MOLPRO code [31] they calculated the nine lowest molecular states of intermediate H_2O^{3+} and H_2O^{4+} [16].

Similar to the work by U. Werner and co-workers, H_2O in collisions with 5.9 MeV $Xe^{17,\ 18,\ 48+}$ ions has been studied by B. Siegmann and coworkers [28] using the same position and-time-sensitive detector. Complete dissociation with a total charge of up to 8+ were observed which was higher than previously observed for the collisions with ≃100 keV H^+ and He^+ which was only able to produce total charge up to 4+ [16].

Figure 2-5 shows the results of their experiments where the variation of signal intensity is depicted against three characteristic parameters of KER, cosχ, and θ_v for (1, 1, 1) channel fragment ions. The vertical lines indicate the excited state in H_2O^{3+}. As can be seen in Figure 2-5 the experimental KER is broader than the Coulombic spectrum and it is also independent of the projectile charge state.

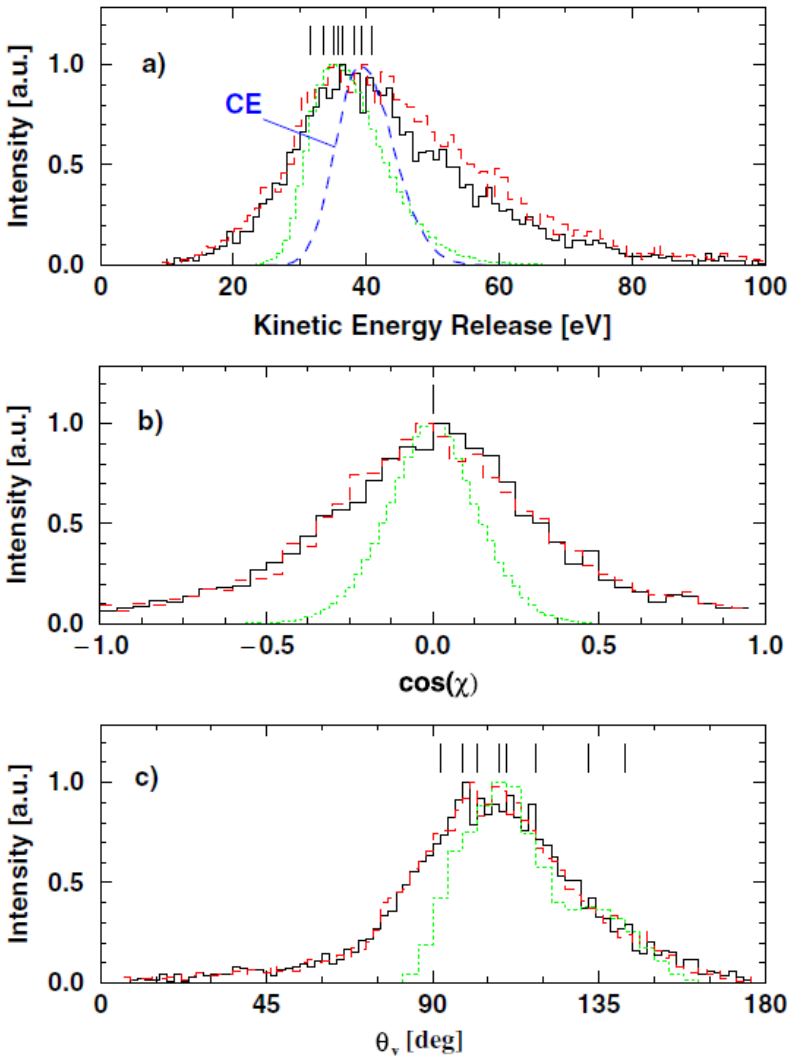

Figure 2-5 a) KER, b) cosχ, and c) θ_v distribution of $H^+ + H^+ + O^+$ channel. Solid line Shows the 5.9 MeV u^{-1} Xe^{17+} and red dashed line shows Xe^{43+}, and green dotted line shows the MCSCF calculations. The excited states in the H_2O^{3+} molecular ion is represented by the vertical lines. Blue dashed line corresponds to the Coulomb explosion model (Reprinted with permission from [16]).

Particularly in Figure 2-5 a), there is an obvious deviation from the pure CE model prediction in the position and width of kinetic energy spectra. Also, as the spectra for Xe^{17+} and Xe^{43+} are similar, the distribution cannot be attributed to the projectile influence. Another conclusion which can be drawn from this figure is the strong dependency of KER on the electronic configuration of the O^{q+} ion. Figure 2-5 b) depicts experimental results compared with MCSCF prediction for a simultaneous break

up. As the water molecule is symmetrical, all MCSCF states result in symmetric curves peaked at around 90º. Therefore, the broadness of the experimental curve cannot be attributed to influences of stepwise processes. The Bielefeld group and others have also investigated multiple ionization of diatomic molecules N_2 [13], [32] , O_2 [28] and CO [33]. As a result of their investigation, a more advanced model of CE fragmentation was developed. This model was founded on a statistical characterization of the individual potential curves. Results of their study led to a satisfactory description of the kinetic energy spectra [15] [16]. Collision induced fragmentation of more complex and triatomic molecules such as CO_2, N_2O, NO_2 or CS_2 have been studied and reported from the 80's to early 2000's. The first experiment to use time and position sensitive detection to analyze the complete fragmentation process in CO_2 was carried out by the Tokyo Metropolitan University (TMU) group [17]. Using the Ar^{8+} projectile at 250keV and utilizing a "backgammon" type anode method or modified backgammon method with weighted coupling capacitors (MBWC) type anode [34] [30]. Four channels of a digital oscilloscope received the signal from the anode. Afterwards, the relative heights of the pulses recorded on each channel were used to determine the x-y position of the signal transferred to PC.

The trajectories of the fragment ions were used to reconstruct the O-C-O angle θ and thus observe the nuclear geometry of this molecule. Figure 2-6 shows bond angle θ for several channels as well as a calculation of the bend angle distribution in the neutral CO_2 experiencing zero point motion. Similar to the observation in the H_2O [16] the bend distribution broadens as charge state decreases towards the (2, 1, 1) channel. This is due to the repulsion between ions being closer to Coulombic in the higher charges which result in faster dissociation. In lower channels partially non Coulombic potentials lead to some relaxation of the molecule. As a result nuclei start to rearrange during the dissociation process.

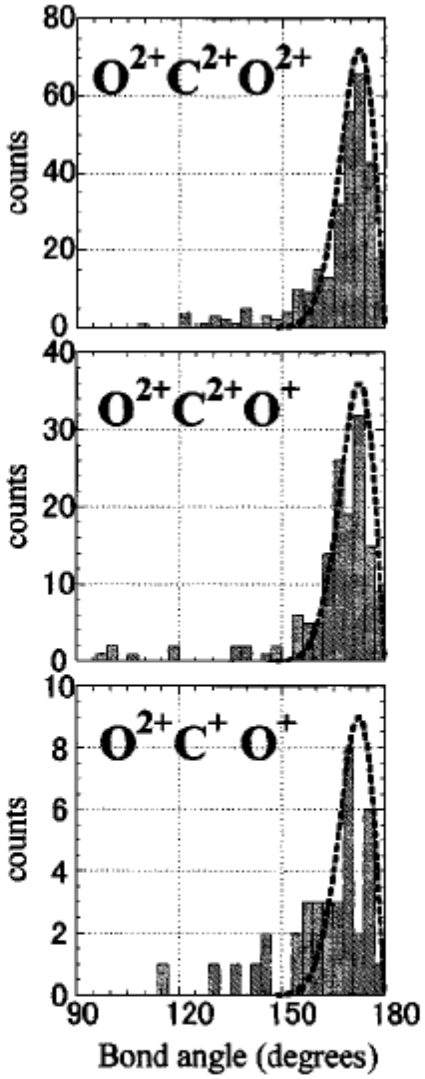

Figure 2-6 Reconstructed histogram of angle θ for O-C-O from fragment velocities, dotted lines shows the probability function for θ corresponding to the zero point motion of the neutral molecule (Reprinted with permission from [17]).

As can be seen in Figure 2-6 the experimental result (bend angle θ peaked near 180° and extending to 140°) confirms the data derived from the initially ground state molecule. They also measured the χ distribution suggesting the break up process is dominated by the concerted processes, where the repulsive Coulomb force between atomic ions, leads to bonds being broken simultaneously. One surprising result was that the velocity of the fragments was somewhat higher than that expected from a purely coulombic potential.

Around the same time the TMU group "Shiromarou and co-workers" [35] employed their apparatus to study the bent NO_2 molecule (NO_2^{3+}, NO_2^{4+}, and NO_2^{5+}). For each collision, the fragmentation process was characterized in terms of fragment velocity vector and the angle between the vectors. It was observed that the angle distribution of the bent highly ionized molecules in the (2, 2, 2) channel was comparable to that of their respective neutral molecule.

CO_2 was again the subject of investigation this time by the group at the Grand Accélérateur National d'Ion Lourds (GANIL) facility in Caen, France. In these experiments, L. Audoui and co-workers [33] employed highly energetic ion beams (11.4 MeV/A O^{7+} and 8 MeV/A Ni^{24+}). These ions collided with localized dense molecular gas targets such as CO_2 in a supersonic jet. After impact the fragmented ions were extracted and then directed by a strong electric field (200V/cm) to a PSD.

The authors analysed the data for the triple fragmentation channel of CO_2 into three ions as well as two ions and one neutral atom, to determine if the process of the dissociation is concerted or stepwise. They found that dissociation is highly concerted in the case of coincident production of C^+, O^+, and second O^+ fragment. However, in the case of C^+, O^+ and neutral O channel, the dissociation process is stepwise with the metastable channel of $O^+ + CO^+$.

To have a better picture of these two break up processes for the related channel, they plotted the χ and θ distribution as depicted in Figure 2-7 and Figure 2-8. Figure 2-7 shows the θ and χ distributions of the fragmented C^+, O^+ and O^+ ions after fragmentation by 8 MeV/A Ni^{24+}.

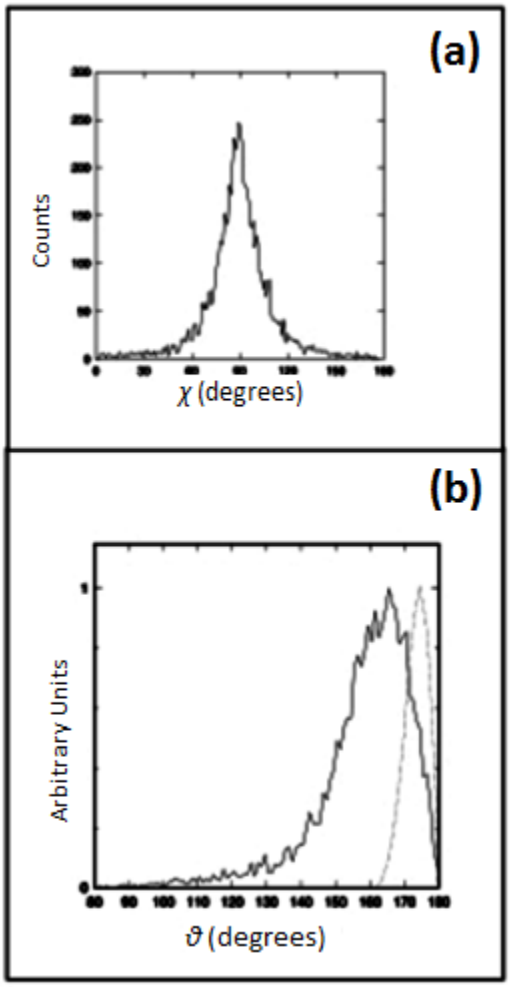

Figure 2-7 (a) Final state χ distribution of C^+, O^+, and second O^+ channel, (b) Bend angle θ distribution, dotted line ground state zero point distribution of the neutral CO_2, straight line experimental distribution (Reprinted with permission from [33])

As can be seen in Figure 2-7 (a) the χ distribution is centered near 90º and confirms the concerted process. Comparing the result to the H_2O molecule experiment, they found that the width of the distribution is almost the same as that of the H^+, H^+, O^+ [16]. In the θ distribution the most probable value is 160º which is a shift to smaller value when compared to the ground state value of the zero point distribution of the neutral molecule, indicating that the molecule is slightly bending before breaking. As can be seen in Figure 2-7 (b), the distribution extended to 100º. The same Figure 2-8 shows the χ distributions for $(CO_2)^{2+} \rightarrow C^+ + O^+ + O$, by 8 MeV/A Ni^{24+}.

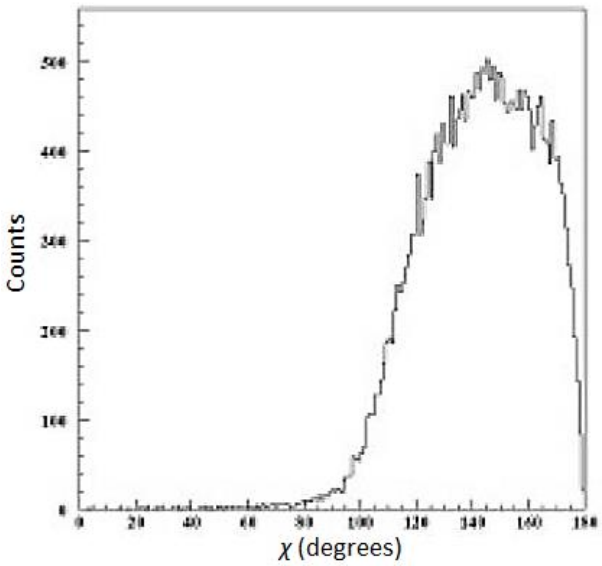

Figure 2-8 χ distribution of C^+, O^+ and neutral O fragmentation (Reprinted with permission from [33])

The distribution which is calculated by assuming the neutral oxygen atom momentum plus the ion fragment momenta add to zero is now quite uniform from 90-180º range. This wide distribution confirms the stepwise process of this channel.

This work was followed in 2002 by work from the Bielefeld group [15] which shed more light on kinematically complete analysis of fragmentation of CO_2 in collision with highly charged ions (5.9 MeV Xe^{18+} and Xe^{43+}). KER, characteristic angles χ, and θ_v for each individual molecule were calculated and depicted in Figure 2-9. As can be seen from the χ distributions, the symmetric charge states peak near 90 degrees indicating the break up process is strongly concerted; furthermore the asymmetric processes also peak close to the expected value for a concerted process (shown by the arrow)

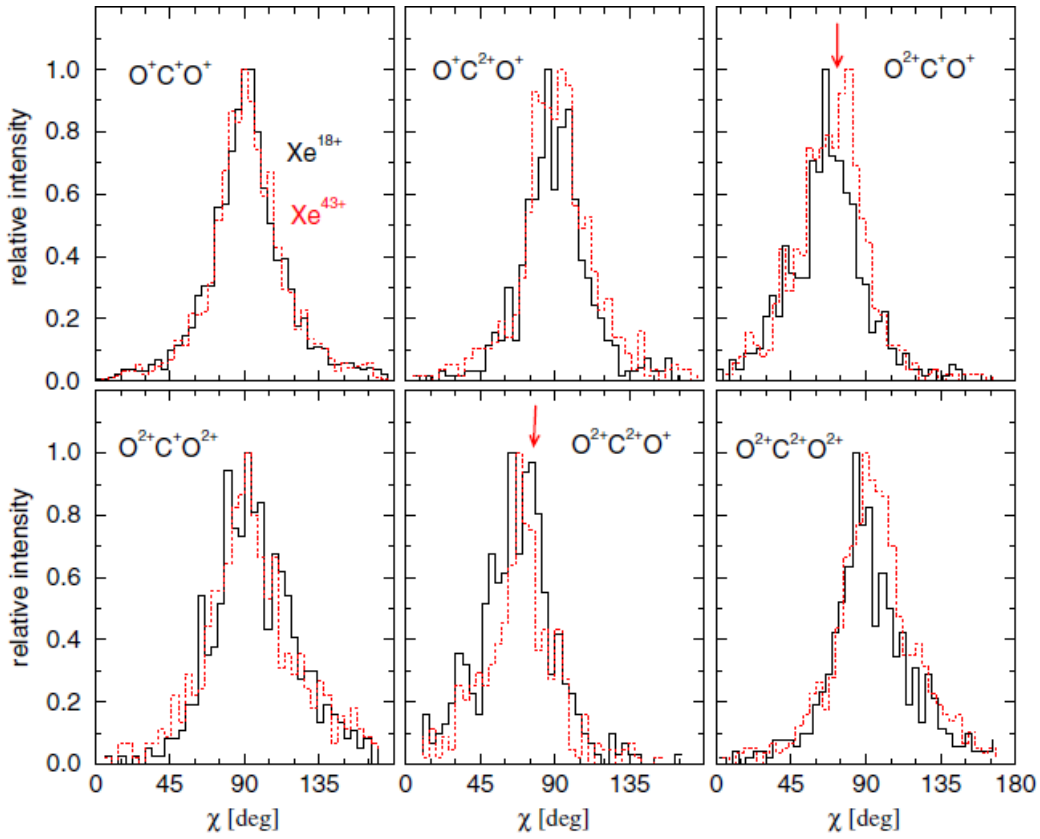

Figure 2-9 the measured angle χ distribution in C^{p+} + O^{q+} + O^{r+} fragmentation, solid line represent collision with 5.9MeV u^{-1} Xe^{43+}, and dashed line represent collision with 5.9 MeV u^{-1} Xe^{18+} (Reprinted with permission from [15])

It can be concluded that the molecule has undergone a simultaneous break up. Hence, O–C–O bond and angle θ_v can be deemed connected. According to Figure 2-10, experimental results of bend angle from θ_v are in reasonable agreement with the results predicted from CE model. However, Figure 2-11 shows that the KER distributions are considerably broader than what have been predicted by the CE model [15]. In fact, the model seems to underestimate the energy of some of fragmentation channels, as with the earlier work [17].

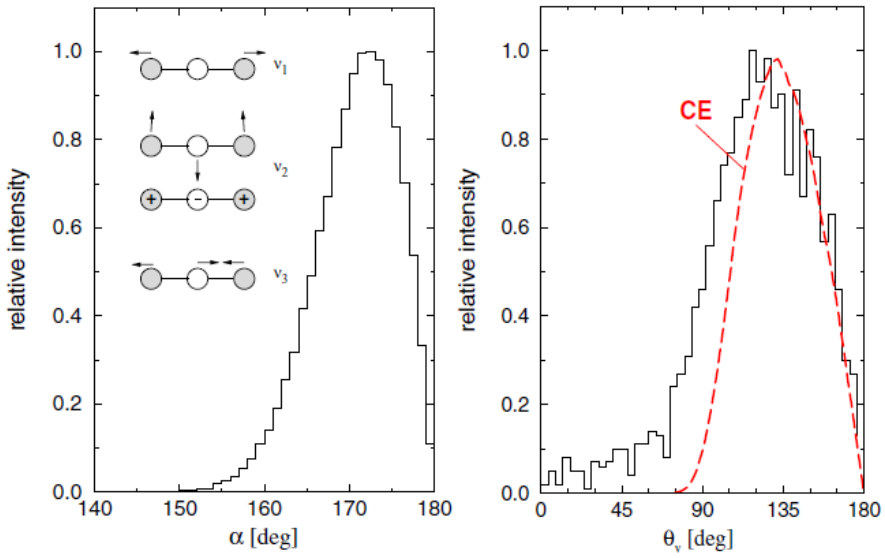

Figure 2-10 Left side plot, the O-C-O bond angle distribution for four vibrational modes, right side plot, the angle θ distribution for $O^+ + C^+ + O^+$ channel, red dashed line Coulombic model, black solid line experimental data (Reprinted with permission from [15])

Obviously the role of detailed electronic structure of the intermediate CO_2^{q+} molecular ion in changing KER as a consequence of mutual screening of the fragmenting ions is important. In fact, sensitivity of the angular parameters to this effect is less as a result of the symmetric nature of the molecule.

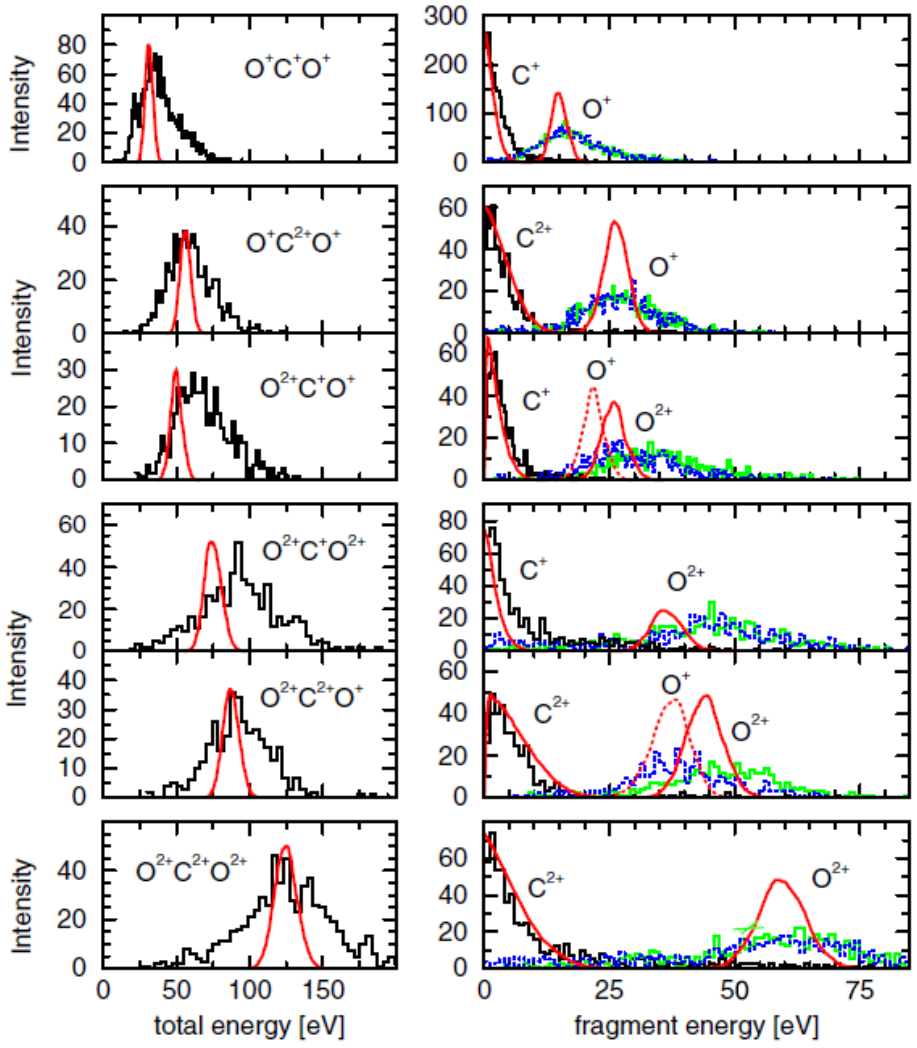

Figure 2-11 KER of C^{p+} + O^{q+} + O^{r+} channels, left side CO_2 collision with 5.9 MeV u^{-1} Xe^{43+}, right side KER spectra of individual fragment ions. The red solid curves the prediction of the CE model. (Reprinted with permission from [15])

The GANIL group followed up its earlier work in 2006 [36] conducting a series of HCI impact experiments to study fragmentation dynamics of triatomic molecules nitrogen dioxide NO_2, CO_2, and different isotopes of water (HDO, H_2O, D_2O).

As can be seen in the Figure 2-12, in the case of NO_2, the break up process of $NO_2^{3+} \rightarrow N^+ + O^+ + O^+$ was found to be synchronous concerted process.

The Dalitz (see Chapter 4) plot of the (N^+/ O^+/ O^+) channel is defined only on the x_D positive plane by definition, the second fragment is the O^+ ion having more energy than the other. One can clearly see

that in most of the cases, events are distributed on the half circle centered at $x_D = 0$, $y_D = -0.1$ corresponding to the bond angle ≈134º. This is in perfect agreement with the assumption of synchronous concerted fragmentation of the bent NO_2 molecule. However, not all the events are gathered at this configuration, showing subtle structure at the upper right side and the center bottom on the circle. The upper right side structure indicates that the fragments (N^+) and (less energetic O^+) rotate so as to have their position reversed in momentum space during the dissociation. In practice, the more energetic O^+ ion is repelled strongly and the other O^+ has very little impulse along the N^+ momentum axis. As a result, the Dalitz diagram clearly shows that the configuration of the molecule changes during the fragmentation via metastable NO^{2+} fragment molecule.

One can thus suppose that some of break up processes follow an intermediate step (NO^{2+}/O^+). Then the second bond breakage of $NO^{2+} \rightarrow N^+ + O^+$ occurs with rather long lifetime so that metastable molecular ion NO^{2+} has a time to rotate.

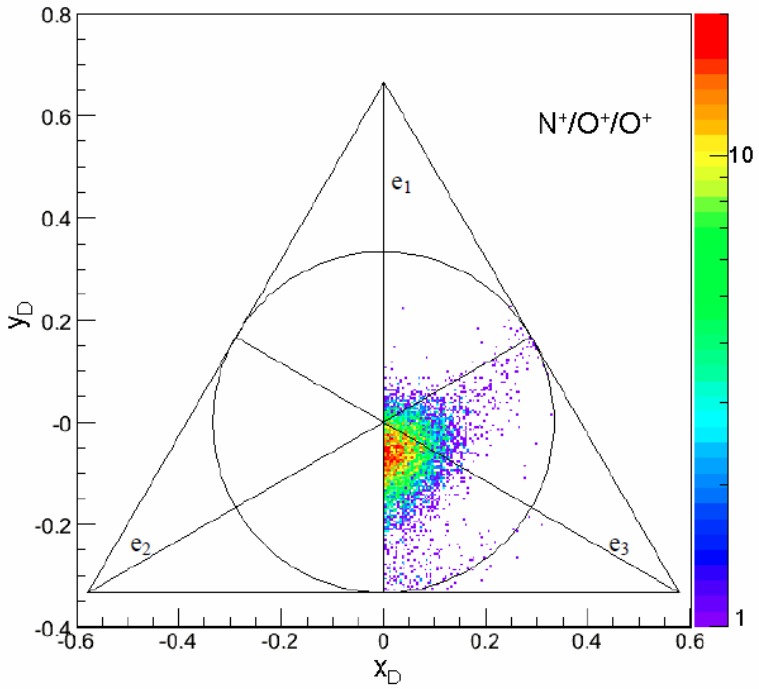

Figure 2-12 Dalitz plot of three body dissociation $N^+ + O^+ + O^+$ channel (Reprinted with permission from [36])

Much of the concentration of this work was on doubly ionized species. Mainly, two types of dissociation were studied for NO_2^{2+}: 1) (NO^+/O^+) and 2) ($N^+/O^+/O$). The former has a single KER peak similar to NO_2^{3+} and can be deemed as an intermediate for the latter.

Fragmentation of isotopic water molecules (HDO, H_2O, D_2O) was studied to obtain more insight in fragmentation process of triatomic molecules. The focus was on the difference of cleavage behavior between the OH bonds over the OD bond in fragmentation of HDO^{2+}. Analyzing all dications of (H^+/OD^+), (D^+/OH^+), (H^+/OH^+) and (D^+/OD^+) resulted in different KER distributions. The results showed attractive nature OD^+ potential as the O-H distance increases faster with respect to the O-D distance.

Neumann and co-workers [18] conducted a Coulomb explosion experiment on the fragmentation of CO_2^{3+}. The parent molecule was hit by an ion beam of Ar^{8+} projectiles at 3.2 keV from the ECR Ion Source facility at Goethe University, Frankfurt. In addition, coincidence of the projectile charge state and all three fragments was measured using a delay line anode.

They defined three decay mechanisms in the study in response of the question: what parameters do control the decay mechanism of a species during Coulomb explosion? As defined earlier the first two mechanisms are the concerted processes and the sequential or stepwise process specifically $CO_2^{3+} \rightarrow CO^{2+} + O^+ \rightarrow O^+ + C^+ + O^+$ in this case.

The third mechanism is called asynchronous break up, during which all bonds break in a concerted process but with asymmetric bond lengths. The Dalitz plot method has been utilized to visualize the three-body processes and accordingly identify the type of break up mechanism.

Figure 2-13 represents results of experiments in both Dalitz and Newton plots. Each break up event has certain geometry of momentum vectors and all possibilities of geometries at the time of break up can be framed in the Dalitz plots. Figure 2-13 (a) depicts the entire possible break up geometries for the neutral CO_2.

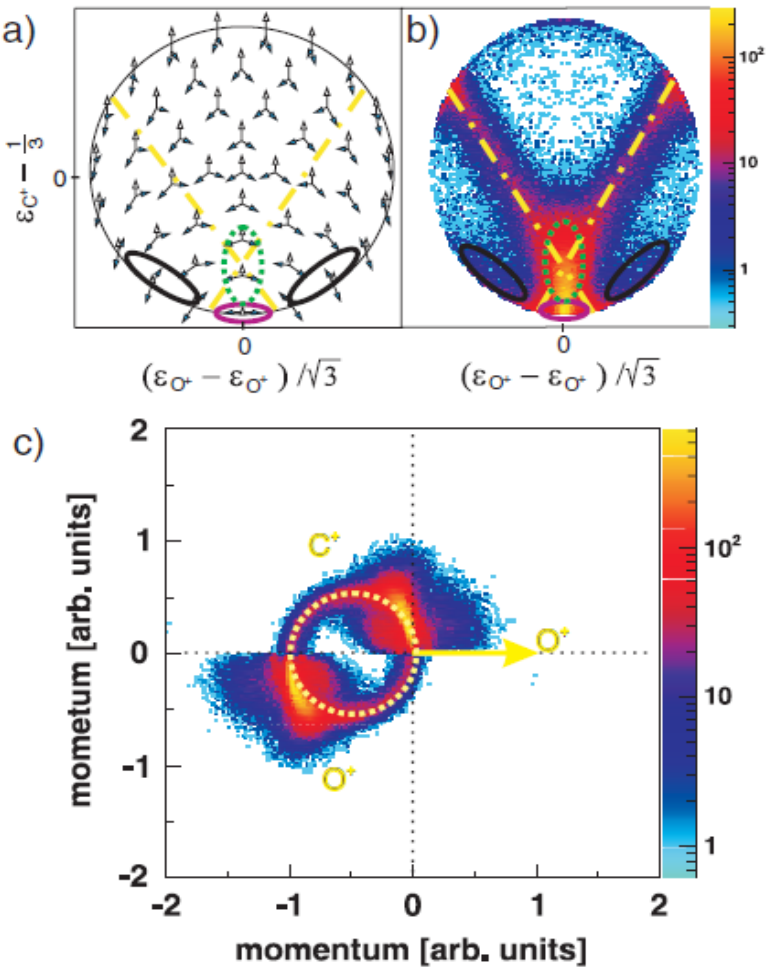

Figure 2-13 Dalitz and Newton plots, (a) Characteristic momentum vector geometries for specific points in the Dalitz plot, (b) Dalitz plot of experimental data for CO_2^{3+} concerted O^+ + C^+ + O^+ and stepwise CO^{2+} + O^+ break up, (c) Newton plot for CO_2^{3+} concerted and stepwise processes (Reprinted with permission from [18])

Figure 2-13 (b) is the Dalitz plot of the measured data. Bending and the asymmetric stretching of the molecule are also depicted in the green dashed oval and the black oval area on the left and right, respectively. Sequential break up can be tracked by the presence of an X-shape area marked by a yellow dashed dot which contains 20% of all the events. The violet oval area represents the region of highest probability in which the configuration is close to the nearly linear ground state geometry of the CO_2 molecule. Figure 2-13 (c) shows the Newton diagram which further emphasizes the processes shown in the Dalitz plots. Sequential break up of the molecule can be clearly represented, as the

momentum for C^+ and the O^+ ions appear to the left, The yellow arrow fixed at 1 a.u. and pointing to the right indicates the direction of momenta for the second O^+ ion, which for a near linear configuration is equal and opposite to the first O^+ while the C^+ has near zero momentum (indicated by the most intense regions) and the second O^+ ion also has momentum with magnitude close to 1a.u.. Stepwise processes are specified by a circular region in which the carbon and oxygen can be seen to switch places with O^+ having zero momentum and C^+ having 1 unit of momentum ($CO_2^{3+} \rightarrow CO^{2+} + O^+ \rightarrow O^+ + C^+ + O^+$).

As a result, the dissociation process of the CO_2^{3+} molecule can be pictured as follow: 1) the initial dissociation to an O^+ ion and a CO^{2+} ion and 2) final dissociation of the CO^{2+} fragment to a C^+ ion and a second O^+ ion. As mentioned earlier, the second dissociation process takes place at a distance where there is no longer any interaction between departing O^+ ion and the CO^{2+} fragment after a delay.

KER and KE distribution graphs corresponding to different break up mechanisms have been reported for different zones on the Dalitz plot by this group. Through this, the dominant break up can be recognized by analyzing the amount of energy that is released during the break up process. Thus, as a result, metastable (stepwise) break up of CO_2^{3+} has been tracked along with concerted break up in terms of energy release, with the stepwise process being characterized by low KER.

The TMU and Waterloo groups [37] studied multiple ionization of OCS in collisions with Ar^{4+} and Ar^{8+} using a system equipped with time and position sensitive detection. The experiment was carried out at 15 keV q^{-1} at the TMU facility and data analysis was done at University of Waterloo, Waterloo, Canada. The condition of the experiment led to complete break up of the molecule $OCS^{d+} \rightarrow O^{a+} + C^{b+} + S^{c+}$ (d=a + b + c). The authors compared the experimental results to the results obtained from simulation of the break up. The simulation is based upon assumption of a point-like ion and purely Coulombic potential from ground state distributions of bond lengths and bond angle. The results showed more broadness of experimental distributions of KER and low energy peak, which were not anticipated from theoretical results. Increasing the final charge state, however, led to more agreement between experimental and theoretical results. For the (2, 2, 2) case, induced bending was also lower than (1, 1, 1) channel. The mechanism of fragmentation in terms of being concerted or step-wise has been characterized using Newton and Dalitz plots as in [18].

Figure 2-14 shows the Dalitz plots for the Ar^{4+} (1, 1, 1) channel and Ar^{8+} (2, 2, 2) channel. The corresponding configurations of momentum vectors of fragments on Dalitz plot is plotted in Figure 2-14 (a). In Figure 2-14 (b) green and red diagonal lines show sequential fragmentation of OCS into a

metastable CO^{2+} and CS^{2+} ions, respectively. For the (1, 1, 1) channel, a high degree of asymmetry is perceivable through the presence and spreading of data in the region of both stepwise channels, but not to the extent seen in CO_2. In Figure 2-14 (c) showing the data for the 6+ channel, more localized distribution is achieved which suggests occurrence of the Coulomb explosion in the vicinity of equilibrium bond angles and bond lengths. However, a degree of bending and asymmetric stretching still exists around the equilibrium geometry as can be seen by the extent of the signal.

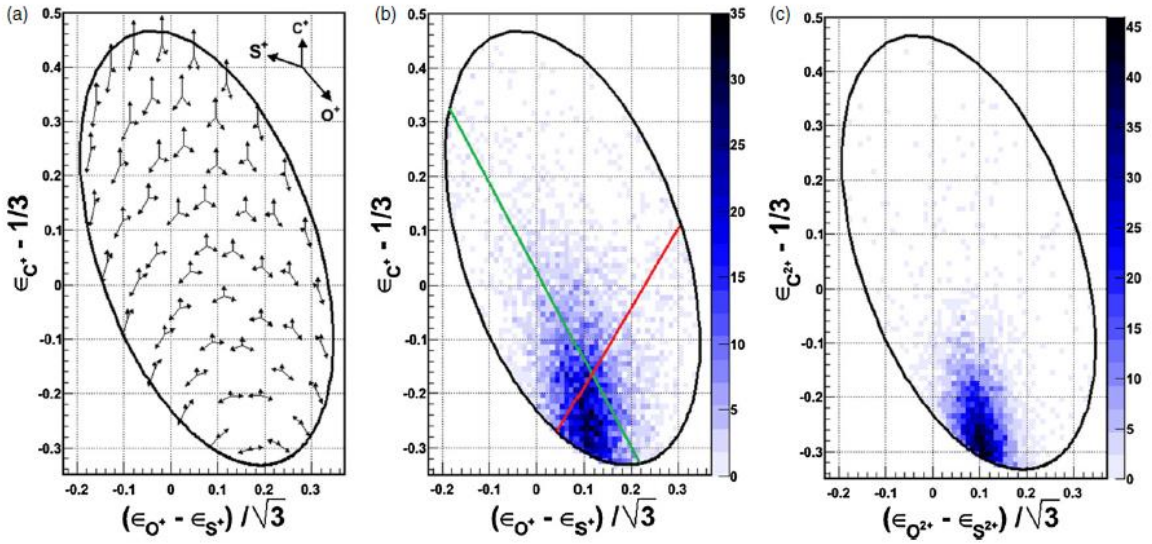

Figure 2-14 (a) Momentum vectors for various points on the Dalitz plot, (b) Ar^{4+} generated (1, 1, 1), and (c) Ar^{8+} generated (2, 2, 2). The green diagonal line indicate the region for $CO^{2+} + S^+$ and the red diagonal line shows $CS^{2+} + O^+$ (Reprinted with permission from [37]).

2.4 Background of ionization view of laser Coulomb Explosion

Since 1980 short pulse lasers have been developed dramatically [4] [38] [39], so that now few femtosecond (10^{-15}s) pulses and even attosecond (10^{-18}s) [40] pulses are available. Accordingly, as the time scale of the pulse duration of lasers has become comparable to that of vibrational and rotational motion of small molecules, short pulse lasers have become increasingly important as molecular probes. By focusing these pulses to a very small area, has led to increasingly intense laser light. The intensity I is related to the electric field E by the relationship $I = \varepsilon_0 E^2/2$ (where ε_0 is the permittivity of the vacuum). We can generate enormous electric fields which can be bigger than the binding field in an atom or molecule.

Absorption of either one (resonance ionization) or multiple photons ionization (MPI) can initiate an ionization process [41].The physics behind the intense laser ionization of atoms, particularly in the high intensity and low wavelength regime, has been well addressed. As a result, different regimes are reasonably categorized according to the so-called Keldysh parameter [42]. The Keldysh parameter can be explained based on the relation between ionization potential of a bounded electron in an atom and the ponderomotive energy conveyed by the laser field to a free electron in the following fashion:

$$\gamma_k = \left(\frac{U_{IP}}{2U_P}\right)^{1/2} \tag{2.1}$$

In this formula U_{IP} is the ionization potential of a bounded electron in an atom and U_P represents the pondermotive potential energy. The pondoromotive energy itself can be obtained using the following formula:

$$U_P = \frac{(eE_0)^2}{4m\omega^2} \tag{2.2}$$

where e is the electric charge and m is the mass of electron. The electric field of maximum amplitude is represented by E_0, and frequency with ω [43].

In the case of the hydrogen atom, when the laser intensity increases (10^{12}-10^{16}W/cm^2) several ionization processes emerge. Depending on the ionization process, each has a partial cross-section which essentially depends on the laser wavelength, rise-time and focused intensity [44] [45]. For example, resonantly enhanced multiphoton excitation at lower intensities ($\sim 10^{12}$ W/cm^2) may result in ionization and the dissociation of a molecule [44]. At higher intensities up to $\sim 10^{14}$ W/cm^2 electron tunneling ionization (TI) is more likely to happen. In this case the ponderomotive energy and the binding potential U_{IP} are in the same range ($\gamma_k \approx 1$). Further increment of the intensity up to $\sim 10^{16}$ W/cm^2 will result in the dominance of ponderomotive energy over binding potential ($U_p > U_{IP}$). This facilitates the passing of the electron over the potential barrier classically. This phenomenon is so called over the barrier ionization (OTBI).

More detailed analysis of the ionization processes based on the Keldysh parameter and the condition for different ionization can be found in references [42]. In this chapter we will mostly focus on a survey of published theoretical and the experimental studies, of molecular multiple ionization and Coulomb explosion.

2.4.1 The classical view on the field ionization for molecules

A simple approach was used by the group at Reading University, UK to model ionization in the laser field [44]. A schematic view of the field ionization of xenon is depicted in Figure 2-15. According to the field ionization model, the Coulombic well of the singly charged atom is occupied by the outmost electron of a neutral atom. This has been illustrated for the case of 5p electrons in xenon in Figure 2-15 (a) by a point-like core with a comparable energy level corresponding to the ionization potential of the atom. According to Figure 2-15 (b), application of an external electric field leads to distortion of the potential well. Based on the classical field ionization model, ionization can only take place when the electron passes over the top of the barrier which was facilitated by lowering the barrier. Considering an electron as a quantum particle, however, may lead to tunneling through the barrier at a somewhat lower intensity of the laser. Codling and coworkers chose to lower the potential barrier to about 3 eV to ensure a reasonable transmission rate. The second ionization step is depicted in Figure 2-15 (c) where a doubly charged core and an electron are assumed to be at an energy level suitable to the second ionization potential. Again, the external field must be further increased to trigger the double ionization. This process continues progressively for other electrons. For example, Figure 2-15 (d) indicates the distorted barrier potential for the fifth ionization step. In particular, Figure2-15 (d) emphasizes the sensitivity of tunnel ionization to laser intensity. Noteworthy, is that in this model electrons are sequentially removed at prescribed laser intensities.

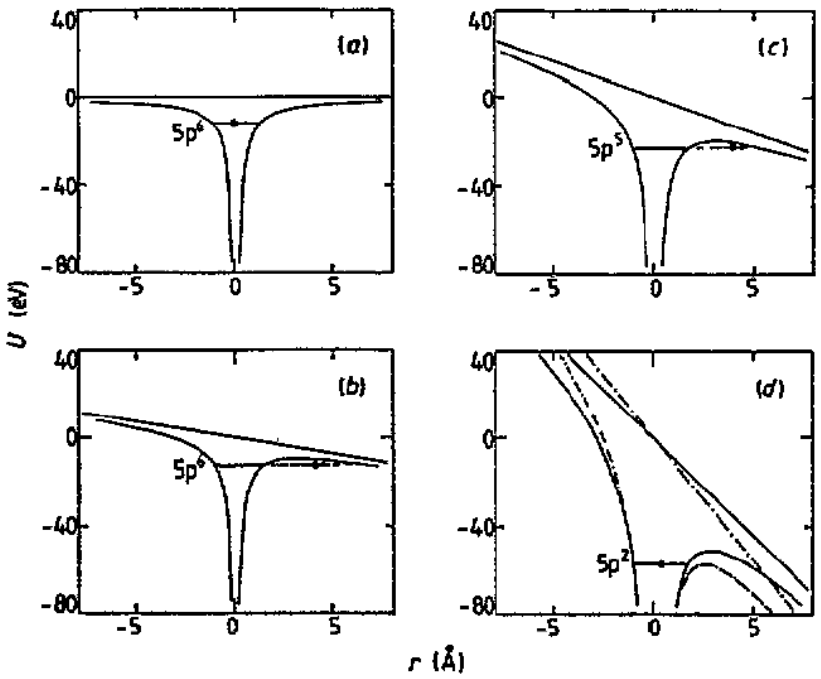

Figure 2-15 Field ionization in Xe, (a) q=1, E=0, (b) q=1, E=1.4 VÅ^{-1}, (c) q=2, E=3.2 VÅ^{-1}, (d) q=4, E=8.9 VÅ^{-1} and 11.3VÅ^{-1} (Reprinted with permission from [44])

Later on, a model was developed by Posthumus and co-workers also at the University of Reading, UK, [19], [46] for explaining the experimental observation that molecules appear to dissociate from a bond length nearly a factor of two longer than for the neutral [21] the model predicts a critical internuclear separation for diatomic molecules. Predicting appearance intensities of ions created in particular ionization channels, this model is capable of calculating the kinetic energies of the ionic fragments. The model is based on purely classical over-the-barrier treatment of a multiple ionization of diatomic molecules. Prediction of the critical distance at which the ionization potential is maximized is one of the most important features of this model. In detail, according to equation 2-3, the laser-molecule potential is related to the distance along the internuclear axis x , the internuclear separation R, and the laser field E_0:

$$U = -\frac{Q}{|X+R/2|} - \frac{Q}{|X-R/2|} - E_0 X \qquad (2.3)$$

In this equation Q can be calculated by:

$$Q = \frac{Q_1+Q_2}{2} \qquad (2.4)$$

where Q1 and Q2 are the charges of the atoms. Assuming U_1 and U_2 as the ionization potentials of the atomic ions, they committed to approximate the energy level E_L of the outer electron in a certain potential by:

$$E_L = \frac{\left(-U_1 - {}^{Q_2}/_{R}\right) + \left(-U_2 - {}^{Q_1}/_{R}\right)}{2} \qquad (2.5)$$

This energy considers the contribution of each charge across the internuclear separation as defined as the average of the ionization potentials. The critical separation was defined as the separation where the energy level E_L touches both the inner and outer potential barriers [19].

In order to compare and validate their model, Posthumus and coworkers [19] attempted to summarize the experimental and theoretical result of the critical separation obtained for a number of diatomic (N_2, O_2, Cl_2, I_2, and CO) and also simple symmetric triatomic carbon dioxide molecules for a wide range of ionization channels with the assumption of structural linearity for CO_2 [47]. The model confirmed that critical distances are independent of ionization channel which was in accordance with previous experimental observations [19]. The shortcomings of this model are that it does not take into account either the laser pulse length or non-sequential electron ejection. A year later, a modified model was developed for the field-ionization Coulomb explosion to tackle the first issue. Posthumus et al. [46] used a similar equation, (2-3) and (2-4), as their previous model for the new field-ionization CE model. Figure 2-16 illustrates the result of field-ionization CE model as applied to the $I_2^+ \rightarrow I^+ + I^+$ channel.

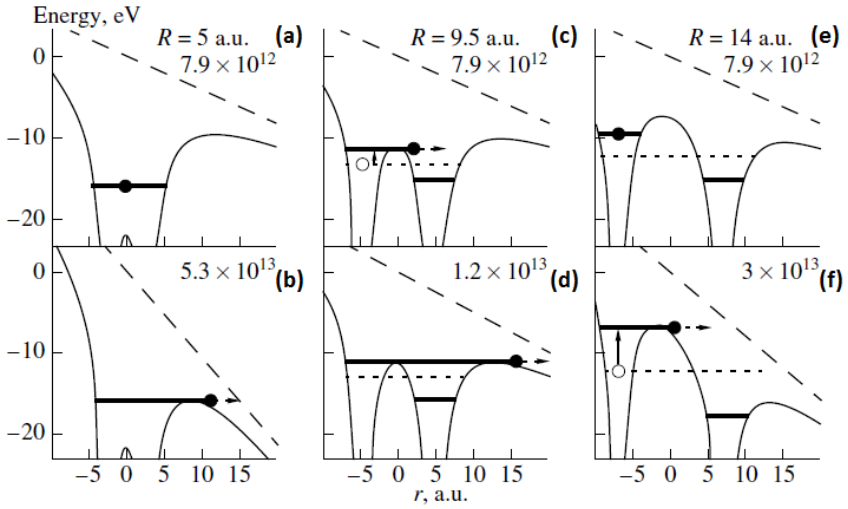

Figure 2-16 Double well potential for the outer electron of I_2^+ in a strong external electric field and at three internuclear separation. Laser intensity is presented on each figure (Reprinted with permission from [46]).

According to Figure 2-16 (a) the central potential barrier is well below the energy of the outer electron at an internuclear separation of 5 au. However, it is required to increase the intensity to 5.3 $\times 10^{13}$ W/cm^2 to overcome the outer barrier. As the internuclear separations increase it inversely affects the appearance intensity (decreasing) due to the rise of the electronic energy level, E_L, and also, the action of the electric field over a longer distance. The latter has more impact in the decrease of the outer potential barrier.

As the internuclear separation increases to R = 7.5 au, electron localization becomes important through the rise of the central barrier above the energy level of the electron. This leads to isolation of the electron in one of the two wells created by the nuclei and the laser field. According to Figure 2-16 (c) and (f), the electron energy tends to increase due to Stark shift or decrease when it is localized in the left and right hand wells, respectively. As the electron in the left hand well can readily ionize, the electron localization facilitates further decrease in appearance intensity. In fact, only 1×10^{13} W/cm^2 required triggering ionization.

Further increase in internuclear distance to values greater than 10 au is followed by hindering of ionization due to an intensified central barrier. The height of the central barrier increases as a function of R as does the appearance intensity. This observation inspired them to identify a minimum in the appearance intensity, as a function of internuclear separation, as the origin of the experimentally

observed critical distance, R_C. Thus, according to Figure 2-16 (d), R_C is the point where the upper Stark level is at the same energy as the central and outer barriers.

The classical model was used by Posthumus et al [46] for different intensities and pulse lengths to obtain the ionization channels. The channels are, indeed, dependent on the peak intensity, but the characteristic internuclear separations for the channels are always close to the critical distance (Figure 2-17). This is because the point of ionization is given by the crossing of the intensity curve with the highest threshold curve. Only for very long pulses of 400 fs is the final state reached after R_C. Therefore, the processes to reach (4, 4) can be deemed as a Post Dissociative Ionization (PDI) of the (3, 3) channel.

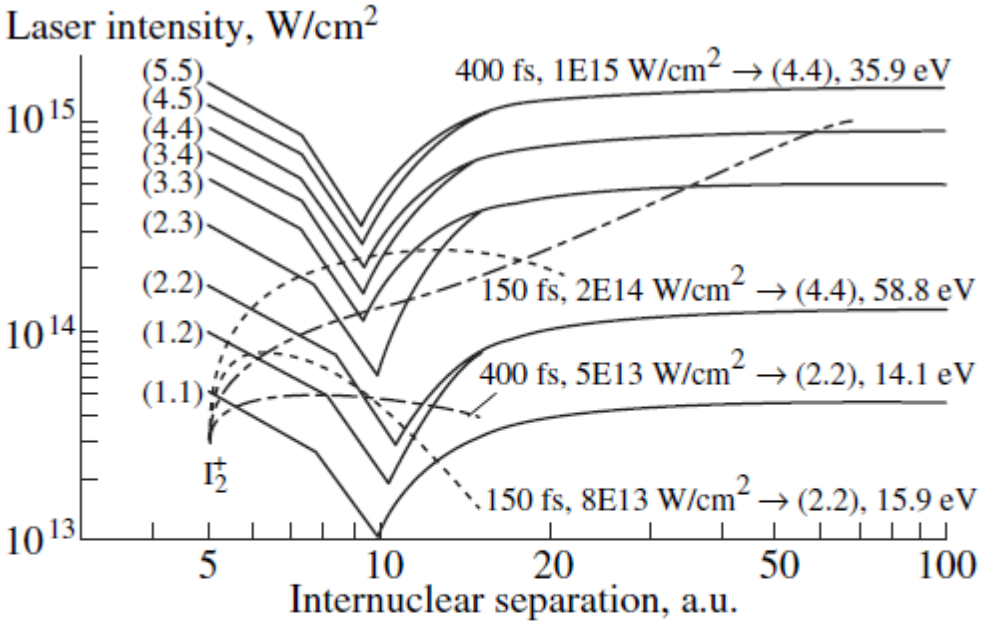

Figure 2-17 Solid curves classical appearance intensities for the various channels of I_2, and dashed curves classical trajectories for 150fs laser pulse lengths, and dot-dashed curves classical trajectories for 400fs laser pulse length (Reprinted with permission from [46])

2.4.2 The Quantum mechanical view of Coulomb explosion

In this section we introduce the theoretical quantum mechanical approach to intense laser field induced multiple ionization of a molecule, conducted by a number of groups in the last quarter of a century.

Corkum and coworkers [48], [49] analyzed experimental data and concluded that there must be a critical separation distance for molecular ionization. That is, molecular ionization starts with removal

of one or more electrons until the molecule reaches to a first repulsive state. Afterwards, rapid multiple ionization of the molecule can take place around a critical distance. If the molecule does not have sufficient time for expansion to reach to the next critical distance, the ionization process comes to a halt. As a result, one can anticipate the fragment ions from all channels to explode almost from the same internuclear separation.

Based on solving the time dependent Schrödinger equation (TDSE) for simple molecules, behavior of one- and two-electron systems in intense laser fields of different wavelengths (532 nm, 600 nm and 1064 nm) was studied by Bandrauk and co-workers [50]. Using split-operator numerical methods, one-dimensional treatment of nuclei and electron(s) was carried out in the Born-Oppenheimer regime; whilst later calculations were based on three-dimensions in the non-Born-Oppenheimer regime. As a result, significant enhancement of the ionization rate in H_2^+ compare to atomic hydrogen over a specific range of internuclear separations was reported. The phenomenon depends on the existence of charge-resonance (CR) states that at the critical distance two states (its two lowest states, $1\sigma_g$ ground state and $1\sigma_u$ first excited state) are strongly coupled to the laser field and the rate of ionization will be increased. This observed phenomenon was given the name charge-resonance enhanced ionization (CREI) [50]. In detail, treating the molecules in three-dimensions within the Born-Oppenheimer regime, the ionization rate of H_2^+ was calculated as a function of R. The results of their numerical calculation are presented in Figure 2-18 where there are two distinct peaks in the ionization rate at R_1= 7 au and R_2= 10 au R_1 and R_2 are attributed to the effect of the laser field on the Coulomb potential from the two nuclei and the existence of the pair of CR states that are coupled to the electromagnetic field at large R, respectively.

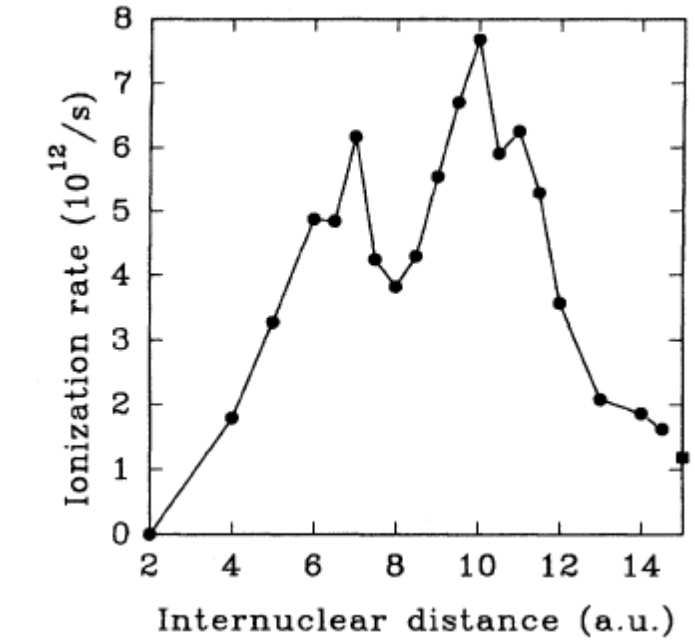

Figure 2-18 Ionization rate of the H_2^+ molecular ion, the square on the right vertical axis marks the ionization of the hydrogen atom (Reprinted with permission from [50])

The ground state, $1\sigma_g$, and the first excited state, $1\sigma_u$ of H_2^+ which are considered as CR states have an important role for the ionization of H_2^+ at intermediate to large R (CREI). Based on the field ionization model of Codling et al.[51] Bandrauk and co-worker [50] employed a DC-field (E_0 = 0.0533 a.u., I = 1×10^{14}W/cm^2) tunneling ionization model for long wavelength laser ionization of atoms and expanded the approach for diatomic molecule H_2^+. Figure 2-19 is the plotted potential along with the lowest autoioniziation states ($1\sigma_+$ and $1\sigma_-$) for R = 6 au, R = 10 au and R=14 au. This group calculated the energy levels $1\sigma_+$ and $1\sigma_-$ and their ionization rates. As it can be seen in Figure 2-19 the inner barrier between the two nuclei frees the $1\sigma_+$ level at R=10 au. So the $1\sigma_+$ level lies just above the inner barrier and ionizes very fast. In this case, because of the strong coupling between the CR states and external field the population of the $1\sigma_+$ level is enormously high. For the smaller internuclear distance (R = 6 au), although the inner barrier is below the $1\sigma_+$ upper level the autoionization rate for this level is small. In fact, the outer barrier becomes comparable and broad which results in lower population and also the coupling between the CR states and the external field is week. Intense laser field ionization of diatomic molecular ions is influenced by asymmetric electron localization. A second ionization maximum at smaller R is achieved through this procedure.

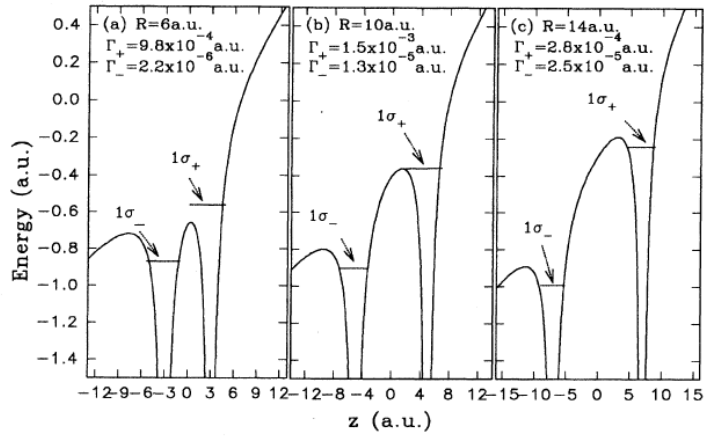

Figure 2-19 Lowest two DC-field induced levels of H_2^+, $1\sigma_+$, $1\sigma_-$ in the effective potential (Reprinted with permission from [50]).

Parallel to this work ,the group of Bandrauk, Seideman and coworkers [49] developed a model based on the field ionization model of Codling et al. [51]. They modeled a typical diatomic molecule B_2 similar to iodine. In detail, considering that the molecule is aligned with the laser field, a smooth one-dimensional potential was designed. They solved the TDSE for an electron moving in this potential and the nuclei were treated in the Born-Oppenheimer approximation. The ionization potential as a function of internuclear separation for a number of Coulombic channels was calculated for two different sets of field conditions. These field conditions determine the ionization rates and ionization probabilities. Qualitatively this result validates the strong enhancement in the ionization rate of molecular ions around a critical separation (double the equilibrium separation) which was observed experimentally, [53] [54] [45].

Although ionization behavior of simple diatomic molecules was well studied, the exact chemical reactions and the stage of structural deformation of them seemed computationally a demanding task. This fact delayed treatment of multielectronic systems and polyatomic systems. Bandrauk and Rual [55] extended the quantum approach to H_3^+ and H_3^{2+} calculating critical distances and predicting critical angles in the ionization dynamics.

In 2003 Sato and coworkers initiated a series of investigations on the ionization of the polyatomic molecule CO_2 [25]. In order to analyze and predict the electronic and nuclear dynamics of polyatomic molecules in intense laser fields, they recommended the use of a time dependent adiabatic state approach which was labeled "field-following". The Schrödinger equation for CO_2 and its ion states was solved using molecular orbital (MO) methods. It is demonstrated that full-optimized reaction

space multi-configuration self-consistent-field (MCSCF) is a useful method to obtain the adiabatic potential surfaces and wave functions. Their model was solved for various instantaneous near infrared field strengths applied to CO_2 and led to extraction of characteristic features of its dynamics which were responsible for structural deformation.

The electric field of the applied laser pulse was assumed to be in the form of $\varepsilon(t) = f(t)\, sin\, \omega\, t$. In this equation, $f(t)$ is the field envelope which was estimated by a realistic pulse shape as

$$f(t) = f_0 sin^2\left(\frac{\pi t}{\tau_p}\right) \qquad 0 \le t \le \tau_p \tag{2.6}$$

Peak strength f_0 was set to 0.19 au (1.3×10^{15} W/cm^2), pulse length τ_p was chosen to be 194 fs, and frequency ω specified at 0.057 au (λ = 795 nm). One of the novelties of this technique is the use of a cycle-averaged potential consisting of the average of the adiabatic potentials at $\varepsilon(t)$ = ± (1/10) au. Consequently, the odd order terms for $\varepsilon(t)$, such as the dipole interaction term is removed. As a result, the pulse amplitude $f(t)$ governs the actual dynamics.

The results of Sato and coworkers' theoretical calculation for CO_2 can be summarized as follow. Firstly, they concluded that in the CO_2 and CO_2^+ stages, ionization takes place before deformation of the molecule as a result of high intensity ($Re \approx 1.17$ Å and $f(t) \approx 0.03$). Secondly, they showed that ionization and dissociation of CO_2^+ leads to CO_2^{2+} with a similar geometry to the equilibrium geometry of CO_2. Then, two extreme cases for the transition of the CO_2^{2+} were considered. In the first extreme which is the vertical transition, the initial vibrational state of CO_2^{2+} was considered equal to the ground vibrational state of CO_2. In the second extreme which is an adiabatic transition, CO_2^{2+} has its own initial ground vibrational state. For the case of a vertical transition, the lowest adiabatic state potential was plotted as a function of the two bond-stretching coordinates R_1 and R_2 and then used to examine the nuclear dynamics. As the dissociation energy of CO_2^{2+} in a zero field is 11 eV in the case of symmetric two-bond stretching and is 1 eV in the case of one-bond stretching, it is anticipated from the calculation results that the probability of the one-bond stretching is higher. However, two-bond stretching takes place simultaneously with one-bond stretching. This is represented in Figure 2-20 (a) by propagation of a wave packet at t ≈ 24.7 fs toward the channels for one-bond stretching (R= 1.5A) from the Franck-Condon region. In this figure, pink contour circles show the probability of the initial wave function around $R_1 \approx R_2 \sim 1.2$ Å and the green contour lines represent the instantaneous potential at ε(t = 24.7 fs)=-0.029 au. Figure 2-20 (b) represents the center of the wave packet moving toward the area of $R_1 = R_2 = 1.4$ au. By contrast to Figure 2-20 (a), the probability of one-bond stretching at ε(t = 96.9 fs) = 0.19 au decreases indicating that it is not greatly enhanced by the field.

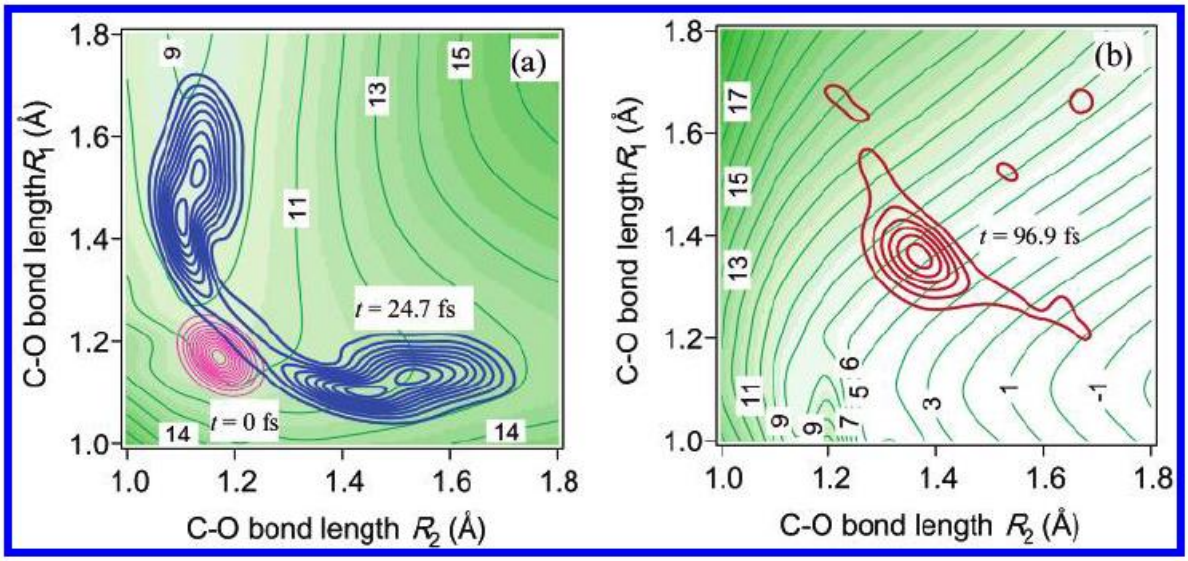

Figure 2-20 Nuclear wave packet dynamics in the lowest adiabatic state |1> of CO_2^{2+} in the vertical transition case; (a) the squares of the nuclear wave functions at t = 0 and t = 24.7fs are denoted by the pink and blue contour lines, respectively; (b) the wave packet at t = 96.9 fs (red lines). In (b) the green contour lines are plotted at intervals of 1 eV (Reprinted with permission from [25].

Thirdly, ionization to CO_2^{3+} takes place after bond stretching of CO_2^{2+} around R_e. According to Figure 2-21, there is a saddle point in the vicinity of $R_1 = R_2 = 1.35$ Å for the potential surface of the field-free lowest adiabatic state of CO_2^{3+}. Also, a hill starts to grow around $R_1 = R_2 = 1.7$ Å by a height of 0.5 eV. For the region of $R_1 = R_2 > 1.7$ Å, Coulomb repulsions of the three atoms governs the potential of CO_2^{3+}.

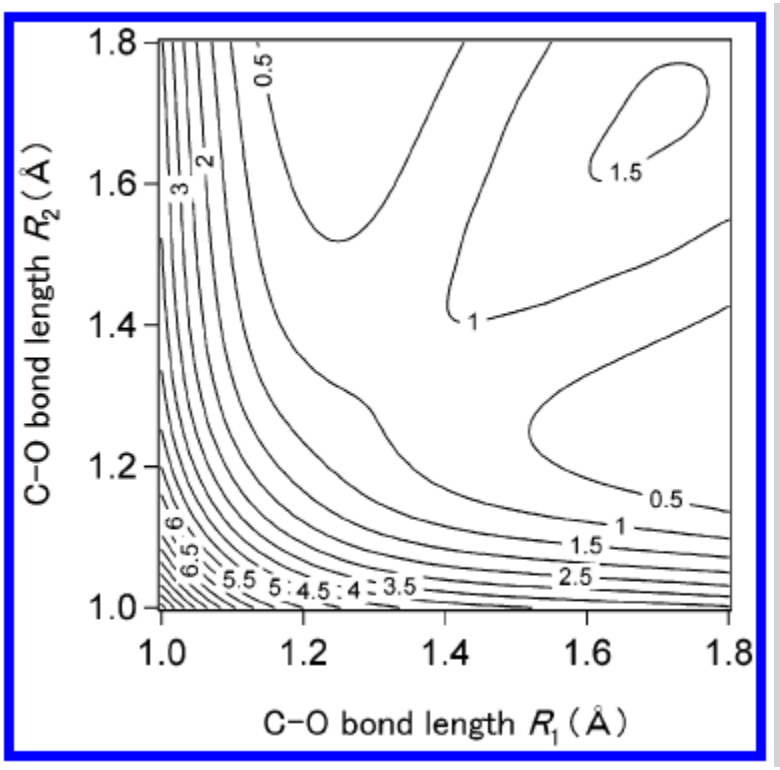

Figure 2-21 Potential of the field-free lowest adiabatic potential of CO_2^{3+} the heights of contour lines are indicated in units of eV (Reprinted with permission from [25]).

Finally, the correlation between bond angle and symmetric stretching is elucidated using a Field-Induced Non-adiabatic transition method. This is done by comparing the results of adiabatic and non-adiabatic transitions. In the adiabatic transition case from CO_2 to CO_2^{2+}, the calculated mean amplitude of the bending motion is increased only1.3 fold. Figure 2-22 (a) represents the wave packet propagation and the cycle-averaged potential at different time scales. The bending amplitude increases a maximum of two fold at t = 84.7 fs. Interestingly, the amplitude of bending motion in $|1\rangle$ decreases after the wave packet passes a point of 1.6 Å. This is not in accordance with the experimental results, where the bending amplitude along with stretching reaches values around 20 degrees [56].

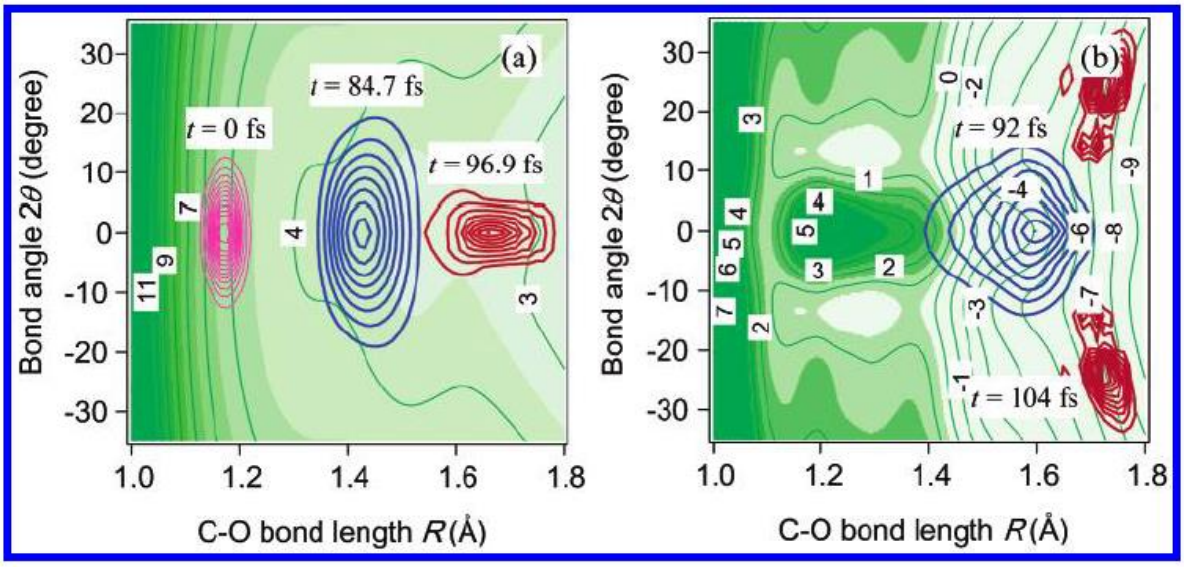

Figure 2-22 (a) Wave packet propagation on the lowest adiabatic state $|1\rangle$ The contour maps denoted by green lines are the cycle-averaged potentials at t = 84.7 fs, snapshots of the wave packet are taken at t = 0 (pink contour lines), t = 84.7 fs (blue lines) t = 96.9 fs (red lines), (b) wave packet propagation on the second lowest adiabatic state $|2\rangle$ in the vertical transition case at t = 92 fs, snapshots of the wave packet are taken at t = 92 fs (blue lines) and t = 104 fs (red lines) (Reprinted with permission from [25])

For the large bond length region (R > 1.7 Å), the energy of one photon (1.55 eV) becomes greater than the difference between the two lowest adiabatic states in zero field. An increase in the bending angle causes a decrease in this difference. Therefore, as can be seen in Figure 2-22 (b), it was concluded that the non-adiabatic transition between the lowest two states with the bending or stretching motion states, |1> and |2>.

2.5 Experimental study of laser assisted Coulomb explosion

Experimental studies of molecules in an intense laser field have revealed many different distinctive dynamical processes such as enhanced ionization, molecular alignment, ultrafast structural deformation, and bond- breaking, all associated with multiple ionization. This review will concentrate mainly on triatomic molecules and the techniques used to experimentally resolve structure and dynamics.

Two approaches which made important progress before 2000 were: 1) Covariance mapping method which was developed by the Reading group of Frasinski and Codling [20] [44] [53], and which was

later used by Cornaggia and Normand [57], and the UCL group of Newell [17] 2) mass-resolved momentum imaging (MRMI) method which was developed by K. Yamanouchi group [58] and its corrected form developed by UCL[59].

2.5.1 Covariance mapping

Pioneering work in the field was first carried out by the Reading group in England [20] [44] [53]. They studied nitrogen ionization and deduced the molecular charge states and kinetic energy released using a simple time of flight mass spectrometer (TOFMS). They used long intense pulses (600nm, 0.6ps, 3×10^{15}W/cm^2) to create molecular ions with charge states as high as N_2^{6+} [53]. They found that the energy released was nearly half of that expected from CE at equilibrium. This was interpreted as stretching of the bond length by a factor of 2. They describe this bond length as the critical distance and the dependence of ionization rate on bond length as enhanced ionization.

TOFMS has been used by many others since the 1950s [29] for determining the species of ions arriving from a focal point or interaction region to the detector. However, this method lacks accuracy when peaks of differing masses and charge states overlap, because of their kinetic energy. More importantly, a simple TOF spectrum cannot give information about which ionic molecular break up channels are occurring. For instance, ionization of the molecule CO to different parent ions CO^+, CO^{2+}, CO^{3+} followed by break up to fragment ions such as C^+, C^{2+} or neutral C and O^+, O^{2+} O^{3+}or neutral O. It is not clear merely from what peaks are present, what processes exist i.e. is (1, 1) common or is (2, 1), or (2, 0). To overcome this problem Frasinski et al. [20] developed the covariance mapping technique to correlate fragments. To distinguish the break up channels of each molecular charge state, the covariance mapping method assigns covariance of each pair of TOF spectra points in a two dimensional map.

In detail, they consider $X_i(t_1)$ as an arbitrary signal from a random process for the ith laser pulse at time t in the TOF spectrum and a similar function can be assumed as $Y_i(t_2)$. These two functions have been used to obtain a tensor product for the calculation of a covariance matrix between a pair of TOF points. Equations 2.7 then can be used to calculate the covariance matrix for a fragment ion pair:

$$C(t_1,t_2) = \langle (X-\langle X\rangle)(Y-\langle Y\rangle)\rangle = \langle XY\rangle - \langle X\rangle\langle Y\rangle = \langle X(t_1)Y(t_2)\rangle - \langle X(t_1)\rangle\langle Y(t_1)\rangle = \frac{1}{N}\sum_i^N X_i(t_1)Y_i(t_2) - \left[\frac{1}{N}\sum_i^N X_i(t_1)\right]\left[\frac{1}{N}\sum_i^N Y_i(t_2)\right] \quad (2.7)$$

where <> is the average value typically over N (20,000) laser pulses.
Figure 2-23 shows a typical fragmentation channel of $CO^{3+} \rightarrow C^{2+} + O^{+}$. Here O_b^{+} (backward oxygen) peak in the X axis has been matched with the corresponding C_f^{2+} (forward carbon) in the Y axis. The result is an island in the covariance map.

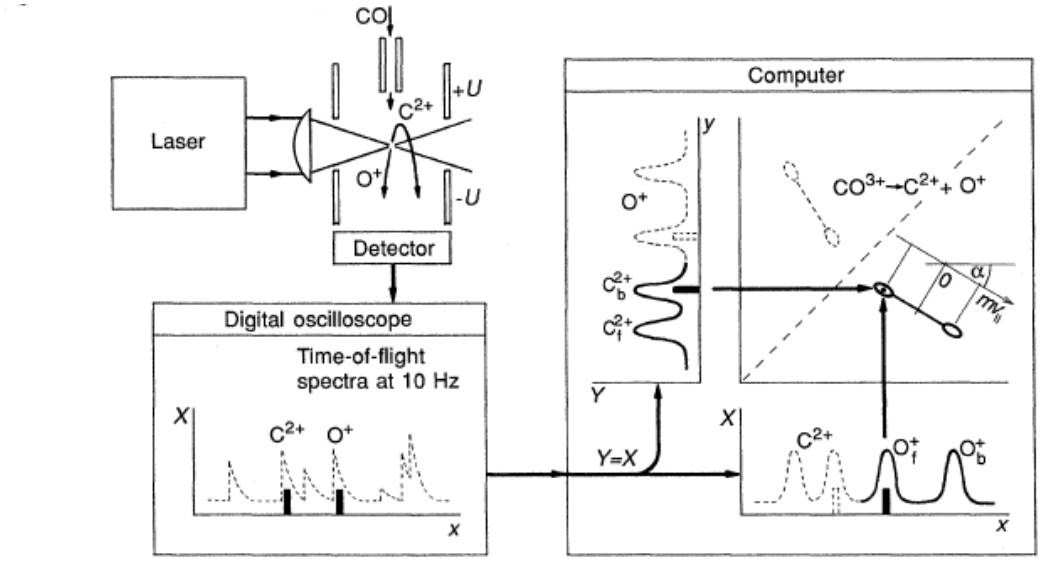

Figure 2-23 The covariance mapping principle for a particular ionization and fragmentation channel of CO, The subscript f and b denote forward and backward fragment ejection as seen by the detector (Reprinted with permission from [20]).

The momentum conservation necessitates linearity of the correlated structure for the case of two body fragmentation. According to a typical covariance map, correlation of forward-backward and backward-forward fragments can be tracked by the two islands on each side of the correlated structure line. Also, the fragment charge ratio can be determined by the line's tilt angle α. Momentum distribution can be realized by the intensity variation along the line and different ionization and fragmentation channels are characterized by different pairs of island on the covariance map.
In the case of CO, a picosecond laser coulomb explosion experiment was conducted and the results were analyzed [20]. For a diatomic molecule, each fragmentation process which leads to a pair of fragment ions will have two corresponding peaks. As mentioned above the TOF peak for each fragment ion can be overlapping with other fragment ions resulting from other dissociation pathways. Figure2-24 (a) shows the covariance map for the fragmentation of CO obtained by this method. The

difference between two large correlated products <XY> (Coincidence map for all data) and uncorrelated product <X><Y> can be seen in Figure2-24 (b) and (c). The association of a broad O^+ peak in the <XY> with three different fragmentation channels of $CO^{2+} \rightarrow C^+ + O^+$, $CO^{3+} \rightarrow C^{2+} + O^+$, and $CO^{4+} \rightarrow C^{3+} + O^+$ is obvious in this figure. Also, a strong diagonal autocorrelation line exists on the map at X=Y as a result of the fact that the spectra X (t) is identical to Y (t).

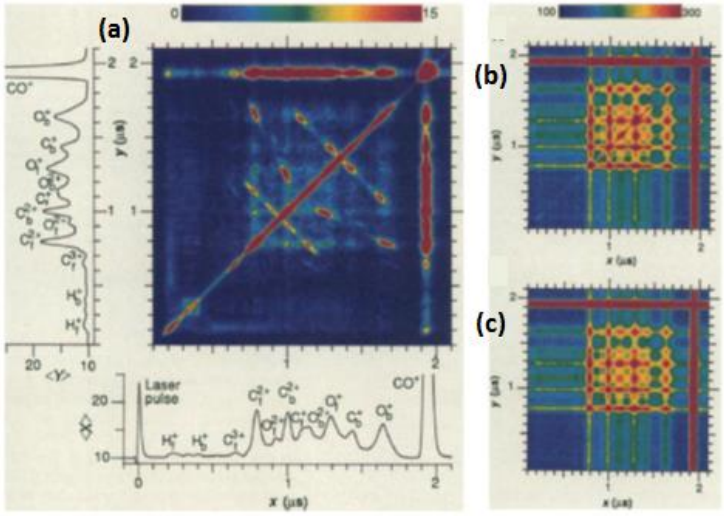

Figure 2-24 (a) A covariance map of CO molecule, X and Y are the signals from the detector in arbitrary units and x (t_1 in the text) and y (t_2 in the text) are the TOFs, (b) the correlated product<XY>, (c) the uncorrelated product <X><Y> (Reprinted with permission from [20])

The Reading group used the same method to analyze ionization of other molecules such as N_2, but importantly also extended the method to triatomic molecules N_2O, CO_2, SO_2 [20].

Using 600 fs, 600 nm laser pulses with intensity of 3×10^{16} W/cm^2, they studied the dissociation of the linear molecule N_2O. Fragmentation takes place along the laser polarization in such a way that the high momentum end nitrogen and oxygen species move in opposite directions. The multiply ionized breaks up channels were identified, and a 3D visualization developed in order to cope with the nature of the correlation. As well as identifying the channels present, the method showed that structure could be deduced from the shape of correlation islands. Having a small momentum, the middle nitrogen ion follows the end nitrogen ion during the break up and forms a narrow correlation island on the map.

However, for a bent molecule like SO_2, broader correlations were produced indicating higher contributions of the middle O ion to the net momentum of the process.

The Cornaggia and co-workers studied the laser induced fragmentation of CO_2 using 150 and 130fs laser pulses of 790 nm wavelength and up to 2×10^{16} W/cm^2 intensities at the CEA/DSM/DRECAM laser facility [21], [47] [60], [61]. They used a Wiley and McLaren [29] double chamber ion TOF spectrometer. The ion signal was detected by microchannel plates just as with Frasinski's work. Geometrical structures of CO_2 cations exactly before Coulomb explosion were studied by this group. The study was based on distribution patterns in a covariance map (referred to as a correlation map) of fragment ions by stripping of up to 9 electrons in order to examine Coulomb explosion into multi-charged atomic ions. Using triple ion correlation experiments, several fragmentation channels O^{a+} + C^{b+} + O^{c+} were identified. They extended the approach of the Reading group by simulating the Coulomb explosion of the molecule from distributions of molecular parameters such as bond lengths and bend angles [21]. They modified the distributions to generate simulated correlation islands which matched the experimental data. From this they were able to deduce that the molecules undergo a large amplitude bending motion during the ionization process as shown in Figure 2-25.

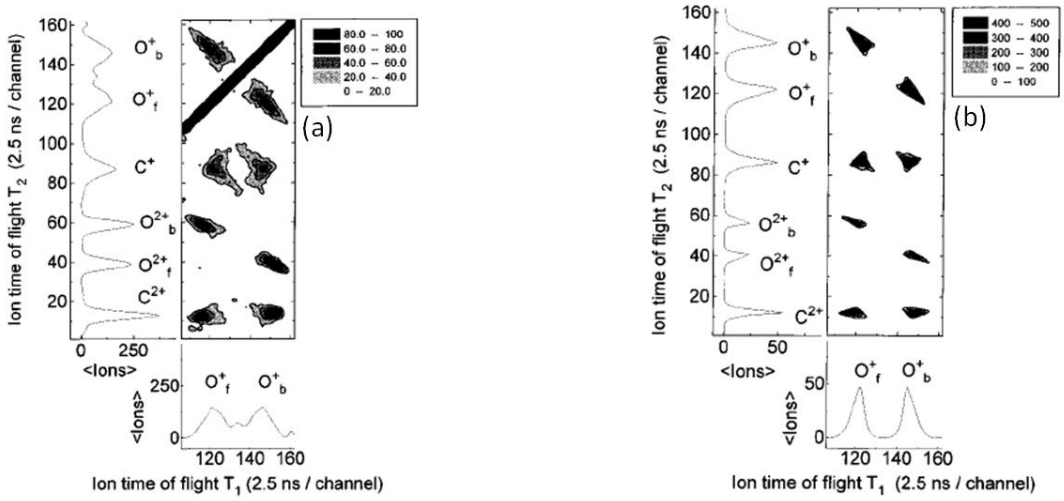

Figure 2-25 Experimental and simulated double correlation plots for the (1, 1, 1) channel of CO_2 (Reprinted with permission from [21])

2.5.2 Mass resolved momentum imaging (MRMI)

The second method which revealed considerable information about molecular structure and dynamics was the uncorrelated MRMI technique developed by the Yamanouchi group from the University of Tokyo. This method focuses on visualizing the momentum vector distribution of mass selected fragment ions with respect to the polarization vector of the laser. The MRMI maps can be made from

the TOF spectra of a molecule's fragment ions recorded while they changed the polarization direction of the laser light with respect to the TOF mass spectrometer for different angles.

They successfully employed this methods for a number of diatomic molecules, such as N_2 [58] [62], but the method was particularly useful for polyatomic molecule, such as SO_2 [58].

Using the MRMI method, Hishikawa and co-workers [63] studied the geometrical structure of exploding CO_2^{3+} in a focused laser pulse (29 μm) giving an intensity of 1.1×10^{15} W/cm^2, 100-fs pulse (λ=795 nm, 0.74 mJ). They made the MRMI map from the TOF spectra of CO_2 fragment ions recorded while they changed the polarization direction of the laser light with respect to the TOF mass spectrometer for 18 different angles. Because the acceptance angle of the detector was very small, only ions with initial momentum in the direction of the detector were detected. The momentum maps were then generated by calculating the fragment momentum component in the direction of the detector for each angle.

The experimental results of MRMI maps for the fragment ions, O^{p+} (p=1-3) and C^{q+} (q=1-3) produced after the Coulomb explosion of CO_2 are depicted in Figures 2-26. Figure 2-26 (a_1) shows The MRMI maps for the O^+, O^{2+}, and O^{3+} ions. As can be seen a pair of symmetrical crescent distributions with a center at the zero-momentum position suggesting that these O^{p+} ions tend to be ejected along the laser polarization direction. Figure 2-26 (b_1) shows the MRMI maps resulting from the C^{q+} fragment ions showing an elliptical distribution extending perpendicular to the laser polarization with a peak at zero momentum. This indicates that these ions gain only small released momenta even though they are formed from the highly charged parent ions. This result confirms that C^{q+} fragment ions are being ejected from molecules which are almost straight and are aligned with the laser polarization direction.

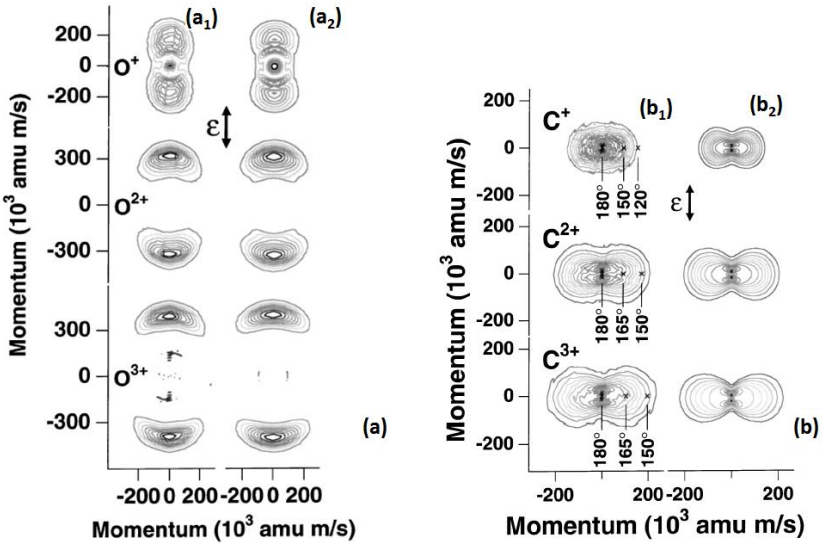

Figure 2-26 (a) The MRMI maps for O^{p+} (q = 1-3) and (b) for C^{q+} (q = 1-3) fragment ions produced through the CE of CO_2 plotted against the polarization vector (ε) of the laser pulse: (a_1) and (b_1) the observed results, (a_2) and (b_2) best fit MRMI map synthesized by the simulation (Reprinted with permission from [63])

They also used the method of Cornaggia to generate simulated momentum maps from distributions of bend, alignment and bond length functions fitting these parameters to generate maps.

As can be seen in Figure 2-26 (a_2) and (b_2) the TMU group was able to generate simulated MRMI maps which matched well with the experimental ones, they found that the C-O bond length is stretched to about 1.7 Å and the mean amplitude of bending is ~20º but was peaked at 180º.

The UCL group of Newell had simultaneously developed this method of deducing crude distributions for bond length, bend angle and alignment angle, but with a corrected MRMI method which compensated for the bias toward zero or low momentum fragments [59]. They were able to show that for 50 fs pulses, H_2O exploded from geometry substantially straighter than from equilibrium. They followed this up with an experiment on CO_2 [59] which showed that bending occurred of the straight molecule, a result which was somewhat in agreement with Cornaggia [47] but not the work of the Yamanouchi group.

At the start of the new millennium there was a significant breakthrough in the technique of molecular imaging using femtosecond laser pulses. The Tokyo group used a 60 fs, 800 nm, and 0.18mJ/pulse laser pulses and focused into an ultrahigh vacuum chamber by a quartz lens of 200 mm focal length resulting in spot size of 32 μm and an intensity of 3.6×10^{14} W/cm^2 [64]. A DC electric field was

used to guide the ions produced through the interaction of the laser field to a time and position sensitive detector. Using this data the authors calculated the momentum components of each fragment along the x, y, and z direction. From the TOF mass spectrum of the fragmented CS_2 they observed two strong peaks corresponding to CS^+ (4.6 μs) and S^+ (3.9μs) with weaker peaks assigned to C^+ (2.4 μs) and S^{2+} (2.7 μs). These fragment ions were produced through a two-body ($CS_2^{p+} \rightarrow CS^{q+} + S^{r+}$ (p = q + r)) or three-body fragmentation ($CS_2^{p+} \rightarrow S^{q+} + C^{r+} + S^{s+}$ (p = q + r+ s)) process. The apparatus allowed the group to employ coincidence imaging methods as had only previously been carried out for HCI impact. This allowed them for the first time to identify specific single explosion events and isolate all of the fragmented ions produced through a Coulomb explosion of a parent ion with a specific charge state. From the single pathway imaging map of the S^+ fragment, they observed that prior to Coulomb explosion the parent molecular ions aligned in the polarization direction. In previous work in the angular distribution of S^+ a strong isotropic component was observed. However, coincidence images of the S^+ showed a sharp angular distribution with little isotropic component [22]. They were also able to measure the distributions of KER for different process. Figure 2-27 shows the distribution of the KER for three different pathways (1, 1), (1, 1, 1), and (1, 1, 2) that produce C^+, S^+, and S^{2+} fragment. In this figure the spreading of the structural distributions for (1, 1, 1) and (1, 1, 2) channels just before fragmentation can be inferred by wider distribution.

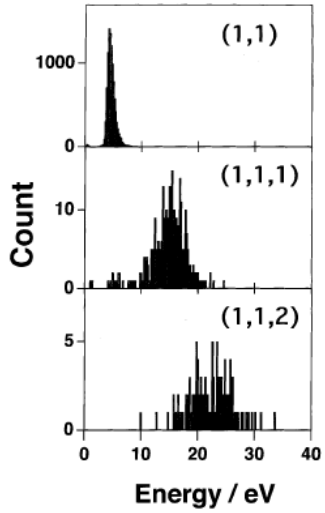

Figure 2-27 KER distribution for the (1, 1), (1, 1, 1), and (1, 1, 2) CE pathwats odtained directly from the determination momenta of the fragment ions (Reprinted with permission from [64])

This work also attempted to reconstruct the molecular structure of CS_2^{3+} prior to Coulomb explosion. This was done using a fitting algorithm to find the geometry for each event which best fit the final momentum of the fragment ions. Figure 2-28 shows the experimental result for structural distribution of CS_2^{3+} prior to coulomb explosion. This figure shows extensive geometrical deformation of CS_2^{3+} from the neutral CS_2 in the $X^1\Sigma_g^+$ state (open circle). This can be inferred by comparing the measured bond angle (145º) with the calculated one (174º) for the CS_2 neutral [65].

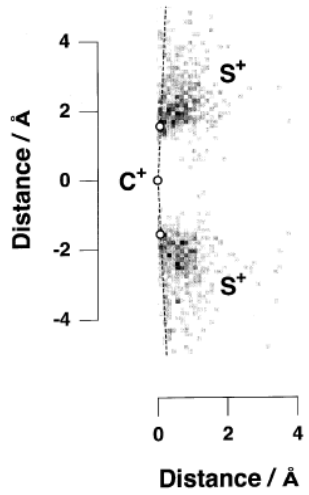

Figure 2-28 The geometrical structure of CS_2^{3+}, the open circle represent the geometry of CS2 in the electronic ground $X^1\Sigma_g^+$ state (Reprinted with permission from [64]).

One year later, using the same facility and setup (60 fs pulse duration) the group again studied the three-body Coulomb explosion of CS_2 [22]. By using the triple-coincidence technique and measuring all fragment ions momenta in coincidence they were able to derive the parameters χ and θ_v and as previously defined for HCI impact.

Corkum and co-workers in NRC Ottawa employed a Ti: sapphires 40fs laser pulse at 800nm wavelength 500 Hz repetition rate compressed to 7fs using an argon-filled hollow core fiber followed by dispersion compensation with chirped mirrors [23]. They used this technique to determine the 3D structure of both D_2O and SO_2. Using classical mechanics and an atomic tunneling model, the authors simulated the break up of D_2O and SO_2. They also compared the experimental results from their time and position sensitive detection system with the calculated results.

Figure 2-29 and Figure 2-30 presents the measured and calculated structures from the *ab initio* potential for D_2O and SO_2 using 8 fs pulses [23]. Figures 2-29 (a) shows the reconstructed geometry of D_2O and Figure 2-29 (b) and (c) show the experimental and calculated distributions of bond length

and bend angle The dotted curves represent the distributions for the ground stationary state structure of D_2O, that is R_{OD} = 0.96 Å and Θ = 104.5°. As can be seen in using the Coulomb potential for reconstruction, R_{OD} peaks at 1.26 Å and Θ = 117°. The *ab* initio and Coulomb potentials yield nearly identical results for 8 fs laser pulses. The authors also carried out the experiment with 40 fs pulses and found R_{OD} = 1.96 Å and Θ = 138° which is in a good agreement with the 50fs results of H_2O obtained by Sanderson et al. [59]. As a result, they concluded that a few-cycle laser pulse visibly improves the measurement of molecular structure.

Although during ionization motion of the molecule happened, they found that to realize the change in length scale of bond length the image accuracy is still acceptable.

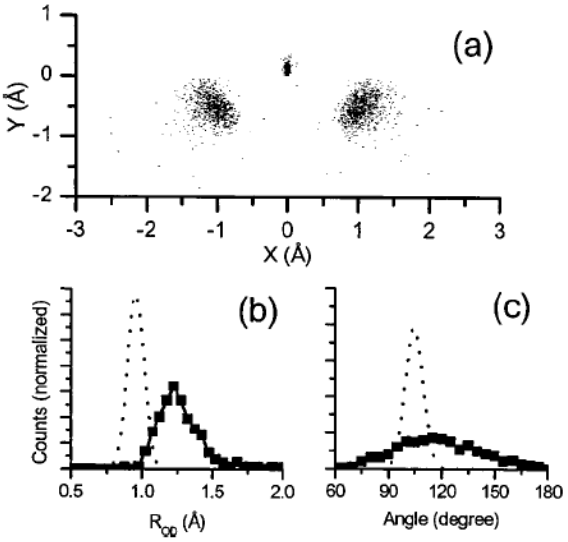

Figure 2-29 (a) Structure of D_2O using the 4+ charge states; *y* axis is the bisector of the angle, (b) Radial distribution, (c) Angular distribution, and the dotted curve represents expected stationary state structure (v = 0) of D_2O (Reprinted with permission from [23]).

Figure 2-30 (a) and 2-30 (c) show the measured R_{SO} and Θ distributions. The known stationary state geometry parameters for SO_2 are R_{SO} = 1.43 Å and Θ = 119.5°. Considering a Coulomb potential for the 7+ charge state, the Corkum group obtained mean structural values of R_{SO}=1.67 Å and Θ=111°. It is worthwhile to note that Hishikawa [58] and coworkers had earlier used 50 fs laser pulses and measured the structural constants of R_{SO}=3.3 Å and Θ_{OSO} =130°. As with the case of D_2O this comparison shows the ability of sub 10 fs pulses to reveal near equilibrium geometry through Coulomb explosion. Comparing the result of [66] [67] the authors noted that the molecule containing

the lighter constituents was more closely imaged than the more massive molecule. They noted that although molecules containing heavier nuclei might be expected to be easier to image using laser-induced Coulomb explosion, because they have more inertia and so begin to deform more slowly during the rising pulse of the laser, in general this is not the case.

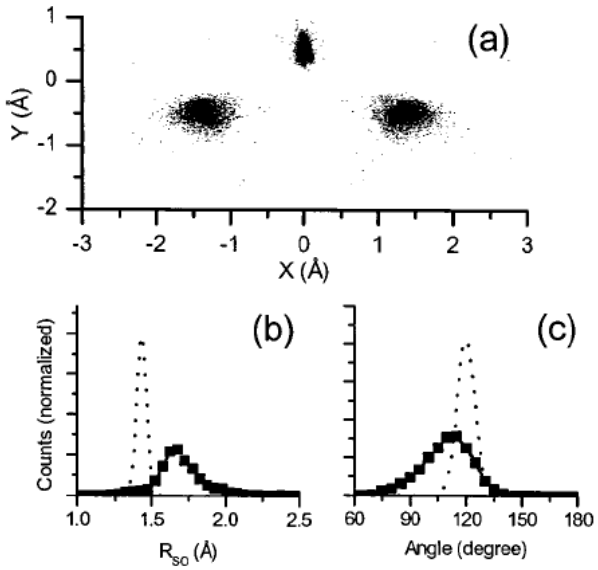

Figure 2-30 (a) Structure of SO_2 using the SO_2^{7+} charge states, The reconstruction is achieved using the Coulombic potential; The *y* axis is the bisector of the angle, (b) Radial distribution, (c) Angular distribution, and the dotted curve represents expected stationary state structure (v = 0) of SO_2 (Reprinted with permission from [23]).

Later the Hishikawa group in the Institute of Molecular Science (IMS), Nagoya [68] employed the coincidence momentum imaging of fragment ions to study the coulomb explosion dynamics of H_2S.they used an intense laser field with short pulse duration of 12fs and intensity of 2×10^{14} W/cm^2. The different electronic and nuclear responses of this system were investigated as a function of the laser polarization in the molecular frame. The molecule is assumed fixed with respect to electric field polarization ε. In fact, the effect of the molecular rotation and laser induced alignment in a few cycle laser pulses are neglected. This assumption is based on the comparison of the time H_2S molecule requires to rotate along one of its x, y, and z axes (e.g. T_{rot} = 0.7, 0.5, and 0.5ps), which is larger than the pulse duration (t<<.1ps).

In this study, position sensitive detection is once again used in order to measure the momenta for each fragment ion, i.e. P_1, P_2, and P_3 and triple coincidence map (P_1-P_2 where P_1 and P_2 are the momenta of

the terminal ions), is used to determine dynamics. According to this kind of coincidence map, a distribution along the diagonal line ($P_1 = P_2$) indicates a concerted breakage of the two S-H bonds. These results led to construction of a map encompassing diagonal coordinates versus the fragment momenta P_1 and P_2. In this way, the effect of the electric field polarization and molecular axis direction on ionization yields can be studied. Figure 2-31 (a) represents schematic view of the H_2S molecule, while Figure 2-31 (b) illustrates more detailed orientation of the molecule plane (x is normal to y-z molecular plane) against the polarization direction (spherical coordinates of θ_p, φ_p). Figure 2-31 (c) and 2-31 (d) show the distribution of θ_p, φ_p, respectively.

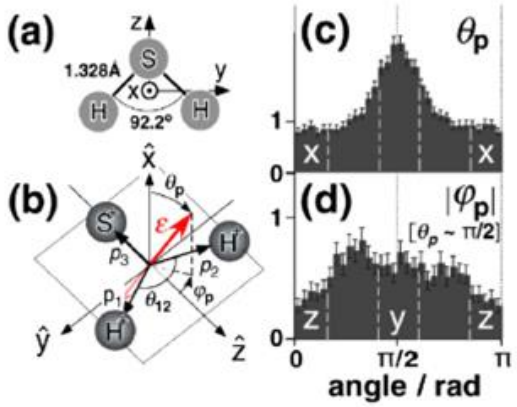

Figure 2-31 (a) Geometry and molecular axes of H_2S in the electronic ground state, (b) Molecular frame defined by the fragment momenta, p_1 and p_2. Vector ε is specified by the spherical coordinates, θ_p and φ_p to show the direction of the polarization. (c) Distribution of θ_p. The relative yields are indicated in the vertical scale. The error bars represent the statistical uncertainty (Reprinted with permission from [68]).

Results for relative ionization yields at x, y, and z directions (1, 4, and 1.6) shows that the direction of the polarization of electric field essentially affects the electric field response.

Figure 2-32 represents the dependency of the nuclear dynamics on the direction of electric field by plotting the variation of momentum angle θ_{12} between P_1 and P_2 and the KER (E_{kin}) for different molecular planes. The results were compared to theoretical results of a model developed by Schmidt and co-workers [69]. The theoretical data is based on classical simulation of the neutral H_2S undergoing a Coulomb explosion in ab initio Potential Energy Surface (PES) of H_2S^{3+}. The second-order Møller-Plesset perturbation theory was used to calculate the potentials using GAMESS program [69].

It has been observed that the experimental data is in accordance with the simulation results for the electric field along with the x axis (θ_{12} = 114º and E_{kin} = 23.6eV) i.e. out of the plane of the molecule, where no signal is observed for long pulses, this indicates the correctness of the first assumption (molecules being frozen during the interaction). For ε directed in z or y axis (in the plane of the molecule) KER decreased to 15eV indicating a stretch in bond length (R = 2.5Å) to twice the size of equilibrium.

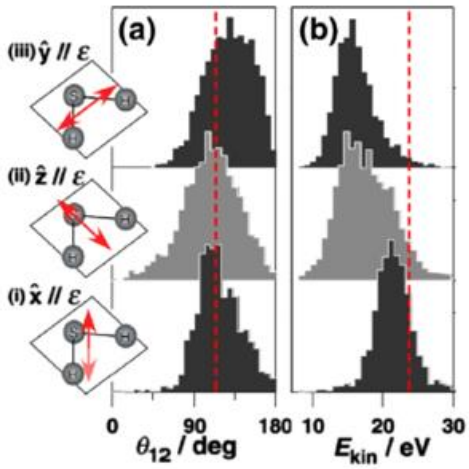

Figure 2-32 (a) Momentum angle θ_{12} distribution and (b) KER (E_{kin}) distribution obtained for three different directions of ε in the molecular frame. Each distribution is normalized at the peak. The dotted lines indicate the θ_{12} and E_{kin} values obtained by a classical simulation of the CE on the *ab initio* PES, θ_{12} = 114º and E_{kin} = 23:6 eV, which are smaller than those expected from the corresponding Coulombic PES, θ_{12} = 124º and E_{kin} = 29:2 eV (Reprinted with permission from [68]).

Matsuda and co-workers [24] studied the Coulomb explosion of the Ozone gas (O_3) with 40 fs pulses, 800 nm, and repetition rate of 1 kHz. This beam was coupled by an optical lens (f = 1200 mm) into an 800-mm-long hollow fiber (core diameter 500 μm filed with Ar gas) to produce 9 fs pulses. They fixed intensity of the laser for both 9 and 40 fs laser fields around 2×10^{15} W/cm^2.
The fragment ions produced by the Coulomb explosion process, $O_3^{3+} \rightarrow O^+ + O^+ + O^+$, were once again detected in coincidence by a position sensitive detector with delay-line anode and the kinetic energy of the fragments were then determined in the lab frame for every event in the Coulomb explosion process.

The authors employed the Dalitz plot method to study the experimental and simulated data. In the case of 40 fs, the authors observed a decrease in the KER, and a broadening in the Dalitz plot distribution. As a result this observation, they concluded that the geometrical structure of O_3 almost does not go under any changes during the interaction with the 9 fs pulse duration. On the contrary, in the case of 40 fs intense laser fields a significant structural deformation along all the three vibrational coordinates, including the antisymmetric stretching coordinate happened.

Figure 2-33 composed of several Dalitz plots. Figure 2-33 (a) illustrates radial and angular momentum correlation between all three O^+ fragment ions. As can be seen, when the angle between each fragment ion is 120°, the momenta of the three fragments are equal in magnitude. The magnitude and angle change in different areas of the plot. Because the three fragments are equivalent the plots have a triple rotational symmetry.

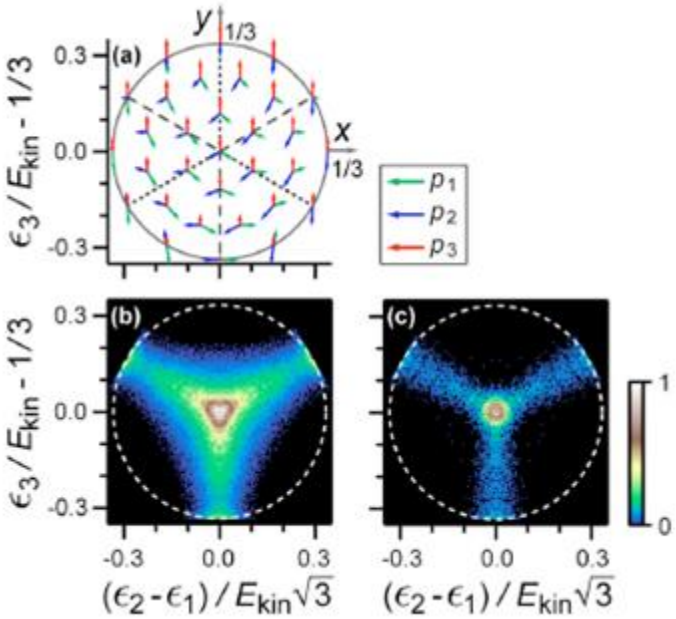

Figure 2-33 (a) Momentum correlation expressed in the Dalitz plot. (b) Dalitz plot distribution of the three-body Coulomb explosion of O_3, $O_3^{3+} \rightarrow O^+ + O^+ + O^+$, simulated with randomly generated geometrical parameters ($r1$ = 1.0 Å, $r2$ = 5.0 Å, and $\gamma \leq 0°$-180°). (c) Simulated distribution for nearly symmetric structure with $|r_a| \leq 0.05 r_s$, where $r_a = r_1 - r_2$ and $r_s = (r_1 + r_2)/2$ (Reprinted with permission from [24]).

Figure 2-33 (b) shows the result of numerical calculation of the energy released for the three-body Coulomb explosion of O_3 in randomly generated geometrical patterns (bond lengths and bond angles) by solving the classical equation of motion. A sharp peak can be seen at the center of the plot due to the dependence of the angle between the momenta of the two terminal O^+ ions on the bond angle of the initial geometry. Figure 2-33 (c) shows a similar simulation except it has a predefined symmetric structure (bond length and angles are symmetric). These two plots illustrate the effects of the asymmetric stretching of the two O–O bonds and the bending of the O–O–O angle. The absence of the statistics for $y > 0$ shows that for the geometry of equal bonds the angle θ between two terminals O is always larger than 117º.

J. P. Brichta and co-workers at University of Waterloo in 2007 [70] used 50 fs laser pulses (800 nm, 350 μJ, 1 kHz) focused by a parabolic mirror ($f = 2.1$ cm, $\varphi = 14$ mm) to an intensity of $\sim 10^{15}$ W/cm^2. The work used a standard time and position sensitive setup but utilized with a MBWC anode [29] [59] [71] with a kHz laser system for the first time.

Recording KER for several channels they demonstrated that enhanced ionization was dominant at 50fs and compared the bond lengths with a classical prediction of enhanced ionization using over the barrier ionization. Although the results did not match exactly there was some similarity between the predicted and measured change in bond length R with channel.

The energy distribution data for the six explosion pathways is depicted in Figure 2-34.

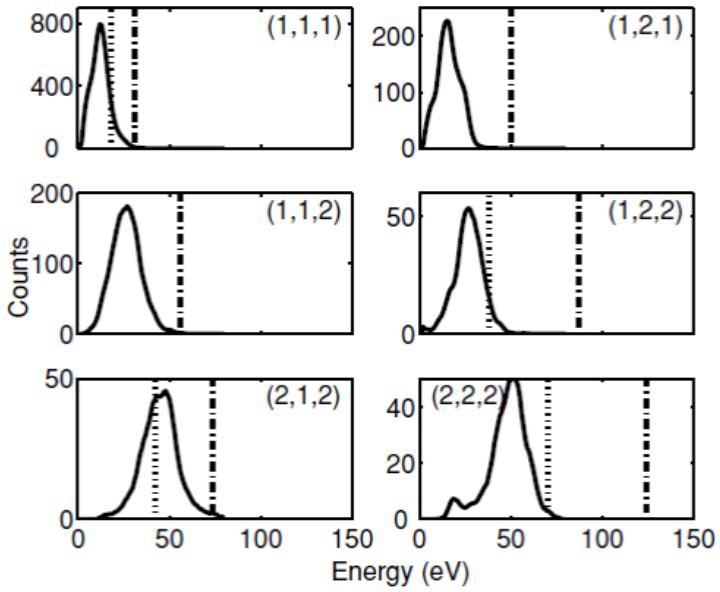

Figure 2-34 KER distributions for the (1, 1, 1) to (2, 2, 2) channel CE pathways; includes KER values (dotted), calculated KER (dot-dash) (Reprinted with permission from [70]).

The authors compared the experimental data with the KER data previously obtained by Bryan and coworkers [72], and with the calculation results of the KER which consider the ground state of the neutral CO_2 as the initial geometry of the molecule. They found that the calculated KER is slightly higher than the KER obtained in this experiment. This comparison shows an agreement for the channels in which the carbon fragment has been ionized singly. The presence of a low energy shoulder in (1, 1, 1) signal, a high energy shoulder in (1, 2, 1), and a low energy feature in (2, 2, 2) close to the noise level is of the interest in this data set. As the statistics for (1, 1, 1) and (1, 2, 1) is more compelling than (2, 2, 2), the latter might be overestimated. Comparison with Bryan's results [72] also features the lower KER of these results for channels with doubly charged carbon fragments. Moreover, double ionization of oxygen fragment, e.g. (1, 1, 2), results in increment of measured KER. Nevertheless, it is not to the extent of double ionization of the carbon fragment, e.g. (1, 2, 1).

2.5.3 Pump Probe Dynamics

Study of molecular dynamics can be enhanced using laser-initiated CEI combined with pump-probe. The mechanism of action in this method is based on initiation of the dynamics with a femtosecond laser pulse, by ionizing the molecule to low charge state followed by a second delayed higher intensity short pulse which removes several more electrons to initiate a Coulomb explosion serving as the probe. Both of the pulses must be very short, e.g. with few cycles of ~ 8 fs, as longer pulses will produces "unclear" dynamics similar to that produced by a camera with a slow shutter speed.

The National Research Council group in Canada has studied dynamic imaging of the molecules such as N_2, O_2, and D_2 using ultrafast laser pulses and attempted to measure their rotational wave packets [73]. More importantly, the pump-probe technique was used by Légaré and coworkers to get more insight into the D_2 and SO_2 molecular dissociation dynamics [73], [74]. They used an 8 fs hollow fiber laser system with two intensities of 3×10^{14} W/cm^2, and 1×10^{15} W/cm^2. The pump pulse created $D_2^+ X^2\sum_g^+$, SO_2^{2+} and SO_2^{3+} parent ions. The probe pulse intensity was 5×10^{15} W/cm^2 and the delay was varied from 0 fs to 220 fs, creating charge state of SO_2^{7+}.

In the case of SO_2 They identified three features in the energy plot while studying KER of the correlated oxygen fragments. The first one was referred to as the lower energy feature. In this feature, a concerted three body fragmentation of the molecule resulted in similar energies for oxygen species as $E_{O1} \sim E_{O2}$. The second one referred to as the off-diagonal features. Here, sequential fragmentation of the molecule leads to dissimilar KER released of the oxygen species such that $E_{O1} > E_{O2}$ or vice versa. It was confirmed that there exists two concerted channels; $SO_2^{3+} \rightarrow O^+ + S^+ + O^+$ and $SO_2^{2+} \rightarrow O^+ + S^+ + O$.

In other work by the authors, the geometry of the SO_2 was estimated to be R_{SO} = 1.7 Å and θ = 120Å (equilibrium geometry of SO_2 R_{SO}=1.43Å and Θ=119º). Herein, Figure 2-35 represents the geometry of the SO_2 molecule in a pump-probe test carried out with three different delay times. As can be seen in Figure 2-35 (a) the delay time has been set to 0fs. The result shows that using few-cycle laser pulses, structural deformation of the light atoms, which is expected to be induced by enhanced ionization, can be hindered.

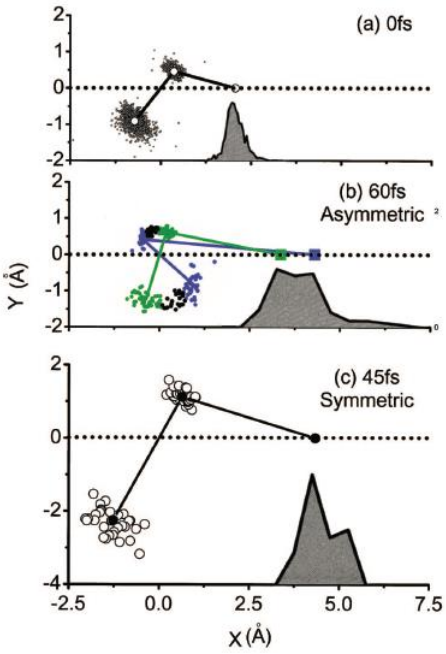

Figure 2-35 (a) Structure of SO_2 for final charge state SO_2^{7+}, (2, 3, 2) channel, (b) Structure of SO_2^{2+}, (1, 1) channel, undergoing asymmetric dissociation at t = 60 fs; blue: average structure for bond angle < 50°, green: bond angle > 75° for final charge SO_2^{7+}, (c) structure of SO_2 in the concerted dissociation (2, 3, 2) channel at t = 45 fs, also shown is the equilibrium structure of SO_2 (final charge is SO_2^{10+}, $I_{pump} = 1\times10^{15}$ W/cm^2, $I_{probe} = 5\times10^{15}$ W/cm^2 (Reprinted with permission from [74]).

The symmetric and asymmetric dynamics of SO_2 have also been depicted in figures 2-35 (b)-(c), respectively. For the asymmetric break up of $SO_2^{2+} \rightarrow O^+ + SO^+$ with 60 fs delay time, θ=70º, R_{SO} =2 Å and the distance between fragments was ~3.7 Å. Symmetric three-body break-up of the $SO_2^{3+} \rightarrow O^+ + S^+ + O^+$ showed quite different response where, R_{SO} = 4.1Å and θ= 100º, shown in Figure 2-35 (c).

Obtaining such information is not possible using the techniques which have been explained in the previous sections, such as Spectroscopy, Beam foil, and HCI impact Coulomb explosion.

Chapter 3
Experimental Setup, Apparatus, and Techniques; Data Acquisition and Analysis

3.1 Introduction

In this chapter we present the entire experimental setup used for Coulomb explosion imaging of molecules. In addition we describe the essential techniques used. First, the laser facility and the techniques for generating short pulses of 7 fs for conversion of 800nm are discussed. Secondly, a description of the supersonic source, vacuum chamber, and the TOF mass spectrometer will be discussed. Finally, the system of electronics used in the time and position sensitive detection system will be described and the data collection and analysis methods summarized.

3.2 The Laser System

The experiments were performed at the Laboratory of the Advanced Laser Light Source (ALLS) research facility in INRS-EMT in Varennes, Quebec, Canada. Schematic view of the short pulse generation laser system in ALLS is represented in Figure 3-1. A CW 10 W Diode pumped solid state (Verdi, Coherent) was used to pump an oscillator (KM) equipped with a Titanium-Sapphire crystal (Figure 1(a)) to generate 6-9 nJ energy, 10 fs pulse length, and 80 MHz repetition rate, at 800 nm wavelength in order to seed the amplifier. To intensify the laser pulse we use a Red Dragon (KMLabs) Titanium-Sapphire (Ti -Saph) amplifier laser system.

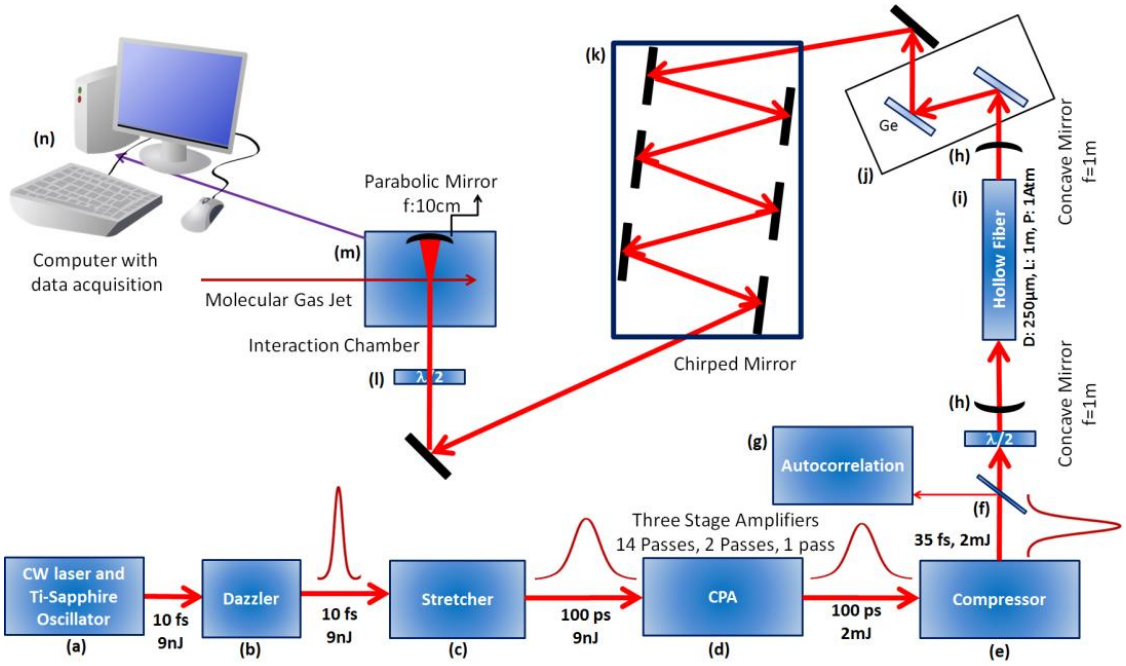

Figure 3-1: The schematic view of the laser facility at ALLS, laser pulse generation set-up (a-l), interaction chamber (m), and data acquisition system (n).

3.2.1 Amplifier

The energy range of resultant laser pulse from the oscillator in (Figure 3-1(a)) is 6 to 9nJ. This energy must be intensified as it is not high enough to be used in most laser applications. The chirped pulse amplification method (CPA) (Figure 3-1(d)) is therefore an essential component of the laser system [4] . The first stage of this process is the stretcher system (Figure 3-1(c)) so that peak power intensity is kept low ensuring that the Ti: Sapphire crystal in the amplifier is unharmed. For a high energy system (>1mj) it is essential to use gratings to introduce dispersion and stretch the pulses. For this purpose, a double-passed grating pair was used to stretch the duration of the seed pulse to about 100 picoseconds, by producing a negative dispersion to the output pulses from the oscillator. The CPA method, then, can be achieved when the stretched laser pulse passes through a Ti: sapphire crystal in a Brewster-cut angle, pumped by a CW laser, several times. The Red Dragon system employs the multipasss system. Because it introduces minimal material dispersion it has an advantage over the popular regenerative type of amplifier. There are three multipass amplifiers, the first one with 14 passes, second with 2 passes, and the third with a single pass, the system is pumped by a 30W diode pumped Nd: YLF laser (Evolution, Coherent) Combined these can produce energy up to 5mj per

pulse with repetition rate up to 5 kHz. In order to compress the pulses the laser system employs a parallel grating pair (Figure3-1(e)). The combined stretcher and compressor system can compensate for dispersion up to fourth order to produce pulses of the order of 25-35 fs. To achieve a shorter pulse, the negative dispersion in the stretcher and the positive dispersion in the compressor must be matched well. The regulated pulse length can be varied by either adding or subtracting the second order dispersion. Although this can be done by adjusting the compressor spacing, an Acousto-optical modulator, so-called Dazzler (Fastlite), is also incorporated to the system between the oscillator and stretcher where the peak power is low (Figure 3-1(b)). This device can introduce a set amount of dispersion either to compensate for any residual high order dispersion still remaining after the compressor, or to achieve the shortest pulse duration, to stretch the pulse by a set amount or to precompensate for dispersion in the lens, half wave plate 1, beam splitter, and the window of the hollow fiber compression system.

The beam's power is typically attenuated further to 1.7 W with a beam splitter (Figure 3-1(f)) which can also be used to send pulses to the autocorelator (Figure3-1(g)) in order to measure the pulse length.

3.2.2 Hollow Fiber

Further shortening of the pulse duration, down to 10-fs, requires the use of a hollow fiber filled with noble gas compression system. This technique is based on spectral broadening caused by the nonlinear influence of waveguides which are filled with a noble gas. This method relies on nonlinear propagation effects which occur in the medium at high intensity. According to Fourier-transform-limited pulse ($\Delta t \Delta \omega \geq 1/2$), it is necessary to use a broad spectral bandwidth in order to produce a very short pulse. The broad spectrum produced in the hollow fiber because the nonlinear refractive index n_2 varies across the temporal profile of the pulse, which causes the appearance of new frequency components; this is known as self-phase modulation. For Ar gas ($n_2 = 2.5 \times 10^{-23} m^2/W$) at 1.2 atmosphere we can expand the 60 nm bandwidth of the compressor output up to 250 nm. We use two 1 meter concave silver mirrors in our setup, one before the hollow fiber and the other after (Figure 3-1(h)). The hollow fiber has been designed in a way that has the internal diameter of 250 μm and length of 1 m (Figure 3-1(i)). The fiber is made up of a fused silica capillary tube which is supported on an aluminum V-groove. As the pulse passes through the fiber, the input and output windows, several meters of air and the window of the experiment they experience material dispersion which stretches the pulse. In our study a set of commercially available chirped mirrors - multilayer/multi-

thickness coated- and two fused silica wedges (Femtolasers, Vienna, Austria) were used to compensate the dispersion (Figure 3-1(k)) [4]. Because the nonlinear process in the hollow fiber is dependent on the intensity in the gas, we vary the output intensity only in order to conduct experiments with the same few cycle pulse length but different intensity. This is achieved with half wave plate 1 which rotates the polarization of the light in the hollow fiber; this is then combined with the two germanium plates fixed at the Brewster Angle (Figure 3-1(j)) which acts as linear polarizers to select energy.

If long pulses are desired the hollow fiber is either evacuated or filled with helium ($n_2=1.4\times10^{-24}m^2/W$) which does not cause self-phase modulation. This keeps the laser profile and beam direction constant so that the focal conditions in the chamber do not change.

3.2.3 Laser delivery to the target

The last stage of the laser system is to guide the few cycle pulse beam to the interaction chamber. In the ALLS facility, the laser pulses are focused by a parabolic mirror (f = 10 cm) to obtain the minimum spot size (without spherical aberration) which is crossed with a supersonic jet gas (Figure 3-1(m)).

The Raleigh range parameter (Z_R) should be taken into account in case one intends to determine the distance at which the well collimated beam is focused in the focal point [75], [76]. In fact, the radius diverges by a factor of $\sqrt{2}$ by passing the distance Z_R (Figure 3-2). In this figure θ is the divergence angle of the beam, R(z) is the radius, W_0 represents the waist radius at z = 0, and $\sqrt{2}W_0$ shows the radius of the beam waist at Z_R.

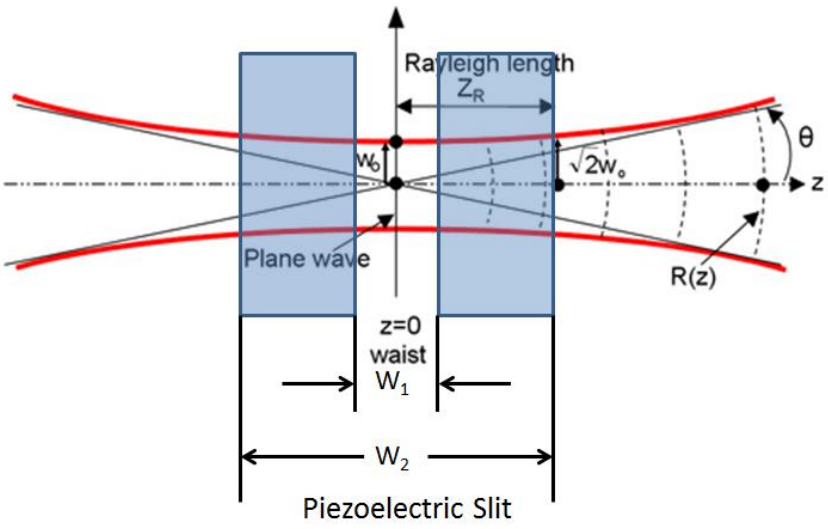

Figure 3-2: Schematic view of laser focus point and motorized piezoelectric slit position

The Raleigh range may shrink to a few micrometers in case the beam is strongly focused (3.1).

$$Z_R = \frac{\pi W_0^2}{\lambda} \tag{3.1}$$

The collimated W might be linked to the focal length of the concave mirror when the initially collimated beam becomes focused with a focal length f through a mirror or lens. This can be validated according to the equation below:

$$W = \lambda f / \pi W_0 \tag{3.2}$$

In this equation λ is wavelength, f is the focal length and W is the beam waist.

3.2.4 Pulse Duration Measurement techniques

We employed the autocorrelation technique using a single shot autocorrelator to measure the pulse duration. As the autocorrelation apparatus and the main chamber are distant, pulse duration varies due to dispersion in air and also other parts of the system (e.g. silica and glass windows) located in the pathway and interacting with the original pulse. However by measuring the KER spectrum of D_2 one can monitor the pulse length in the vacuum chamber [66] [77]. In this method, the shortest pulse duration is known to correspond to the highest CE energy observed in the KER spectrum. The technique is applied to manipulate the pulse to optimize the short pulse duration. This is typically applied while varying the separation of the wedges or the number of bounces from the chirped mirrors.

3.2.5 Vacuum chamber source and supersonic facility

In this section the Coulomb explosion apparatus (Figure 3-3) will be discussed: the source, intermediate and interaction chamber, and motorized slit. In order to image molecules one at a time it is necessary to perform experiment in vacuum. This can be realized by focusing a laser beam in a medium. To facilitate these conditions, three vacuum chambers are used.

Figure 3-3: A photograph of ALLS laser and chamber facility

A schematic side view and top view of the Coulomb explosion and electron diffraction apparatus is depicted in Figure 3-4. The top view shows the role of supersonic jet gas component more precisely. The side view of this figure provides the whole setup includes three chambers the source, intermediate, and interaction chamber. 1 mm-diameter electroformed nickel skimmers separate the source and interaction chamber.

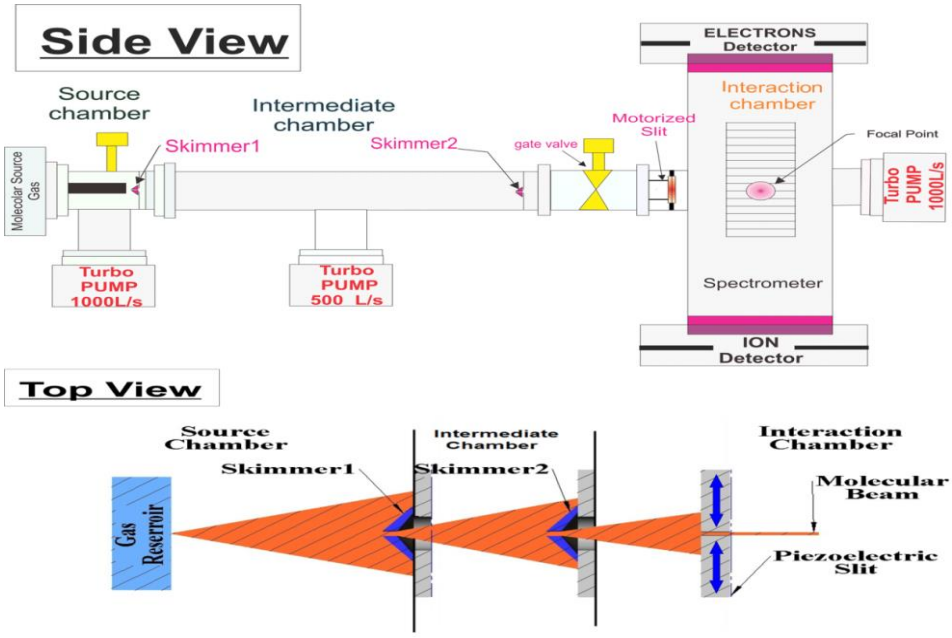

Figure 3-4: Schematic detailed view of supersonic gas jet facility, (a) side view and (b) top view for the whole set up.

Although all these three chambers are connected they can easily be separated if needed. All these three chambers provide a suitable condition for interaction of a laser beam and a supersonic jet of a molecular gas. The interaction chamber contains the TOF mass spectrometer, incorporating a micro chanel plate (MCP), and PSD.

3.2.5.1 Source chamber

A turbo molecular pump backed with a dry scroll pump mounted on the source chamber provides a base pressure of 10^{-9} Torr and a high pumping speed of 1000 l/s. inside the source chamber, the molecular source consists of a small enclosed space connected to an external gas reservoir. A pinhole of a few microns (30µm), maintains a pressure difference between the source and the source chamber of around five orders of magnitude. This pressure difference generates a high speed narrow velocity distribution gas stream toward the skimmer. The diameter of the gas jet is reduced when it passes through the first 1mm skimmer.

3.2.5.2 Intermediate chamber

An intermediate chamber pumped by a high speed turbo pump (500 l/s) and backed by a dry scroll pump is used to provide differential pumping between the source and interaction chambers. The second skimmer mounted between the intermediate and interaction chamber selects the central portion of the molecular jet. The resultant jet after the skimmers is a highly collimated beam with an effective transverse translational temperature of Kelvin (K).

3.2.5.3 Interaction chamber

The interaction chamber is pumped by a second 1000 l/s turbo pump backed by a dry scroll pump. After baking the chamber reaches a base pressure of 10^{-10} Torr, this ensures that number of background gas molecules in the interaction region is kept to a minimum. A motorized piezoelectric slit is mounted on the flange which separates the intermediate chamber and the interaction chamber. This motorized slit is used to adjust the width and the axis of the gas beam. In fact, manipulation of this slit results in shrinkage of the width of the jet width confining it within the confocal parameter. Decreasing the window width improves the profile. The voltage chosen on the piezoelectric slit to close it by 90% was chosen to optimize as the window. Figure 3-2 shows a schematic view of the interaction of the very narrow molecular jet (using slit) with the most intense area of the focal point of the laser pulse. Here W_1 is the active open width and W_2 is the fully open width of the slit.
This very narrow molecular beam provides two key benefits for high intensity laser experiments using Coulomb explosion imaging. Firstly, molecules can be confined almost entirely to the highest intensity region of a tight laser focus [78]. This can significantly reduce the quantity of low charge state ions produced at lower intensities that often represent unwanted background in such studies. Secondly, in conjunction with a tight laser focus, an ultrathin molecular beam yields an extremely small laser-molecule interaction volume that facilitates experiments on single gas-phase molecules. Using a laser pulse with 800 nm wavelengths, interaction volumes of about 100 μm^3 can be achieved while by introducing a slit, the interaction volumes can be reduced to about 5 to10 μm^3.
Figure 3-5 shows an image of the adjustable piezoelectric slit which has μm adjustment using piezoelectric activator. This slit is mounted by four spacers to the bulkhead separating between intermediate and the interaction chamber. The distance between the slit and the focal point is determined by the length of these spacers.

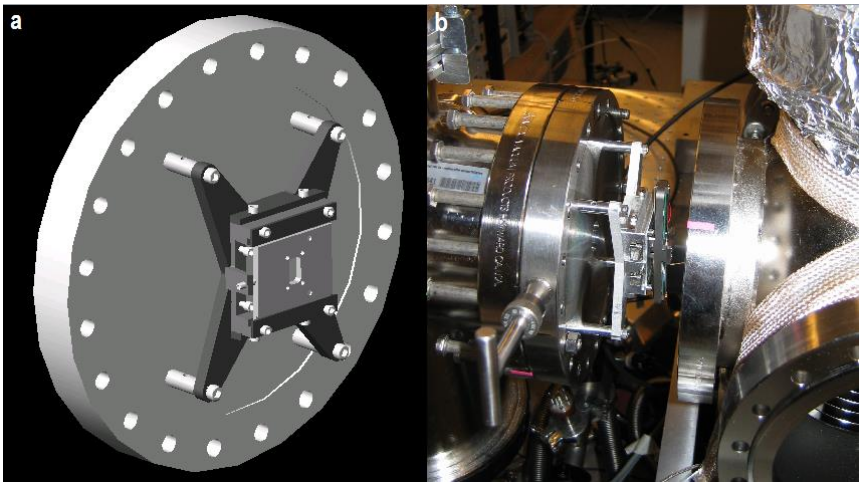

Figure 3-5 An image of the adjustable piezoelectric slit which has µm adjustment using piezoelectric activator.

As can be seen in Figure 3-1(m) after the laser beam enters the interaction chamber perpendicular to the molecular target gas jet, a 10 cm spherical mirror is responsible for focusing the laser beam and reflecting it back to the focal point. This mirror is connected to a 3D XYZ stage with micron resolution to locate the focal point right at the center of the supersonic gas jet. Resultant ions from interaction of the laser and the gas jet become accelerated in the direction of the detector at the lower part of the spectrometer.

3.2.6 Time of Flight Spectrometer (TOF)

The interaction between the laser pulse and the molecules in the focal point causes ionization of the molecule. As a result, strong Coulomb forces between ions create a repulsion and production of fragment ions. In order to record the momentum imparted to the fragment ions, these fragment ions need to be detected with a position sensitive detector. Guidance of the desired fragments toward the detector is facilitated using the TOF spectrometer technique. This technique is based on the separation of the resultant fragments according to their ratio of m/q. Figure 3-6 represents a 3D schematic view of a common TOF spectrometer. As can be seen in the figure this system includes a set of ring-shaped electrodes which are linked in series by resistors and are isolated providing a uniform electric field which causes a constant voltage gradient along the TOF axis. This constant voltage gradient provides a DC electric field which accelerates the fragments toward the detector. A grid (tungsten 99% transparent) at the end of the TOF region isolates it from the influence of the front of the microchannel plates which are held at a constant voltage.

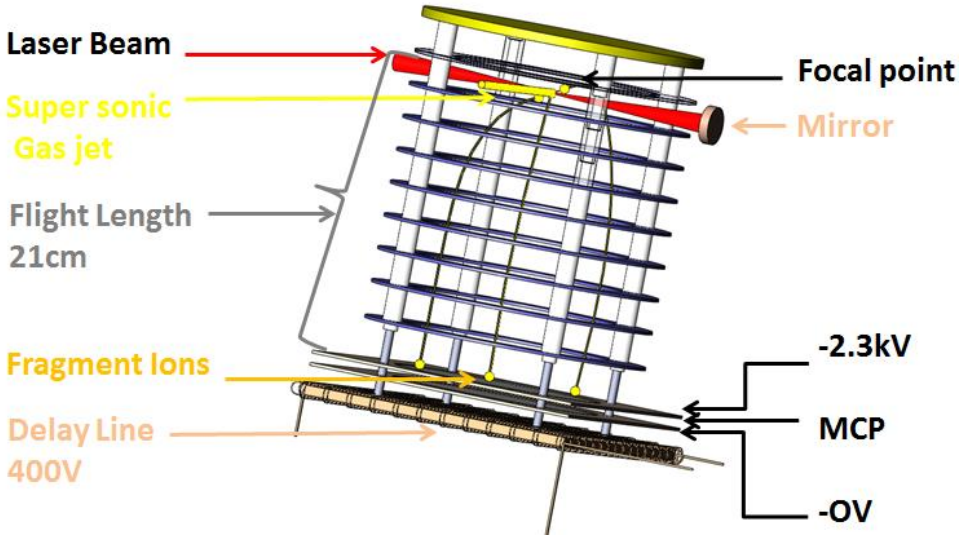

Figure 3-6: 3D schematic of a TOF spectrometer, MCP and delay line

The adjustable voltage is supplied by external supplies, usually between 2000V and 5000V in order to maximize the detection efficiency and also timing resolution of TOF.

The electric field is capable of collecting the ions in solid angle of 4π. The voltage applied across the spectrometer must be high enough to lead all possible energy levels of fragment ions to the detector over the flight range of 21 cm. As a result, the strong electric field generated within the flight tube separates and accelerates positively charged fragments as they fly towards the detector. The arrival time is recorded during movement of a typical fragment ion from the original explosion point to the detector, which precisely is defined as TOF. The TOF spectrometer main axis is perpendicular to the both laser and the gas jet axes. Figure 3-7 shows an image taken from the TOF apparatus used in the ALLS facilities.

Figure 3-7 A photograph of a real TOF spectrometer being used at ALLS laser facility

3.2.6.1 Time of Flight (TOF) Equation

The classical motion equation in a vector form for a typical fragment ion mass m, charge q, and velocity vector υ_0 under the extraction DC field E is described as follow:

$$m.\vec{a} = \vec{F} = q\vec{E} \tag{3.3}$$

Here $\vec{a}$ is the acceleration and $\vec{F}$ is the electric force on fragment ion.

The electric field $\vec{E}$ is in the TOF axis direction, thus for x and y direction electric $\vec{E}$ field becomes zero and equation (3.3) will simplified to only one direction along the TOF axis (z direction),

$$m.a_z = qE \tag{3.4}$$

Expanding this equation results in:

$$v(t)_z - v_{0z} = \int_0^t \frac{q}{m} E dt = \frac{q}{m} Et \tag{3.5}$$

where v_{0z} is the initial component of velocity of the ion in the Z direction. Rearranging and integrating gives

$$D = \frac{q}{2m} Et^2 + v_{0z}t \tag{3.6}$$

where D is the displacement of the ion during its flight time, which is assumed to be the same for all ions produced in the micron scale laser focus. Solving for t gives

$$t = \frac{m}{qE}(-v_{0z} + \sqrt{v_{0z}^2 + \frac{2qE}{m}D}) \quad (3.7)$$

According to this equation, using measured flight time t one can calculate the initial velocity component of the ion in the Z direction immediately after ionization. Knowing initial velocity is critical to calculate the KER and the momentum vector of each fragment (see next section). Referring to equation (3.7) for ions with zero initial velocity ($v_{0z} = 0$) an expression of the form $\sqrt{m/q}$ is used to obtain a mass to charge ratio plot to recognize each peak in the spectrum.

The zero flight times of the fragment ions t_0 can be determined using equation (3.7)

$$t = t_0 = \sqrt{2mD/qE} \quad (3.8)$$

3.2.6.2 Time of Flight Calibration

Unlike traditional mass spectroscopy, in the case where, the laser E field is parallel to the TOF axis, ions arrive earlier (forwards) and later (backwards) with respect to zero flight time t_0 (flight time for fragment ions with zero initial velocity) due to the explosion momentum imparted in the direction of the TOF axis. Thus, it is not trivial to differentiate the peaks obtained in TOF spectra and attribute them to specific fragment ions. Therefore, we need to calibrate the TOF spectra.

Ion identification can be made, as the strength of the uniform electric field *E*, the distance traveled by the ions *D*, and sqrt (*m/q*).

To an excellent approximation, D can be taken to be the flight time separation between the laser focus and the top electrode on the MCP which is 21cm.

In order to find the characteristic t_0 for each ion it is important to take into account t' the delay between the triggering of timing electronics and the passage of the optical ionization pulse through the laser focus. For the ith ion t_{i0} the flight time is given by

$$t_{i0} = t_i - t' \quad (3.9)$$

Furthermore by simplifying (3.8) and (3.9) equation (3.10) is resulted

$$m_i/q_i = B(t_i - t')^2 \quad (3.10)$$

where t_i is the apparent arrival time recorded by the TDC, t' and B is a scale factor. Both t' and B can be treated as calibration constants which can be calculated by considering two known ion peaks in the TOF spectrum which have times t_1 and t_2 by rearranging (3.10)

$$t' = \left(t_2\sqrt{m_1q_2/m_2q_1)} - t_1\right) \Big/ \left(\sqrt{m_1q_2/m_2q_1)} - 1\right) \tag{3.11}$$

B can be defined by equation (3.12):

$$B = \left(\left(\sqrt{m_1/q_1)} - \sqrt{m_2/q_2)}\right)/(t_1 - t_2)\right)^2 \tag{3-12}$$

The time interval for these two peaks should be as long as possible in order to maintain accuracy, and must be ions with initial velocity zero (parent ions). For example, in the case of CO_2 we use H_2O^+ and H_2^+ peaks. This process is the basis of the TOF calibration, which is the essential first step when analyzing data obtained using the ALLS instrument.

To confirm or invalidate the hypothetical peak assignment the mass-to-charge ratio of all peaks must be inspected. That includes the ratios of other parent ions such as background gas and fragment ions. Typical TOF spectra for the triatomic molecules CO_2 and N_2O are depicted in Figure 3-8 and 3-9. In Figure 3-8 the E field axis is perpendicular to TOF axis while in Figure 3-9 the E field is parallel to TOF axis.

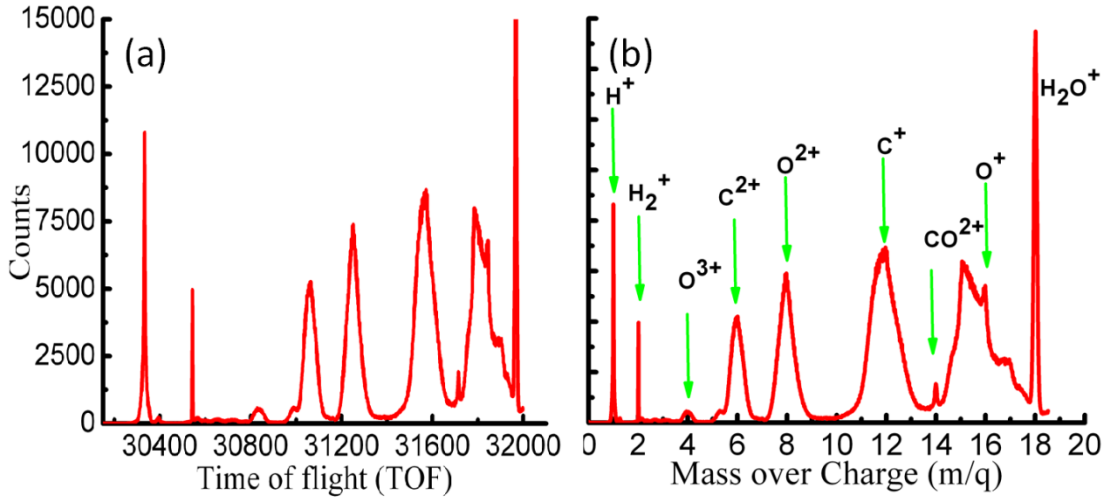

Figure 3-8: TOF mass spectrum of a symmetric triatomic molecule CO_2, here green arrows show TOF and sqrt (m/q) for fragment ions with zero initial velocity. Here the E field polarization is perpendicular to the TOF axis

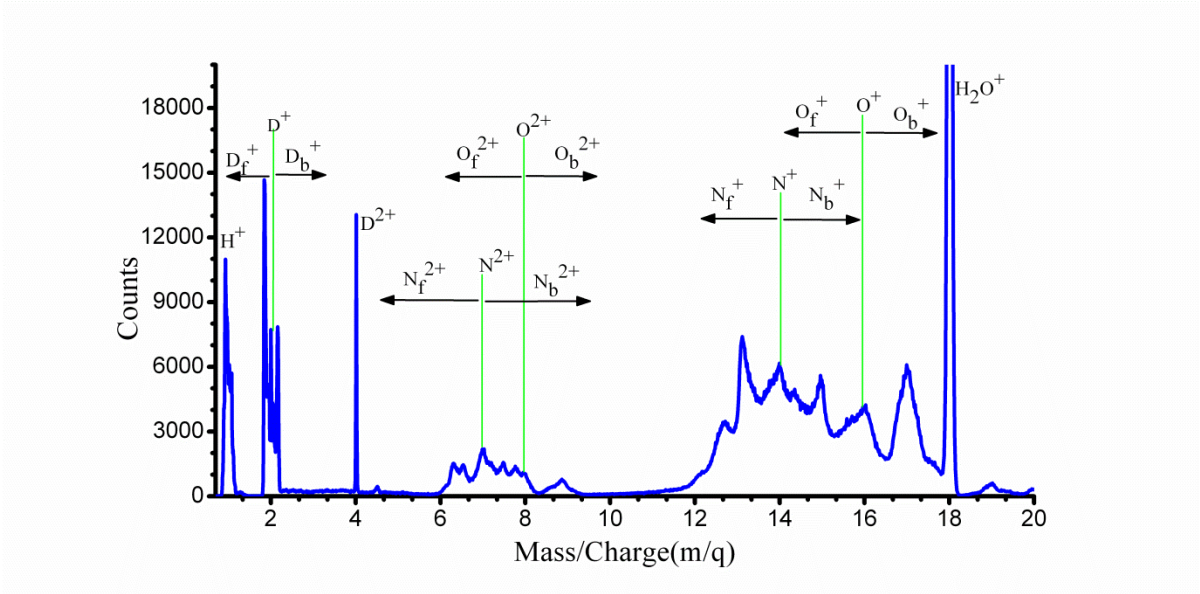

Figure 3-9 TOF mass spectrum of asymmetric triatomic molecule N_2O, arrows shows region related to backward and forward ions. Green vertical lines show m/q for fragment ions with zero initial velocity; here the E field polarization is aligned to the TOF axis

As explained earlier an inherent drawback is that, the TOF of different events with different charge states can overlap, as Figure 3-10 shows in the case of the OCS molecule. In the case of the (1, 1, 1) channel for example the TOF peak related to oxygen forward O_f^+ is overlapped with zero TOF and backward sulfur ion S_b^+ TOF [79].

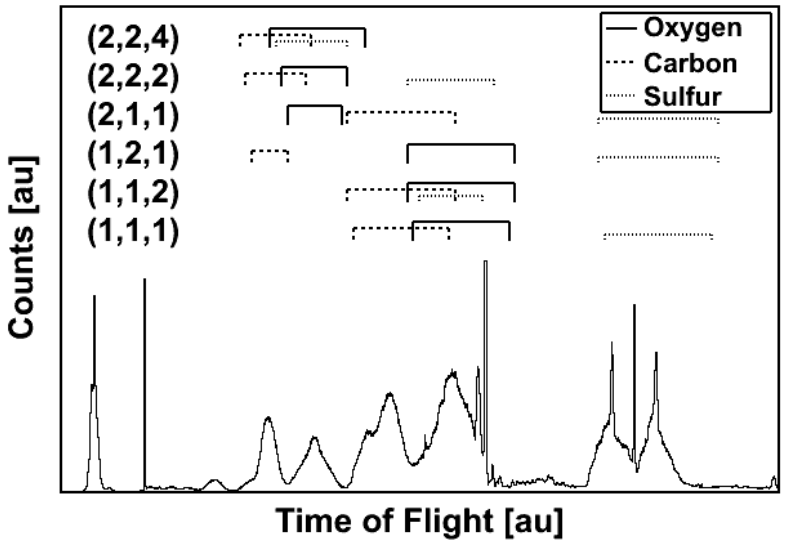

Figure 3-10 OCS TOF and fragment ion TOF Windows for a selection of channels (Reprinted with permission from [79])

3.3 Position of the fragment ions N_t^+, N_m^+, and O^+ on the detector in vertical and horizontal polarization

Figure 3-11 presents a typical detector image showing the relative position of fragment ions N_t^+, N_m^+, and O^+ from the N_2O (t and m refer to the terminal and middle N ions) molecule on the MCP while the polarization of the laser pulse is vertical (Figure 3-11 (a)-c) (The E field of the laser is parallel to the TOF axis). In this figure the vertical axis represents the Y coordinate, the horizontal axis represents the X coordinate and the color demonstrates the frequency of ions with a particular (X, Y). Variation of the color from blue to red indicates an increase in magnitude. As can be seen in this figure all three fragment ions N_t^+, N_m^+, and O^+ hit to the center of the detector. Because break up processes is in the TOF axis.

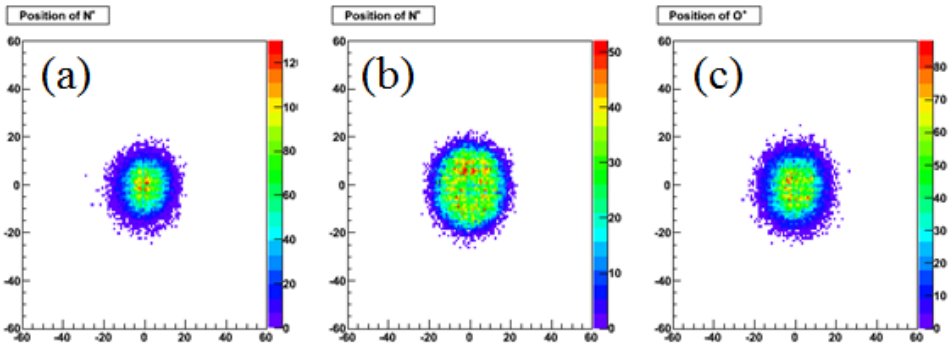

Figure 3-11 Position of the fragment ions on the detector (MCP) in a vertically polarized electric field of the laser in respect to TOF axis (polarization of the laser parallel with TOF axis), (1, 1, 1) channel 200fs-H. (a) N_t^+, (b) N_m^+, and (c) O^+.

Similarly, Figure 3-12 presents a typical detector image or position for N_t^+, N_m^+, and O^{2+} fragment ions of the N_2O molecule on the MCP while the polarization of the laser pulse is horizontal (the electric field of the laser pulse is perpendicular to the TOF axis). As can be seen in Figure 3-12 (b) the N_m^+ hit to the center of the MCP and this confirms that during the break up the middle nitrogen ion does not get much momentum that is the N_m^+ fragmented with zero initial velocity. In Figures 3-12 (a) and 3-12 (c) there are separate islands and this is because N_t^+ and O^+ have initial velocity perpendicular to TOF axis. As a result, depending on the molecular axis orientation each fragment has chance hit to different part of the MCP.

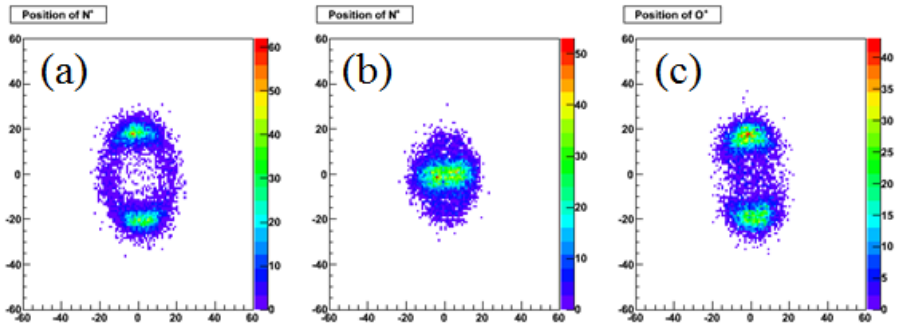

Figure 3-12 Position of the fragment ions on the detector (MCP) in a horizontally polarized electric field of the laser pulse in respect to the TOF axis (polarization of the laser pulse perpendicular to TOF axis), channel (111-200fs-V) (a) N_t^+, (b) N_m^+, and (c) O^+.

3.3.1 Position sensitive detector (PSD)

Using a PSD allows us to obtain information on momentum sharing among fragments. We need to measure the initial velocity vectors of each fragment ions V_{0x}, V_{0y} as well as V_{0z}. As Figure 3-13 shows this system consist of a doublet MCP and square type two dimension delay line anode detector (DLD) (RoentDek Handels GmbH) [80]. These components give us the ability to measure fragment ions' position in the xy plane and their flight time associated with the z axis. All of this information ultimately determines the velocity vectors of each fragment ion (next section). The ALLS setup has two of these detectors mounted on each end of spectrometer. Electrons are detected by a PSD at the top and positive ions are detected by a PSD below the interaction point. In this study only data obtained from the fragment ion detection is used.

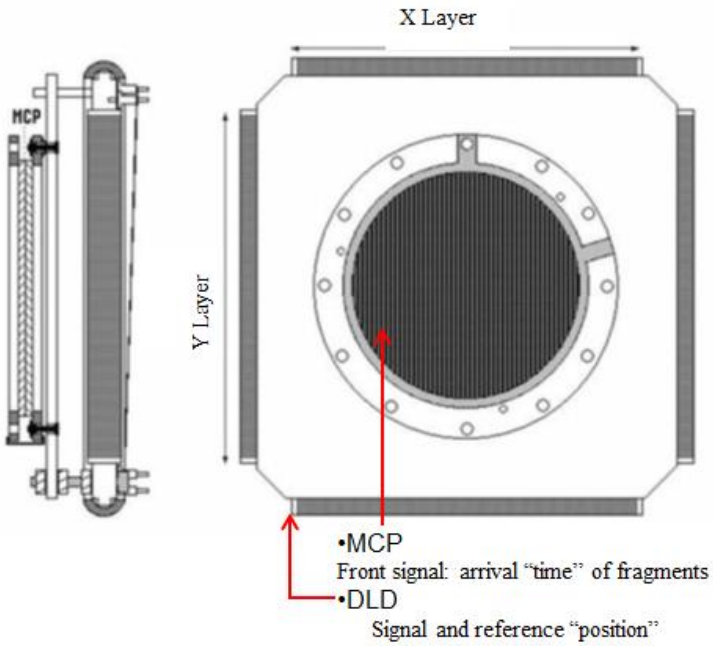

Figure 3-13 Schematic front and view of a delay line system integrated to a MCP (Reprinted by permission from [80])

3.3.2 Micro Channel Plate (MCP)

The MCP is mounted in front of two flattened helical delay lines (Figure 3-13 and 3-14). The detector is placed a few millimeters above the grid of the time-of-flight mass spectrometer on a stainless steel mounting plate. The mounting plate is joined to the spectrometer's top electrode by four steel rods and is electrically isolated by a set of alumina sleeves and spacers. A steel spring at the top of each rod prevents spacer breakage during chamber bake-out.

One power supply channel is used exclusively for biasing the micro channel plate. One of the MCP plates is negatively biased with 2.3 kV and the other plate is grounded (Figure 3-6). Since the spectrometer's top electrode is typically grounded as well, ions leaving the spectrometer experience a slight acceleration before collision to the detector. The second power supply channel is connected to a network of potentiometers providing typically 400V, used independently to bias the delay lines as well as their aluminum back plate independently. Each fragment ion reaching to one of the MCP channels produces a cluster of electrons which intensify the charge of the influencing fragment ion. This signal from the MCP front gives the flight time of fragment ions and the cluster of electrons leaving the MCP back are amplified by the second plate to the level that can be detected by the DLD to give the position

of the fragment ions on the MCP plate. All of his information is ultimately determining the three-dimensional vector velocity.

Figure 3-14 is the photograph of the PSD ion detector assembly used at ALLS for data acquisition.

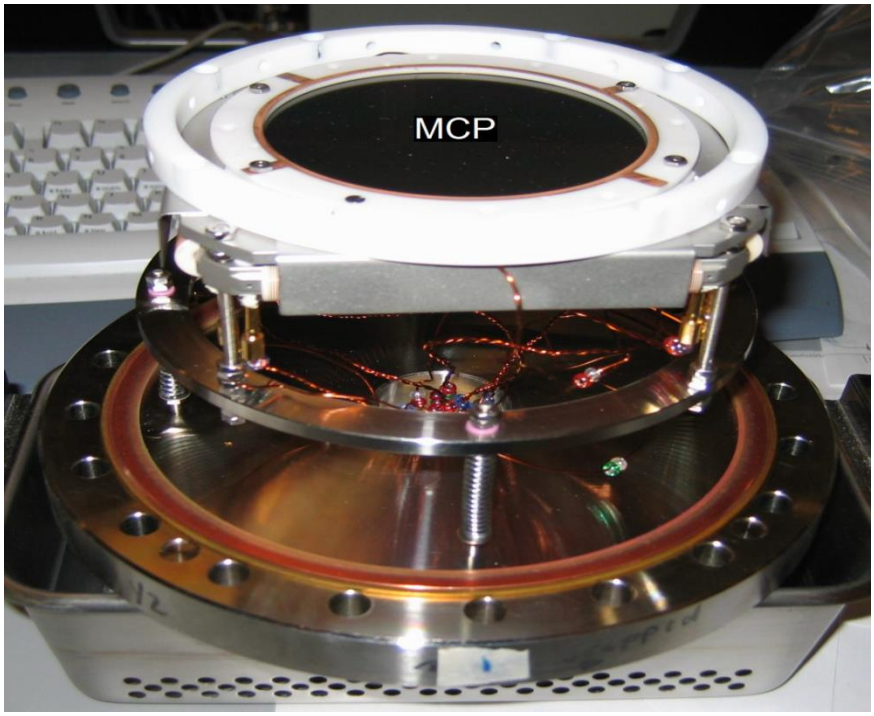

Figure 3-14 MCP image being used in ALLS laser facility

3.3.2.1 Delay line

The delay lines consist of two pairs of thin filaments coiled around a ceramic frame in X and Y directions. One filament which is referred to as the signal wire is supplied with a positive voltage. The other filament is referred to as the reference wire and is supplied by a voltage lower than the signal wire. In this system, electron pulses from the MCP are received by the signal wire. Also, the two filaments are closely adjacent and so experience the same electric noise. The electric noise can be eliminated by subtracting the signals acquired from both filaments in the differential amplifier. The time to digital converter (TDC) is able to detect multi-hits with dead time of less than 10 ns for a pulse pair.

Figure 3-15 shows the schematic view of how to extract 2D positions (X, Y) from the delay-line signals according to the time delay.

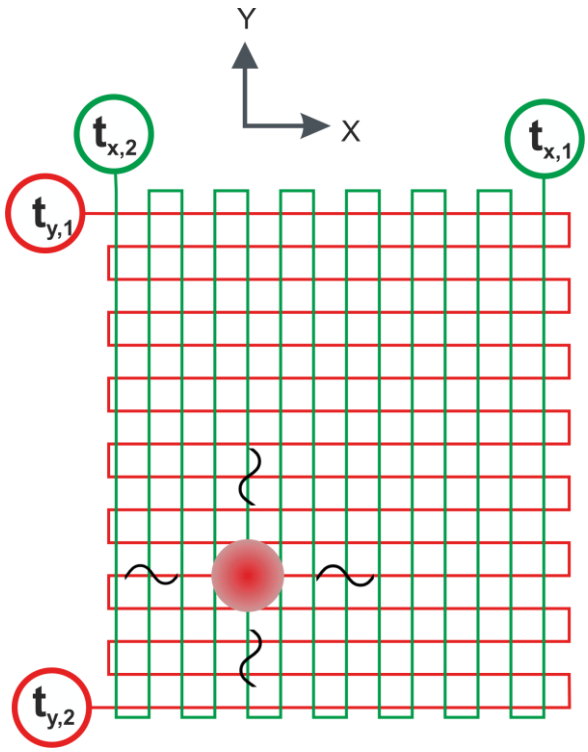

Figure 3-15 Schematic view of a mechanism of action in a delay line (Reprinted by permission from [80])

The wires absorb the electron cluster formed by the MCP (red disk) which causes generation of a charge moving along the X and Y directions. The time interval in which the signal travels the total length of wire determines the coordinate of the collision. Channels of a TDC are utilized to measure the arrival times of the signals leaving two sides of a wire.

X and Y are determined by:

$$X = C(t_{1x} - t_{2x}) \quad (3.13\ a)$$

$$Y = C(t_{1y} - t_{2y}) \quad (3.13\ b)$$

Where t_{1x}, t_{2x}, t_{1y}, t_{2y} are the arrival times of the signals on the right and left of X axis and top and bottom ends of Y axis, respectively. In this equation C is the conversion factor of time/position determined by the detector calibration [80] [81] .

3.3.3 Data Acquisition and electronics

To measure the multi-hit fast signals coming from the PSDs with higher resolution, both MCP and DLD signals for each fragment have to be analyzed appropriately. Thus, a sophisticated set of electronics is required to do so. In this section we aim to elaborate the electronic system for data acquisition and analysis in more detail.

We use commercial electronics (RoentDek GmbH) which consists of a preamplifier, a constant fraction discriminator (CFD) and a TDC. The action of these electronics starts with a logic pulse from the Ti: Sapphire amplifier which serves as a trigger signal for TDC. In detail, all the raw signals from the delay lines of the PSD act as an input signal for the CFD after amplification (200 times for DLD signal and 20 times for MCP signal). The output from the CFD is in a standard negative logic signal with width about 10ns. CFD output signal is measured by a TDC. This type of TDC includes 32 independent signal channels which are able to record up to 16 hits. The timing resolution is 0.5 ns and time range is 8 to 32 μs per trigger. Succinctly, position and TOF resolution and TOF range is defined in the TDC. The weak point of TDC, i.e. dead time 10ns, is that position data is inaccurate as only one of the fragment ions can be detected if the time interval between them is less than 10 ns [80].

3.3.4 Data analysis

Online data acquisition and analysis is facilitated by C^{++} software developed at ALLS, and a data analysis framework which has been developed at Waterloo [79], using Root software (Version 5.28) established by CERN (also in C^{++}) [82]. The output file from the ALLS software is an lmf file format which is a block of data consisting of many discharges of the TDC, i.e. the data on all collisions saved in a 32 μs interval succeeding an order of laser pulses. The lmf file contains the position (x, y) and time t of all fragments ions striking the detector. Spectrometer field and masses and charges of the fragments were used to calculate three dimensional momentum vectors in Root as will be explain later in this section. For purposes of analysis results, the software also contains algorithms for the calculation of various physical quantities. It will be possible for example to calculate the distribution of momentum or kinetic energy either for each fragment or for several ions in coincidence, TOF and sqrt (m/q) Plots, Coincidence Map, Molecular Counts, Newton Plots, Newton normalized plot, Dalitz Plots, Angle Θ, χ and $\Theta - \chi$ plots, and so on.

3.3.4.1 Velocity Components Determination

In this analysis the first step is to calculate the momentum of each fragment ions. Using flight time and position (x, y) information, the asymptotic momentum vector for each fragment can be determined through simple kinematic equations of motion:

$$P_x = \frac{m(x - x_0)}{t} \tag{3.14a}$$

$$P_y = \frac{m(y - y_0)}{t} \tag{3.14b}$$

$$P_z = \frac{qE}{2}\left(\frac{t_0^2 - t^2}{t}\right) \tag{3.14c}$$

here, x_0,y_0, are the location at which an ion will arrive if zero momentum is imparted during ionization and t_0 is the zero time of flight respectively. E, q, and m are the electric field, particle charge, and it's mass, respectively.

To determine which ions detected in coincidence, originate from the same molecule, we can use conservation of momentum as follows:

$$P_1 + P_2 + P_3 = 0 \tag{3.15}$$

In this equation P_1, P_2, P_3, are the momenta of each fragment ion from one molecule. The vector resulting from the sum of these quantities will be zero if the ions result from the same parent ion. It is possible to filter our data which come from one molecule keep the events obtaining only in coincidence where $\sum \vec{P} = 0$. It is only possible to correlate the channels for which all fragments are charged, due to the nature of the spectrometer.

3.4 Degeneracies

Mass to charge ratio degeneracy for some common molecules causes difficulty in identifying specific ions during a detection event. For instance, there are two types of nitrogen atom in the triatomic molecule of N_2O: the central one and terminal one. As fragment ions have the same TOF window, their TOF and consequently their mass to charge ratio peaks overlap. B. Wales has developed more the algorithm for data analysis to tackle this problem [79] [83]. Refer to equation (3.15) the algorithm identifies all ions and checks whether their net momentum is close to zero. For example, identifying the terminal oxygen species of CO_2 leads to a redundant result due to the symmetry of the molecule. Thus, by defining the forward and backward TOF cuts window for oxygen one could separate the ion identities. This is not the case for N_2O. As two nitrogen species are not symmetric in the molecule,

totally overlapped TOF windows will occur. If such TOF windows are used in the analysis than algorithm, the central and terminal ions cannot be reliably identified any mistaken for one and other. To address this issue, the algorithm firstly assigns degenerate flags to ions if two identities of the same mass and charge are registered for a single event. Then, if two possible molecules are generated using two degenerate ion identities, only the first one is considered.

Figure 3-16 shows the TOF of the (1, 1, 2) channel of N_2O for N_t^+, N_m^+, and O^+ fragment ions. The blue distribution curve is assigned for O^{2+} and the green and red ones are for the N^+ ions. In this diagram, the full range of the TOF distribution is used for the central nitrogen ion as well as for the terminal one. Accordingly, the black curve shows the overlapped TOF window for the central and terminal ions. Alternatively, in the Figure 3-17, a narrower window is chosen for the central ion and a broader range is chosen for the terminal ion. The terminal ion is expected to hit the detector far from the zero time of flight; but the central ion arrives close to zero TOF. As a result, this technique gives two clearly separated TOF distributions, one for the central ion (green), and the other for the terminal one (red). Since this technique assumes a strict TOF window for each ion, events arriving outside the ranges (central nitrogen arriving in the terminal range and vice versa) will pass the coincidence test without undetectable false ion identification. A zero count zone is observed between the peak regions for the central and terminal ions in Figure 3-16 and Figure 3-17, indicating that very few central ions are passing through the central TOF window into the terminal TOF window and vice versa.

In the case of (1, 1, 1) channel this degeneracy problem become more complicated. Because in addition of overlapping for terminal and central nitrogen, TOF window of the O^+ will overlap with the TOF window of central nitrogen and this is explained in detail in chapter 5.

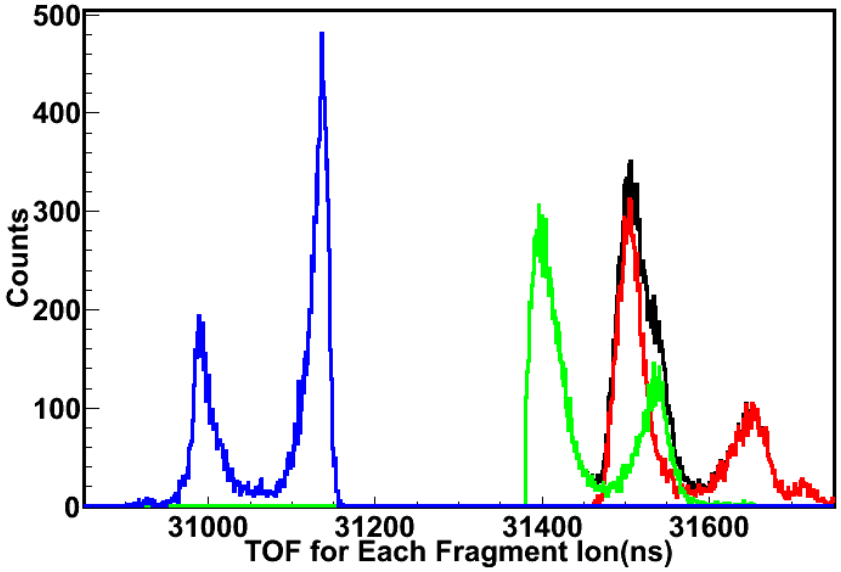

Figure 3-16 TOF distribution for O^{2+} (blue) and N^{+} ions (green and red) where the same TOF window is defined for the central and terminal N^{+} ions.

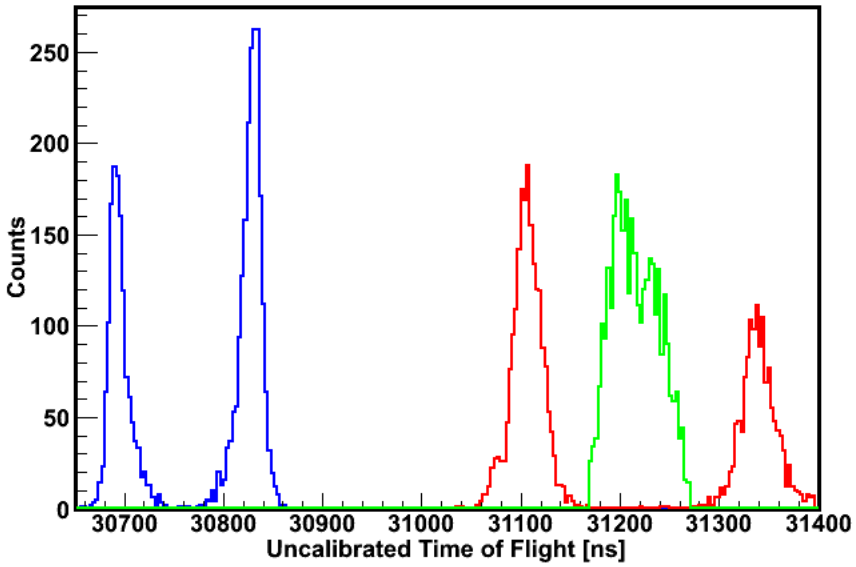

Figure 3-17 TOF distribution for O^{2+} (blue) and N^{+} ions (green and red) where a narrow TOF window (green) is used for the central N^{+} ion and a wide TOF window (red) is used for the terminal N^{+} ion.

3.5 Momentum selection in data analysis

The recorded data includes the position and time information of all fragment ions. We are interested in finding ions which come from the same molecule, the net momentum of the molecules before and after the explosion is constant for a true coincidence. Therefore, conservation of momentum can be used to identify true coincidences. We define threshold momentum in order to identify the true coincidences for each dimension X (Supersonic jet gas direction), Y (propagation of the laser pulse direction), and Z (polarization of the field and the TOF axis).

During the analysis of a CEI dataset, the coincidence algorithm produces several possible molecules per laser shot. To adjust the calibration parameters and ensure the momentum selection is accurately applied to identify true coincidence, five histograms are used as diagnostics: The momentum sum of the coincident fragment ions from a possible molecule 1) z, 2) x, and 3) the y direction, are reordered in addition 4) the magnitude of the vector momentum sum, and 5) KER are also recorded.

Figure 3-18 shows these 5 diagnostic histograms for (1, 1, 2) channel of N_2O. Firstly, the algorithm generates and populates the momenta of all possible molecules for a specific channel for example the (1, 1, 2) channel (first row in histograms). Next, the algorithm takes into account the molecules that pass the momentum sum threshold in the z-direction (the second row histograms). The algorithm repeats the previous step for the molecules passing the momentum sum threshold in both z-direction and x-direction (histograms in the third row). Finally, the algorithm populates the momenta for the molecules passing momentum selection in all three directions (the histograms in the last row).

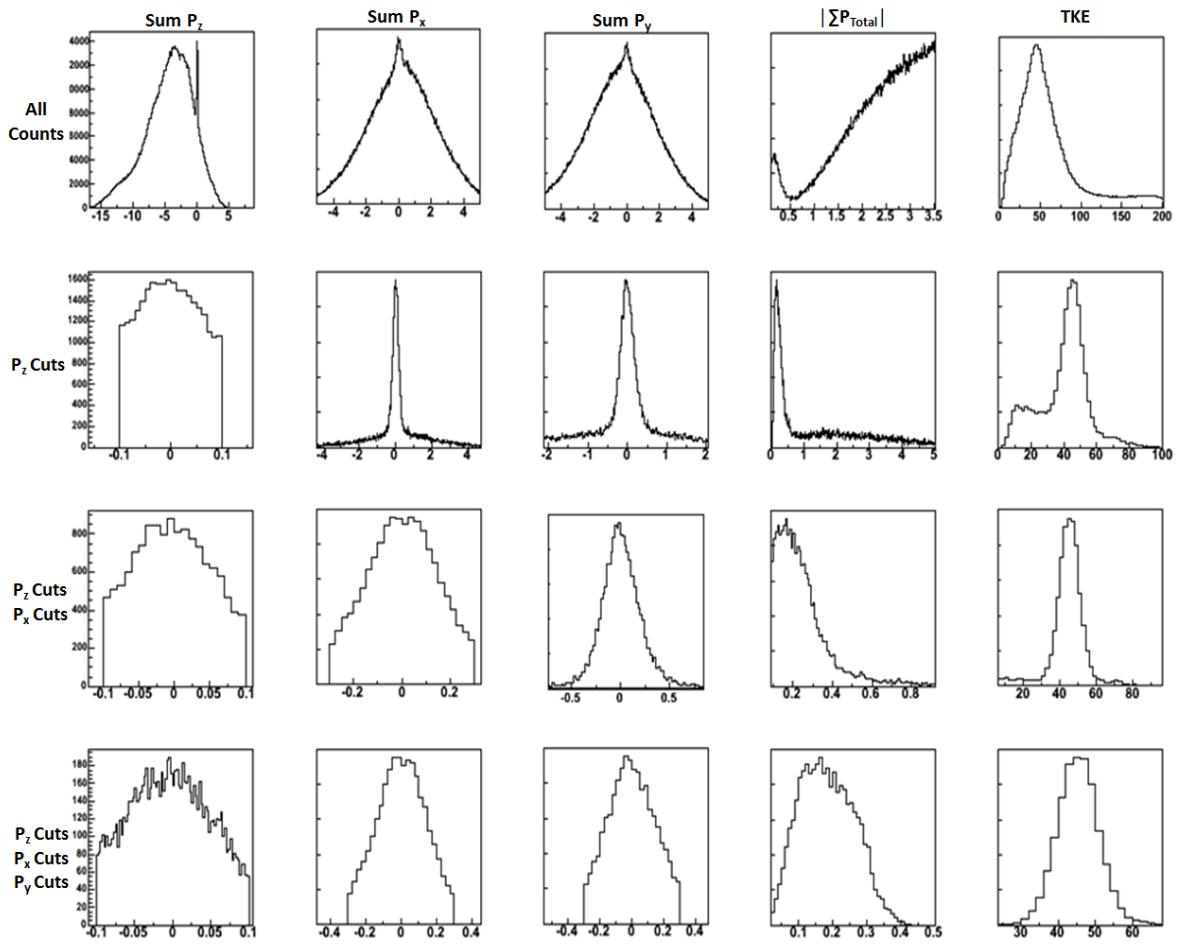

Figure 3-17 Momentum judgment diagnostic of N_2O analysis, left to right: Z momentum sum; X momentum sum; Y momentum sum; magnitude of momentum sum; KER, Top to bottom: all hypothetical molecules; Z selection; Z and X selection; Z, X, and Y selection, momentum units of [0.5×10^{-22}kg m/s]

Before any restrictions have been placed on the data, there is a distinct peak in all three histograms representing the X, Y and Z momentum in columns 1, 2 and 3 top plots this indicates that some true coincidences have been recorded. The large background shows false coincidences which can be eliminated by successively restricting the range of momentum which events are allowed to have. Also a narrow peak near zero in the total momentum sum (column 4 top plot) confirms that the algorithm has identified true coincidences. To ensure that the proper calibration is achieved, the X, Y and Z histograms are monitored (Column 1, 2, and 3). Additionally, a rising edge in the momentum sum

plot results from false coincidences and continues to grow well beyond the threshold value of $.5 \times 10^{-22}$kg m/s. Thus, it is difficult to choose an appropriate threshold for the momentum sum from this plot and it would be difficult to estimate the true to false coincidences ratio [83] .

Instead we restrict the momentum in the Z, X and then Y momentum successively in rows 2, 3, and 4. As can be seen in row 2 the effect of cutting the Z momentum at some appropriate level also dramatically effects the histograms for X, Y and the total momentum sum, accentuating the narrow peaks indicating the true coincidences.

In this study thresholds of momentum sum values around 0.5×10^{-22} Kg m/s, where used to eliminate false coincidences but ensure that true coincidences were correctly recorded.

Chapter 4

CO_2 ionization and dissociation dynamics in intense femtosecond laser radiation, probed by systematic pulse length variation from 7 to 200 fs

This chapter which is adapted from the Physical Review Letters paper [26] describes a set of experiments carried out on CO_2. The primary purpose of the experiments is to help us understand the process of CREI for a polyatomic molecule, in order to do this we explore the pulse length dependence of molecular geometry and kinetic energy release during Coulomb explosion. This chapter includes the first quantitative comparison between experiment and theory for a triatomic molecule. The work highlights the importance of the 3+ state for CREI. This work was a collaborative effort of all the authors of [17]. My involvement in this work consisted of participation in the setup of the laser experiments, data acquisition, data analysis, and graphical representation and finally manuscript preparation.

4.1 Introduction

Ultrafast molecular imaging techniques with intense infrared femtosecond laser pulses are based on converting long wavelength photons into short wavelength particles via the process of ionization: XUV (extreme ultraviolet) photons for orbital tomography [84] electrons for laser induced electron self-diffraction[85], [86], and ions for time-resolved Coulomb Explosion Imaging (CEI) [74], [87], [88]. It is therefore critical to understand the different mechanisms behind high intensity molecular ionization. One of the mechanisms is CREI.

The process by which a molecule in an intense femtosecond laser field ionizes more efficiently as its bond length increases towards a critical distance R_c is known as charge resonance enhanced ionization (CREI). For the first time we make a series of measurements of this process for a polyatomic molecule, CO_2, by varying pulse duration, from 7fs to 200fs in order to identify, the charge states and timescale involved. We reconstruct the geometry at the moment of explosion and obtained the critical geometry ($<R_{CO}> \approx 2.1$ Å and $<\theta_{OCO}> \approx 163^o$, compared to equilibrium values of $<R_{CO}> \approx 1.16$ Å and $<\theta_{OCO}> \approx 172^o$). All necessary calculation and the algorithm related to this molecular geometry reconstruction from our momentum triple coincidence data were performed by our collaborator J. P. Brichta (University of Waterloo, Canada). Finally, to investigate the details of CREI and identify

physics behind this phenomenon, we provide the result of the calculation by our collaborators from Prof. Andre Bandrauk's group (Universite de Sherbrooke). They make the first quantum numerical simulations of ionization rate for a polyatomic molecule in an intense field (the quantum ab initio calculations of ionization rate and low-lying 1D Born-Oppenheimer potentials for the carbon dioxide trication) and identify the electronic states ($3\sigma_u$ and $5\sigma_g$) responsible for CREI in our experimental observations of CO_2.

4.2 Previous work

In the case of CEI, experiments with diatomics have shown that the molecular bond stretches towards a critical internuclear distance (R_C) where the ionization rate is greatly enhanced [44] [89]. This also explains the explosion of clusters creating highly charged states [90]. This process called CREI is well understood for diatomic molecules, such as H_2^+/D_2^+, in terms of charge resonance (CR) states (σ_g and σ_u) that are strongly coupled by the laser field at large internuclear distance [49], [50], [91]. At such distances, the energy difference between the two CR states approaches the photon energy, giving rise to electron localization by creating a coherent superposition of opposite parity states [92] followed by enhanced ionization. For triatomic molecules, the experimental appearance of a critical geometry has not been elucidated in terms of CREI and its mechanism remains a matter of interest. CO_2 has been the subject of experiments using both uncorrelated and correlated fragment detection techniques [56], [70], [93]. All those studies used pulses of 50 fs and longer and have attempted to understand the mechanism of dissociative ionization. Two consistent parts of the picture which have emerged are that the bond lengths determined from a Coulombic inversion appear to be stretched between 2 and 2.5 times the equilibrium distance to a critical distance (R_C) and the bond angle is less than 180 degrees. Experimental results for CO_2 have been compared to classical calculations [56], [70] adapted from the over the barrier model developed by Posthumus et *al.* [19]. This simple approach predicts a value for R_C but for bonds stretched considerably more than indicated by experimental observations. Numerical simulations of nuclear motion on field dressed molecular potentials of CO_2^{2+} have revealed bending and symmetric stretching on a time scale of ~100 fs [25]. These vibrational dynamics cannot explain the observation of a R_C when CO_2 is ionized to high charge states (> 3+). To our knowledge, no experimental work has successfully tracked the dynamics on either the doubly or higher charged states and no theoretical work has modeled the mechanism for CREI in triatomic molecules including CO_2.

It has been demonstrated for diatomic that by using few-cycle pulses, CREI can be suppressed since the molecular ion does not have sufficient time to reach R_C within the duration of the pulse [66]. Therefore, varying the pulse duration from the few-cycle to the multi-cycle regime is a valid approach to follow the appearance of CREI and investigate its molecular origin. In this chapter, we use 3D-ion-momentum coincidence measurements of the three-body dissociative ionization of CO_2 to CO_2^{n+} (n=3 to 6). This technique is used to measure the atomic fragment ions in triple coincidence: O^{k+}, C^{q+} and O^{l+} ions are identified as the result of the fragmentation of a single molecule only if their total momentum is close to zero ($< 5\times10^{-23}$ kg×m/s). We used a linearly polarized 800 nm laser pulses to make the first systematic study of the dependence of dissociative multiple ionization dynamics on laser pulse duration for any polyatomic molecule. We achieve this by varying the pulse duration from 7 fs up to 200 fs to find the onset of CREI. We then perform nonlinear non-perturbative time-dependent density functional theory (TDDFT) calculations to attempt to identify the CR states and thus the underlying mechanism for CREI in CO_2.

4.3 Experimental apparatus

The experiments were performed at the Advanced Laser Light Source using the multi-kHz Titanium-Sapphire (Ti- Sapphire) laser system (KMLabs). Few-cycle pulses (7 fs) are obtained using nonlinear propagation in a hollow core fiber filled with Ar and by dispersion compensation using chirped mirrors. To achieve longer pulse duration, the fiber was evacuated. Using an acousto-optic programmable dispersive filter located in the stretcher of the Ti- Sapphire amplifier, we applied second order dispersion ($\Phi^{(2)}(fs^2)$) to achieve the desired pulse duration. The laser pulses are focused by a parabolic mirror (f = 10 cm) on a well-collimated supersonic jet of CO_2 inside a uniform-electric-field ion imaging spectrometer. The fragments are detected and their full 3D momenta are determined using a time- and position-sensitive delay-line anode detector at the end of the spectrometer (RoentDek Handels GmbH).

4.4 Dissociation along the laser field polarization and TOF spectrum

For 7 fs, we observe that a much higher intensity is required to produce high charge states such as C^{2+} and O^{2+}. Figure 4-1 (a) compares the time-of-flight mass spectra from 7 fs I = 2×10^{15} W/cm^2 to 200 fs I = 2×10^{14} W/cm^2 giving similar ratios for C^{2+}/C^+ ion yields. This observation confirms that ionization of CO_2 to high charge states is much easier for multi-cycle pulses, i.e. CREI is suppressed with few-cycle pulses[66].

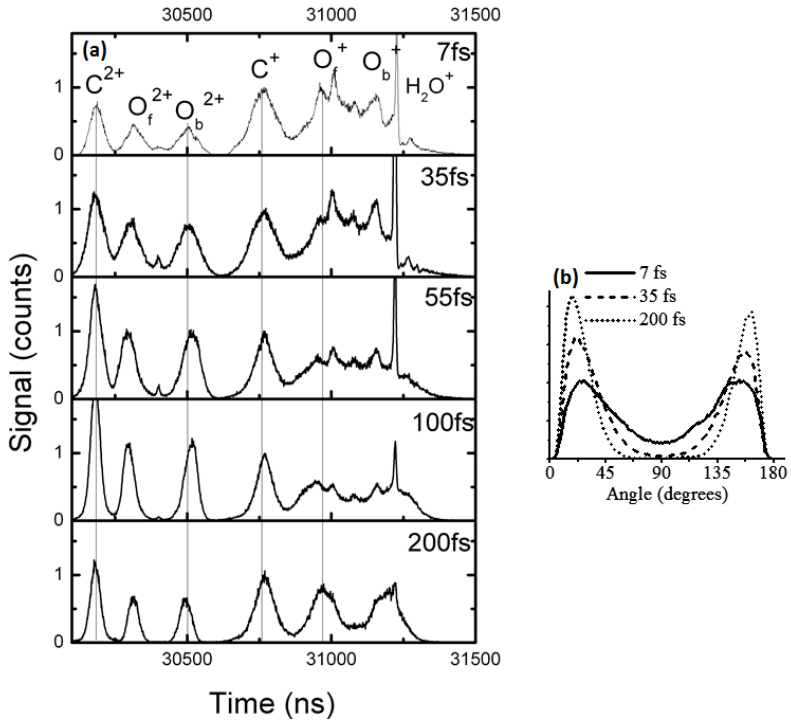

Figure 4-1 (a) Mass/q spectra obtained for two experimental conditions; 7 fs I = 2×10^{15} W/cm^2 and 35-200 fs I = 2×10^{14} W/cm^2. (b) Angular distribution of O^{2+} fragments relative to the laser polarization direction as a function of laser pulse duration; 7 fs I = 2×10^{15} W/cm^2, 35 fs I = 8×10^{14} W/cm^2, and 200 fs I = 2×10^{14} W/cm^2.

In addition, for 200 fs duration, the forward and backward O^{2+} peaks are quite narrow and the signal drops to zero between them, whereas for the 7 fs pulse the peaks are wide with continuous signal in between.

There are two contributing factors to this phenomenon. First, and most importantly CO_2 molecules can undergo fragmentation either along, or perpendicular to the laser polarization axis. For a long pulse, molecules are preferentially ionized when they are orientated along the laser polarization axis (which here is along the spectrometer time-of-flight axis). As a result the fragment ions O^{2+} have an initial velocity along the TOF axis direction, so that the signal drops to zero between the forward and backward O^{2+} peaks. In contrast, for 7 fs, some ions are produced with the molecular axis close to 90 degrees with respect to the polarization axis. Although perpendicular fragmentation of the molecule gives rise to zero initial velocity for the oxygen ions along the polarization/TOF axis, the fragment ions which arise from these molecules have finite velocity, but the result is signal in the TOF

spectrum near to the time associated with an O^{2+} ion without initial velocity and resulting in a continuous signal in between the forward and backward O^{2+} peaks. The second contribution leads to a small peak in some of the spectra between the O^{2+} forward and backward peaks, the reason for the presence of this signal is, the fragmentation of contaminant water molecules, which can lead to O^{2+} ions with low initial velocity parallel to the TOF axis. The oxygen in water holds the central position, thus the O^{2+} has a low kinetic energy release during Coulomb explosion. As can be seen in Figure 4-1 (a), the signal for parent ion of H_2O is more pronounced for the shorter pulse laser experiments and diminishes for longer pulse laser experiments (200fs). The signal from H_2O break up is completely eliminated as a contaminant when we use coincidence methods. Figure 4-1 (b) shows the angular distributions of O^{2+} plotted for 7 fs $I=2\times10^{15}$ W/cm^2, 35 fs $I=8\times10^{14}$ W/cm^2, 200 fs $I=2\times10^{14}$ W/cm^2. A dramatic drop in alignment such as the one observed for 7 fs has previously been reported for the Coulomb explosion of D_2 and is explained by the suppression of CREI [66] at such short pulse lengths.

4.5 KER and bend angle (φ) distributions for different channels

Herein, we investigate the dependence of both total kinetic energy released and bond length and bend angle of the fragmented ions. Note that the results obtained from triple coincidence measurements. Figure 4-2 shows the KER release and the bend angle φ of the molecule CO_2. For the (1, 1, 1) in Figure 4-2 (a) and (f), the (1, 1, 2) in Figure 4-2 (b) and (g), the (1, 2, 2) in Figure 4-2 (c) and (h), the (2, 1, 2), in Figure 4-2 (d) and (i), and the (2, 2, 2) in Figure 4-2 (e) and (j) channels KER and φ is measured as a function of pulse duration. As can be seen, a decrease in pulse duration results in an increase in total KER for all channels except (1, 1, 1) in which the total KER appears to be independent of the pulse duration. In addition, decrease in pulse duration results in increase in the angle φ between the momentum vectors of the end fragment ions which is the result of bending of the molecules. Both of these trends are most apparent for channel (2, 2, 2) (Figure 2 (e)).

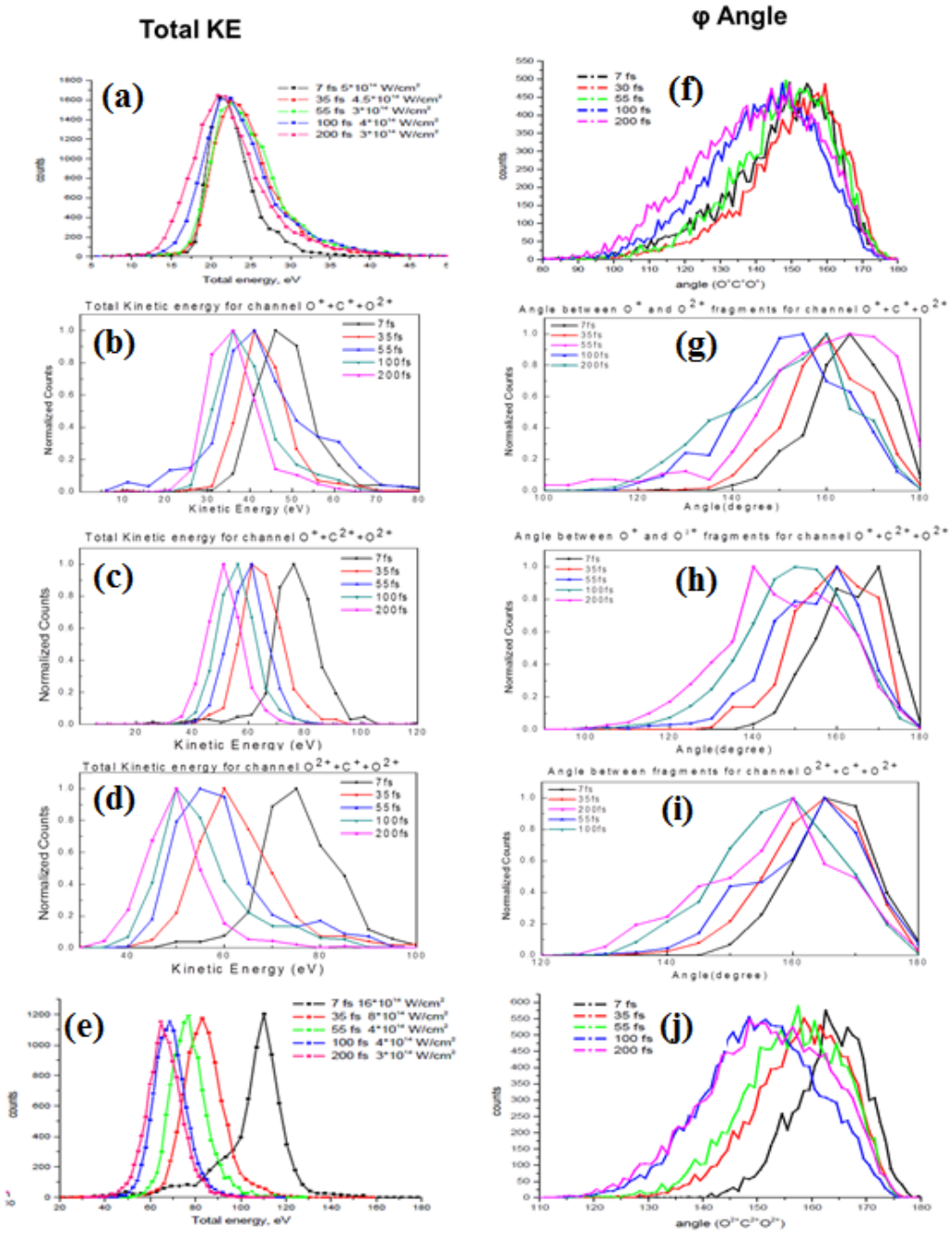

Figure 4-2 KER and angle distribution versus pulse length (a) and (f) $CO_2^{3+} \rightarrow C^+ + O^+ + O^+$, (b) and (g) $CO_2^{4+} \rightarrow C^+ + O^+ + O^{2+}$, (c) and (h) $CO_2^{5+} \rightarrow C^+ + O^{2+} + O^{2+}$, (d) and (i) $CO_2^{5+} \rightarrow C^{2+} + O^+ + O^{2+}$, (e) and (j) $CO_2^{6+} \rightarrow C^{2+} + O^{2+} + O^{2+}$ (CE) channels. Each curve corresponds to a certain pulse length: (black) 7 fs (red) 35 fs; (green) 55 fs; (blue) 100 fs; (purple) 200fs

4.6 Intensity dependence of the peak position of KER spectra

As discusssed in the context of Figure 4-1, in spite of the fact that the experiments have been performed with different intensities and pulse durations, The ratio of the C^{2+} to C^{+} signal counts has been kept almost constant. Furthermore in Figure 4-2 we have shown that there is a marked dependence of KER on pulse length but we should show that it is the pulse length which is the major factor and not the intensity which is also changing. To demonstrate this, and reinforce the importance of pulse length on the KER distribution, we conducted two different CEI experiments with single pulse duration but with two laser intensities. Figure 4-3 represents a comparison of KER spectra for the (2, 2, 2) channel obtained with 7 fs and I = 2×10^{15} and 1×10^{15}W/cm^2.
The peak of the KER spectra is at 110 eV and the shape of the KER spectra is almost independent of laser peak intensity.

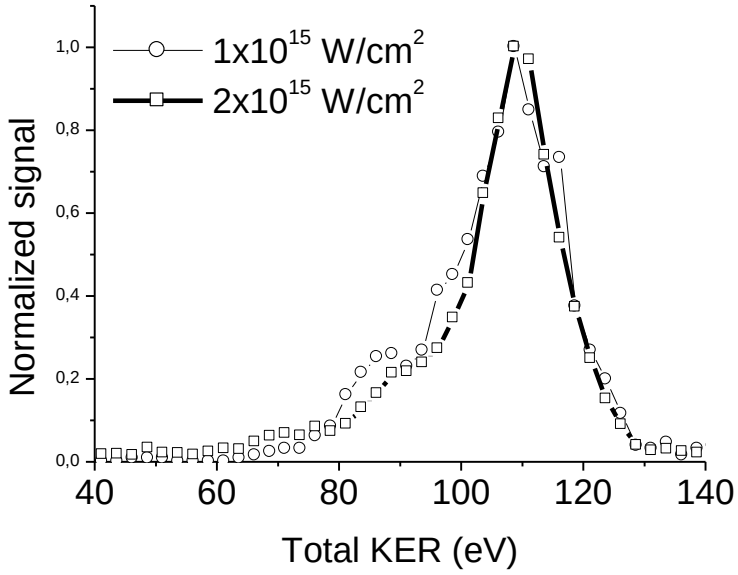

Figure 4-3 KER spectra for the (2, 2, 2) channel obtained with 7 fs and I = 2×10^{15} and 1×10^{15} W/cm^2.

4.7 Percentage of Coulombic KER

Figure 4-4 again presents the energy released, for a variety of final charge states as a function of pulse duration, but this time as a percentage of the energy which would be released if the process was purely Coulombic. To calculate the KER for a purely columbic process we express the energy as a percentage of the amount of energy released if the molecule fragmented into point-like ions along a purely Coulombic potential from the ground state equilibrium geometry. Figure 4-2 (a) - (e) and Figure 4-4 show that the KER depends significantly on the pulse duration for only the 4+ and higher charge states.

In detail, from 200 fs to 35fs, the KER increases from around 50% to 60% of the expected Coulombic values. For 7 fs pulses, there is a significant increase of KER up to 90% and above of the Coulombic value in some cases. If we relate the KER to the bond lengths at which the final charge state is populated, it is apparent that the molecule is being ionized at progressively longer bond lengths as the pulse duration increases, and reaches a critical bond length (R_C) at pulse duration near to 100 fs. For diatomic molecule, the observation of R_C has been explained by the presence of CREI [50][91][92]. A similar trend is found for all other channels resulting from charge states above 3+.

By contrast, the (1, 1, 1) channel exhibits a quite different behavior with KER at around 70-75% of the Coulombic value independent of the pulse duration. This independence KER to the pulse duration, never reported before, is summarized in Figure 4-2 (a) and Figure 4-4. The observation is consistent with dissociation from a non Coulombic potential, one in which bond length does not map onto the KER. The ground state of CO_2^{3+} exhibits this kind of behavior for R<1.7Å where the potential is weakly attractive; as can be seen in Figure 5 of reference [25]. When the dissociating wave packet reaches R_{CO} = 1.7Å it then experiences full Coulombic repulsion releasing approximately 70% of the energy expected from equilibrium plus energy accumulated on lower dissociative states. The results indicate that even with few-cycle pulses, it is not possible to retrieve the molecular structure of CO_2 using CO_2^{3+} as the final charge state.

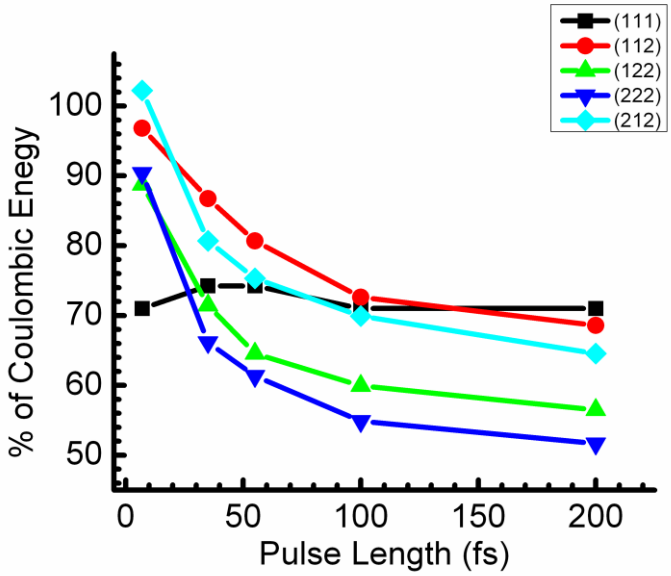

Figure 4-4 Ratio of KER to energy expected from the Coulomb explosion at the equilibrium of CO_2 (CE) as a function of the final charge states and pulse duration

With 7 fs duration and for final charge states higher than 3+, the KER is close to the value expected for Coulomb explosion from the CO_2 equilibrium geometry. For longer pulse duration, the total KER decreases and it becomes almost independent of pulse duration (>100 fs) in a similar fashion to the pulse duration dependence of KER from D_2 in a pulse longer than ~40 fs [66]. For D_2 the KER from Coulomb explosion becomes independent of pulse duration once the D_2^+ molecular ion stretches to $R_{C,}$ where CREI occurs [50], [91], [92]. In Figure 4-4, the variation in %CE (Coulomb Energy) between channels, for long pulse duration experiments, at first glance appears to indicate a variation in R_C with final charge state (assuming a Coulombic 1/R inversion, 50% of CE implies $R_C = 2R_{Equilibrium}$). However, to conclude this would be incorrect as this variation is mainly attributable to the contribution to the final channel KER from the dissociation of CO_2^{3+} (which does not change with pulse duration). In the case of (1, 1, 2), this is a large fraction of the final energy but becomes progressively less important for the 5+ (1, 2, 2) and the 6+ (2, 2, 2) charge states. In fact, it is quite straightforward to show that the actual value of R_C for the (1, 1, 1) to (1, 1, 2) step is between 1.85 and 2 Å [94]. This indicates that significant dissociative dynamics must be occurring on the 3+ charge state, in order to stretch from 1.7 Å to 2 Å.

The percentage of Coulombic KER for channel (1, 1, 2) is noteworthy, as it is higher than 100%, which is unexpected. We have however observed similar behavior in another set of experiments,

where the percentage of coulombic energy for a 7fs pulse CE experiment for CO_2, OCS, and CS_2 molecules have been compared to the results of a HCI impact experiments with the same targets [95]. Figure 4-5 features the variation of percentage of Coulombic KER against the charge states which reported in [95]. Clearly in, for HCI impact experiments the percentage of the coulombic potential energy is greater than 100%.

We speculate that the distribution of the electron around the fragment ions is more asymmetric rather than symmetric. If this is the case, we cannot presume the ions as positive point-like structures which are necessary in calculation of the pure coulombic potential energy.

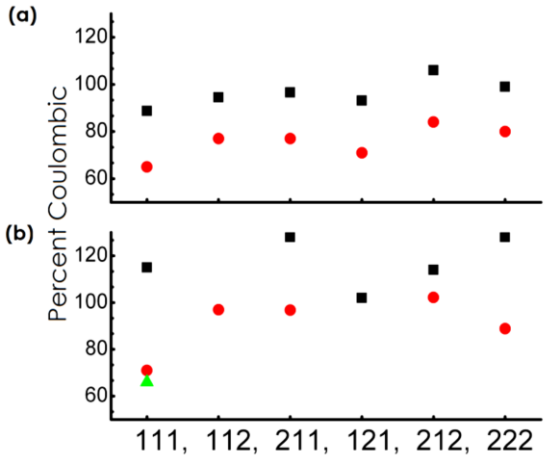

Figure 4-5 Percentage Coulombic energy released as a function of channels for sub 7fs laser pulse initiated ionization (red circles) and Ar^{8+} ion impact (black squares) for (a) OCS and (b) CO_2

4.8 Relating fragment ion KER to bending

It is stated in the previous section that the total KER is independent of the pulse duration for channel (1, 1, 1). This is attributed to dissociation from non-Columbic potentials, in which the KER is not indicative of the bond length. However, as Figure 4-2 shows the bend angle varies with pulse duration even for channel (1, 1, 1). As a consequently of this bend angle decrease, which is an indication that the molecule is undergoing dynamics despite the lack of evidence of dissociation from KER. One way to see this dynamics is to plot the KER of the individual fragment ions. Figure 4-6 presents the C^+ and O^+ KE spectra as a function of pulse duration.

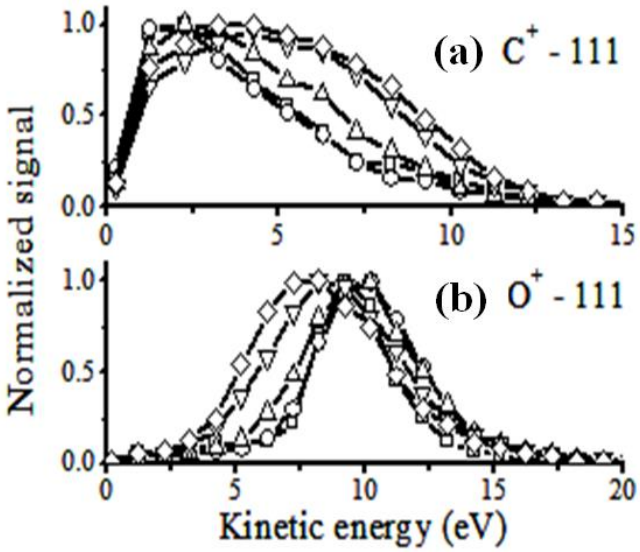

Figure 4-6 KER distribution of (a) C^+ and (b) O^+ as a function of pulse duration for the (1, 1, 1) channel final charge state, square 7 fs, circle 35 fs, triangle up 60 fs, triangle down 100 fs, diamond 200 fs, the laser intensities are: 7 and 35 fs; 5×10^{14} W/cm^2, 60, 100 and 200 fs; 3×10^{14} W/cm^2.

We observe that as the pulse duration increases, the C^+ KE spectrum broadens towards high energy, and correlates with an opposite behavior in O^+ which moves to lower KE. This is a significant observation as along with the previously observed change in φ it indicates bending dynamics on lower charge states (such as 2+). Our observations are the first which show the evolution of the wave packet over time as predicted by Sato et al. [25] who have modeled dissociation dynamics on the light dressed states of CO_2^{2+}, without considering the ionization step to CO_2^{3+}, and predicted bending in association with symmetric stretching to between 1.4 and 1.75 Å bond length on time scale of ~ 100 fs.

4.9 Dalitz plots for channel (1, 1, 1) to (2, 2, 2)

A third visualization method allows us to see the most complete picture of molecular dynamics. This method allows us to display the possible molecular dissociation geometries in a 2D histogram and categorize the possible break up channel for a triatomic molecule CO_2, the method is known as a "Dalitz plot" [96]. This technique has been successfully used for symmetrical molecules such as CO_2 [18], but has also recently been adapted to work with asymmetric molecules [37] such as N_2O (will be presented in details in chapter 5). In Dalitz plots, the y-axis shows the fraction of energy carried by

the middle ion, in this case carbon (C^+) (equation 4.1) while the x- axis shows the difference in the fraction of energy between the terminal ions in this case oxygen (O^+) and the other oxygen (equation 4.2).

$$y = \varepsilon_{C^+} - \frac{1}{3} \tag{4.1}$$

$$x = \frac{\varepsilon_{O^+} - \varepsilon_{O^+}}{\sqrt{3}} \tag{4.2}$$

Figure 4-7 presents theoretically the Dalitz plots of CO_2^{3+} break up into different fragment ions. Each point of this plot represents a specific arrangement of the momentum vectors. For instance, bending of the molecule in a concerted dissociation process, where the bonds expand equally results in a reduced angle between the outside momentum vectors, and this reduction has the effect of imparting more momentum to the middle ion, carbon. This process is associated with approximately vertical changes from the equilibrium point on the Dalitz plot. In addition the process where the molecular bonds break one at a time (stepwise) can be identified by signal along a diagonal line form bottom center to top right or left. The geometry of the molecule and the momentum vectors resulting from the break up are of course related**.**

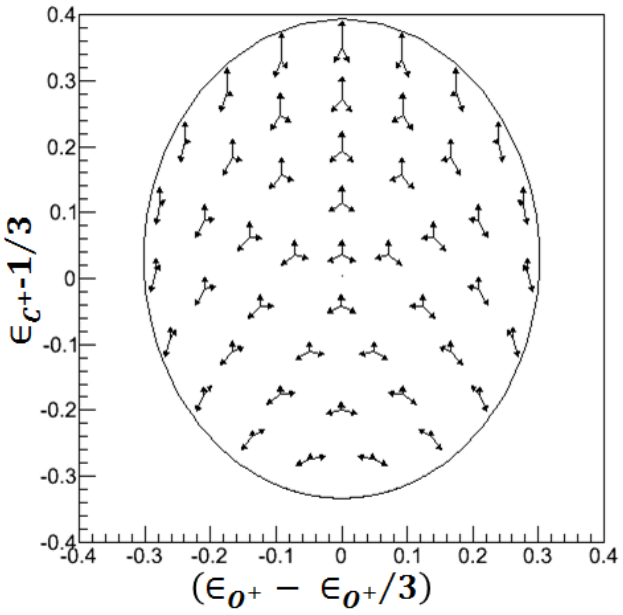

Figure 4-7 Full Dalitz plot map of momentum vectors theoretical calculation of CO_2^{3+} break up into different fragment ions

Figure 4-8 features the variation of Dalitz plots against pulse duration for channel (1, 1, 1). Both concerted and stepwise processes of CO_2^{3+} can be traced in these plots. Firstly it is apparent that the concerted process dominates. This information is not available from the simple energy distributions described in the previous section. The concerted processes can be tracked by the population of the green spots around the equilibrium point. As the pulse duration increases, the population of the concerted processes shifts vertically from the equilibrium point towards the higher carbon KER values.

In addition to monitoring concerted processes in channel (1, 1, 1), the stepwise processes can be traced by the extent of the diagonal branching in the Dalitz plots. Firstly the two branches represent just one process $CO_2^{3+} \rightarrow CO^{2+} + O^+ \rightarrow C^+ + O^+ + O^+$. Points on Figure 4-8 separated further horizontally in the two branches from the main distribution represent rotation of the metastable CO^{2+} molecule before it breaks up. Figure 4-8 suggests that although the concerted process involves increasingly bent molecules with increasing pulse length, the stepwise channel still persists.

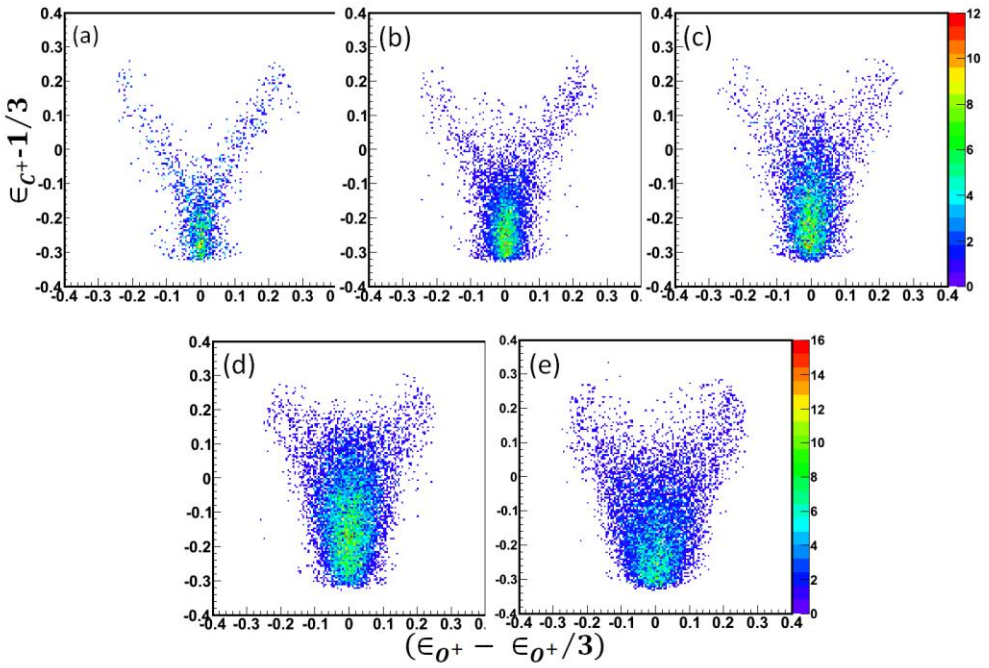

Figure 4-8 Dalitz plots, (a) 7 fs, (b) 35 fs (c) 55 fs (d) 100 fs (e) 200 fs for the (1,1,1) channel (I between 4×10^{15} and 2.5×10^{14} W/cm^2).

4.10 Newton plots

The Newton plot technique is another means to monitor the concerted and stepwise processes. The Newton plot depicts the three momentum vectors of the fragments ions resulting from the break up of a triatomic molecule (in the molecule frame). The vectors can be plotted on a plane as are triatomic molecules. We can create a maximum of three Newton plots for a triatomic molecule, one for each fragment ion, but because of its symmetry, the (1, 1, 1) channel of CO_2 has only two distinct ions. The most revealing plot is for the O^+ ion. We rotate the molecule such that the oxygen ion momentum points along the positive Y-axis, the other oxygen momentum is confined to the negative half of the X-axis and the carbon momentum is confined to the positive half of the X-axis. With one O^+ momentum vector restricted to a point two island distributions represent the momentum of the C^+ and other O^+ ions. A stepwise process has a distinct appearance due to the lifetime of the metastable CO^{2+} which can rotate one or more times before it dissociates. This results in two semi-ring structures which come out of the concerted process islands in the Newton plot. Figure 4-9 displays Newton plots for (1, 1, 1) with pulse duration from 7 to 200fs where the momentum from each coincidence has been scaled to the momentum of the O^+. The change in the concerted channel with longer pulse length is apparent by the stretching of the O^+ island in Figure 4-9 (a), (c), (e), (g) as the bonds become increasingly asymmetric, such that the true stepwise channel becomes just a tail on the extended island by 200fs. This process is less clear in the C^+ plots but results in a widening of the plot in the vertical direction.

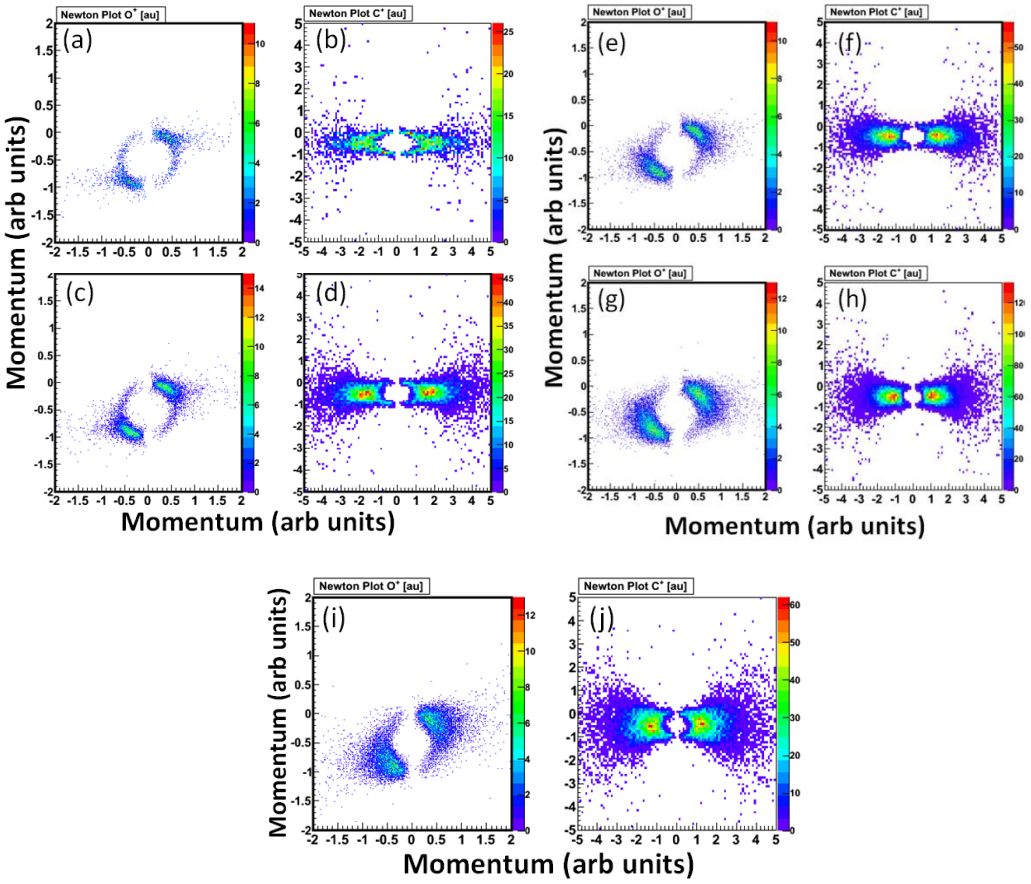

Figure 4-9 Newton plots: momentum vector of one O^+ ion, concerted break up mechanism are identified by two island distributions represent the momentum of the C^+ and other O^+ ions, two semi-ring structures which come out of the concerted process islands in the Newton plot shows the stepwise proses $CO_2^{3+} \rightarrow CO^{2+} + O^+ \rightarrow C^+ + O+ + O^+$.

4.11 Molecular geometry reconstruction

By performing full coincidence momentum measurements, it is possible to retrieve the molecular structure [74]. Because its energy release is close to Coulmbic, the highest observed charge state 6+ (2, 2, 2) will be used to perform this retrieval. A simplex algorithm is used to iteratively optimize the agreement between the measured momenta and the asymptotic momenta generated by a simulation of the Coulomb explosion of the molecule in the 6+ state. Recently, this algorithm has been refined and presented in detail [97]. The algorithm first presumes a hypothetical structure for a desired molecule before explosion. Then it conducts a series of calculations to measure the total momenta of the hypothetical molecule undergoing a coulombic explosion. The resultant measurements then are

compared with the experimentally detected total momenta of the fragment ions. This algorithm continues by presuming other possible structures for the target molecule if the theoretical and experimental values of the momenta do not match. If the theoretical and experimental values coincide, the hypothetical structure is assigned to the tested molecule. Figure 4-10 (a) presents the retrieved molecular structure ($R_{CO} \approx 1.3$ Å and $\theta_{OCO} \approx 168^o$) for 7 fs pulses which is very close to the equilibrium geometry ($R_{CO} = 1.16$ Å and $\theta_{OCO} \approx 172^o$ [15]).

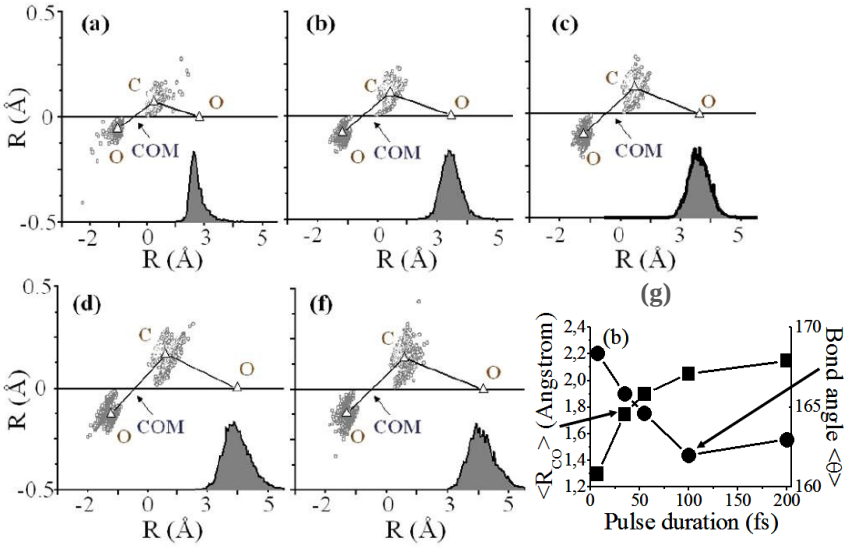

Figure 4-10 Reconstruction of molecular structure for (a) 7fs, (b) 35fs, (c) 55fs, (d) 100, (f) 200fs pulse duration using the (2, 2, 2) channel. (g) Average CO bond distance and bend angle retrieved as a function of pulse duration.

For longer pulses Figure 4-10 (b)-(f) the molecule expands and undergoes bending.
In Figure 4-10 (g) significantly, the molecular structure of CO_2 remains almost unchanged for pulse duration longer than 100 fs ($R_{CO} \approx 2.1$ Å and $\theta_{OCO} \approx 163^o$).
Molecular structures presented in Figure 4-10 reveal that CO_2 undergoes ultrafast symmetric stretching in the presence of the laser field. Figure 4-10 indicates that this symmetric stretching cannot be explained by nuclear dynamics on the CO_2^{2+} potential energy surface since the KER from CO_2^{3+} is almost independent of pulse duration. As mentioned previously, Sato et *al.* calculated that about 100 fs is required for symmetric bond stretching between 1.4 and 1.75 Å to occur on light

dressed CO_2^{2+} [25], which is significantly shorter than the measured R_C. This is confirmed in Figure 4-5 where we show that R_{CO} is already stretched to ~ 1.75 Å with pulse duration of 35 fs.

4.12 Theoretical calculation and analysis

The strong dependence of KER on pulse duration is only observed when the 4+ charge state is reached, revealing significant dissociative dynamics on the 3+ and higher charge states, with 3+ providing the first step of CREI. To elucidate this mechanism, we have calculated the ionization rate and the electronic structure of CO_2^{3+} as a function of R_{CO} assuming a symmetric linear geometry which is a valid approximation based on the structure presented in Figure 4-10.

Professor Andre Bandrauk and coworkers (Universite de Sherbrooke) performed nonlinear non-perturbative TDDFT using the statistical average of orbital potential (SAOP) local density potential to calculate the ionization rate [98] of CO_2^{3+} as a function of R_{CO} with the following parameters: $I=8\times10^{14}$ W/cm^2, λ = 800 nm, τ = 6 optical cycles. Triple-zeta (TZ2P) Slater-Type Orbital (STO) basis set have been used for all atoms. A symmetric linear geometry for CO_2^{3+} was assumed. For each R_{CO}, two calculations were performed; the molecular axis is either parallel or perpendicular to the polarization axis. Figure 4-11 shows the result of calculated and measured R_{CO}. The ionization rate per optical cycle is presented in Figure 4-11(a).

The ionization rate when CO_2^{3+} is perpendicular to the laser polarization axis remains constant for R_{CO} longer than ~1.7 Å while it continues to increase when the molecule is parallel. At the largest R_{CO} where calculations can be performed, near 1.9 Å, the ionization rate is ~5 times larger when CO_2^{3+} is parallel to the polarization axis. Therefore, we conclude that as CO_2^{3+} is symmetrically breaking apart within the laser field, the intensity required to reach high charge states decreases due to increased ionization rate and the distribution of high charge fragments such as O^{2+} becomes highly anisotropic, and peaked along the polarization axis. This explains the experimental results presented in Figure 4-1.

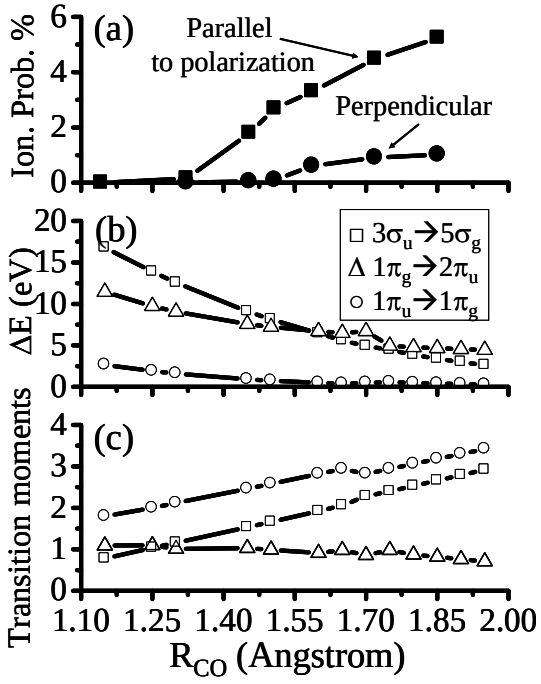

Figure 4-11 Results of numerical simulations (a) Ionization rate per optical cycle as a function of R_{CO} for CO_2^{3+}. (b), (c) Energy gaps (eV) and transition moments (a.u.) for the parallel transitions in CO_2^{3+}.

From the nonlinear non-perturbative TDDFT calculations, we can identify the probability of ionization as a function of the molecular orbital. We observe that the ionization probability is mostly coming from the $3\sigma_u$ orbital when CO_2^{3+} is parallel to the polarization, while it comes from the $1\pi_u$ orbital for the perpendicular case. To understand these results, time-independent DFT calculations [99] were performed to characterize the electronic structure of CO_2^{3+} as a function of R_{CO}. At the equilibrium of CO_2, we find for the 3+ charge state that the HOMO in $D_{\infty h}$ is an anti-bonding type, $1\pi_g$, formed of π lobes lying perpendicular to the internuclear axis and located on the oxygen atoms, while the HOMO-1 is $3\sigma_u$, and the HOMO-2 is $1\pi_u$. At R ≈ 2 Å, they become almost degenerates. The energy gaps and the transition moments for parallel transitions; $3\sigma_u \rightarrow 5\sigma_g$ (Σ), $1\pi_u \rightarrow 1\pi_g$ (Π_a), and $1\pi_g \rightarrow 2\pi_u$ (Π_b), are presented in Figure 4-11(b) and (c).

To explain CREI in term of strongly coupled CR states, both the Σ ($3\sigma_u \rightarrow 5\sigma_g$) and the Π_a ($1\pi_u \rightarrow 1\pi_g$) parallel transitions can result in charge localization. The ionization rate is however much higher from the $3\sigma_u$ as mentioned previously. Charge localization from the Π_a transition results in a pshape orbital with its main axis perpendicular to the laser polarization, from which the ionization rate is suppressed

[100]. Finally, the Π_b transition is much less important because at large R_{CO}, the $2\pi_u$ becomes localized on the carbon as a 2p atomic orbital in the center of the molecule while the electronic density of the $1\pi_g$ orbital is located on the oxygen atoms in a 2p atomic orbital separated by $2R_{CO}$. The resulting transition moment and radiative coupling vanishes with increasing R_{CO}.

The theoretical result for dissociation and fragmentation of triatomic molecule CO_2 which discussed in detail, along with the H_2^+ result [101] is depicted in Figure 4-12. In this figure right plot presents the two lowest 1D potentials for CO_2^{3+} and left plot H_2^+ gerade and ungerade potentials. For the CO_2 molecule in its equilibrium R_{C-O} = 1.15 Å, 16 eV energy is required to couple the bonding $5\sigma_g$ and anti-bonding $4\sigma_u$ orbitals, which is more than 10 photons of 800 nm laser pulse. While increasing the C-O bond to 2.2 Å, the energy gap reduces to 1.5 eV which is equal to the energy of one photon of 800 nm laser pulses. This is sufficient for coupling of $5\sigma_g$ and anti-bonding $4\sigma_u$ orbitals [81].

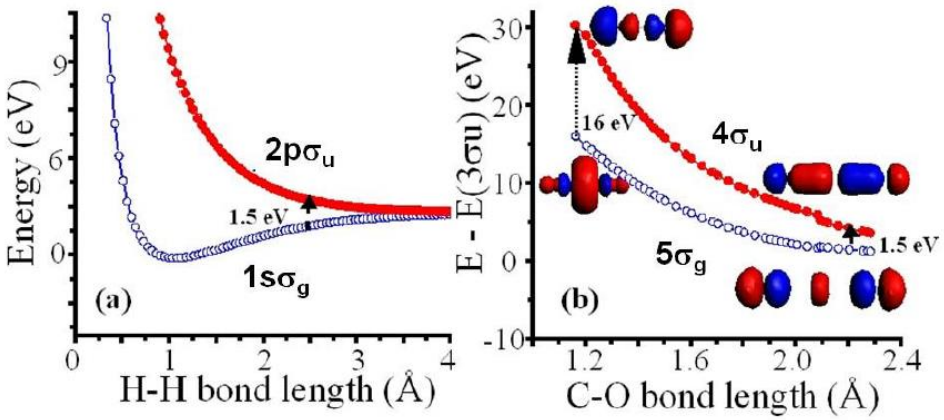

Figure 4-12 Gerade and ungerade states for (a) H^{2+} ion, (b) CO_2^{3+}, the shapes of molecular orbitals at the equilibrium and the critical internuclear distances are shown Reprinted with permission from [81]).

4.13 Conclusion

In conclusion, we have made the first clear systematic measurements and provided interpretation of the effect of laser pulse duration on dissociative ionization to high charge states for a polyatomic molecule, CO_2. By changing the pulse duration, we have been able to definitively measure the molecular geometry where CREI occurs ($R_{CO} \approx 2.1$ Å and $\theta_{OCO} \approx 163^o$). The experimental results clearly indicate the importance of dissociation dynamics on the CO_2^{3+} charge state leading to structural deformation observed in the higher charge states. As the CO_2^{3+} breaks apart, the numerical simulations clearly show that the ionization rate increases rapidly when the molecule is aligned along the laser polarization axis because of strongly coupled CR states ($3\sigma_u \rightarrow 5\sigma_g$). This requires that enough time is given to CO_2^{3+} and subsequent charge states to stretch up to the critical distance of R_{CO}~2 Å, a condition satisfied with laser pulse duration equal to or longer than 100 fs.

Chapter 5

N_2O ionization and dissociation dynamics in intense femtosecond laser radiation, probed by systematic pulse length variation from 7 to 500 fs

This chapter describes a series of experiments in which we performed measurements as a function of pulse duration of ionization and fragmentation of the asymmetric molecule N_2O in intense femtosecond laser radiation. The pulse length was varied from 7fs to 500fs with intensity ranging from 4×10^{15} to 2.5×10^{14} (W/cm^2) respectively. Time and position sensitive detection allows us to observe all fragments in coincidence. By representing the final dissociation geometry with Dalitz and Newton plots, we can identify the underlying break up dynamics. First, we observe here for the first time that there are two stepwise dissociation pathways for N_2O^{3+}: (1) $N_2O^{3+} \rightarrow N^+ + NO^{2+} \rightarrow N^+ + N^+ + O^+$ and (2) $N_2O^{3+} \rightarrow N_2^{2+} + O^+ \rightarrow N^+ + N^+ + O^+$ as well as one for $N_2O^{4+} \rightarrow N^{2+} + NO^{2+} \rightarrow N^{2+} + N^+ + O^+$. Next we show that the N_2^{2+} stepwise channel is suppressed for longer pulse length, a phenomenon which we attribute to the influence which the structure of the 3+ potential has on the dissociating wave packet propagation. We also discuss in detail the problematic (1, 1, 1) channel dissociation. Finally, by observing the total kinetic energy released for each channel as a function of pulse duration, we show the increasing importance of charge resonance enhanced ionization for channels higher than 3+. This work was a collaborative effort of all the authors of [102]. My involvement in this work consisted of participation in the experimental setup, I took principal responsibility for and carried out data analysis, and graphical representation and finally manuscript writing and preparation. Introduction

Intense femtosecond lasers are ideal tools for imaging molecular structure and dynamics, and has been used for more than twenty years primarily through the technique of Coulomb Explosion Imaging (CEI), [20], [25], [26], [44], [50], [53], [68], [87], [103], [104] and more recently with methods such as electron ion coincidence[105], and high harmonic tomography [68], [106–109]. Theoretical advances have identified the origin of phenomena observed experimentally such as CREI, [50] recollision physics [49] and laser induced dynamics [25].

We have recently made an experimental advance by varying the pulse duration from few cycles (<10fs) to 100s of fs and making a series of careful measurements [26]. This has revealed aspects of laser-molecule interaction not visible in earlier work which used a fixed pulse duration [23], [59],

[74], [87], [103], [17]. This improvement is analogous to the increase in information retrieved about dynamics from a movie compared to a single snapshot. The new approach introduces a multi-dimensional aspect to the science of non-perturbative laser-molecule interaction. We refer to this approach as FEmtosecond Multi-PUlse Length Spectroscopy (FEMPULS) in order to distinguish it from previous work [110] [111] which used standard TOF techniques to monitor the fragmentation of molecules. Here as previously [26] we study dynamics by coincidence methods, to record individual fragment momenta, molecular geometry, energy release and modes of dissociation.
By monitoring KER of the observed dissociation channels of CO_2 from 3+ to 6+ using the 3D-ion-momentum coincidence method [15], [17], [22], [23], [64], [74] we were able to show that the KER from fragmentation on the 3+ charge state is nearly constant with pulse duration even for few cycle pulses. When we compare the KER with a simulation of the Coulomb explosion (CE) assuming point-like ions, we found that the measured energy release is around 70% of the Coulombic energy. This contrasted with the higher channels such as 6+ (2, 2, 2) which exhibited low energy release of close to 50% for long pulses, and high energy release up to 90% for short 7 fs pulses. The pattern not only revealed that the 3+ state is never Coulombic but also pinpointed it as the state from which CREI to higher charge states is initiated. In addition, by monitoring the individual energy released by the respective fragment ions, we showed that there was a progression in molecular deformation with pulse duration. Here we develop the method further by employing Dalitz plots in order to distinguish concerted and sequential processes as well as geometry deformation [96]. We apply the method to the asymmetric triatomic molecule N_2O.

5.1 Previous work

N_2O has been the subject of experiments using both uncorrelated and correlated fragment detection techniques over the past twenty years. All studies have used multi-cycle pulses longer than 50 fs and have endeavoured to determine the mechanism of dissociative ionization by determining the channels of fragmentation, measuring the apparent molecular geometry, and the rate of ionization. Frasinski et al. [112] reported for the first time observation of CE in N_2O. They applied the 3D covariance mapping technique to detect correlated ions. The authors employed a laser of wavelength 600nm, pulse length 0.6ps, repetition rate10 Hz, and focused intensity of 10^{15} W/cm^2. Using the original TOF design, the TOF axis and the E field of the laser pulse were aligned. Here, the fragment ions were emitted selectively in direction of the TOF axis. Afterwards, the fragment ions are accelerated forward and backward via DC electric field to the detector. As a result of this process, a

pair of ions is detected. Figure 5-1 presents the time-averaged TOF spectrum along with a covariance map. The two islands in the top right-hand corner of this figure reflect the correlation of $N_f^+ + NO_b^+$ and $N_b^+ + NO_f^+$ (b: backward, f: forward, m: middle). Other various channels and correlations emerge separately like islands on the covariance map. Islands (a), (b), (c), (d), (e) and (f) represent correlation of $N_b^{2+} + O_f^{2+}$, $N_b^{2+} + N_m^{2+}$, $N_m^{2+} + O_f^{2+}$, $N_m^{2+} + N_f^{2+}$, $N_f^{2+} + O_b^{2+}$ and $N_m^{2+} + O_b^{2+}$ respectively. The islands (g) and (h) close to the autocorrelation line is associated with $C^+ + C^+$ correlation from residual gases in the chamber.

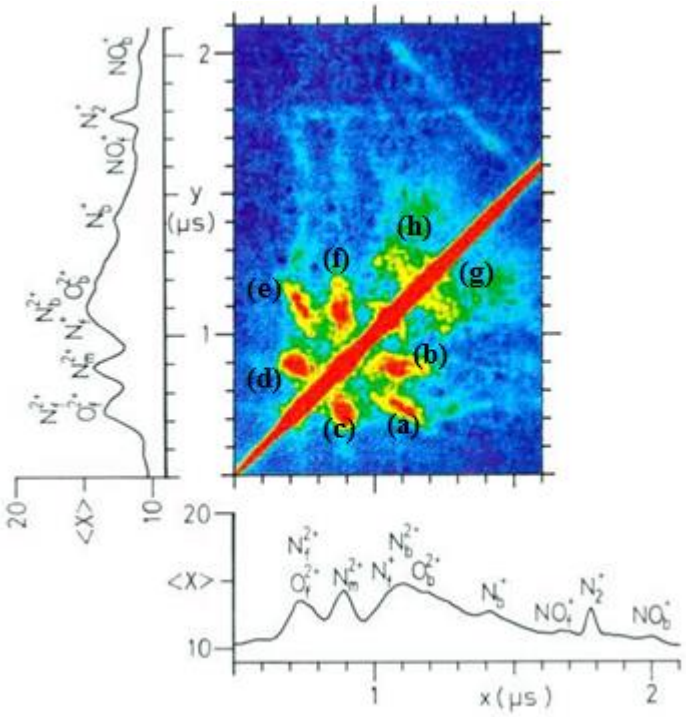

Figure 5-1 Two-dimensional map for N20, the conventional time-averaged TOF spectrum is placed along the x and y axes. The figure borrowed from reference (Reprinted with permission from [112])

As a result, they identified the two body explosion pathway, $N_2O^{2+} \rightarrow N^+ + NO^+$; and the three body pathway, $N_2O^{6+} \rightarrow N^{2+} + N^{2+} + O^{2+}$. Because they observed no $N_2O^{3+} \rightarrow N^+ + N^+ + O^+$ pathways in the covariance map, they concluded that for the three body pathway ionization of $N_2O \rightarrow N_2O^{6+}$ happened non-sequentially for all six electrons. This result infers that in the intense laser field, only N_2O^{2+} and N_2O^{6+} are formed with no sign of the intermediate states: N_2O^{3+}, N_2O^{4+}, and N_2O^{5+}.

Later, in order to clarify the origin of the tendency in the formation of N_2O^{6+} Hishikawa et al. [103] performed a series of experiment on N_2O. They employed a 100 fs laser pulse and used the

uncorrelated MRMI method and observe additional channels $N_2O^{d+} \rightarrow N^{a+} + N^{b+} + O^{c+}$, d (3-6) = a (1-2) +b (1-2) + c (1-2).

Following up this study using the fully correlated 3D-ion momentum coincidence method with 60 fs pulse duration [104], this group were able to identify a correlation between a decrease in the N-N-O bend angle and a stretch in the two bonds in the concerted pathway in which the N-N and N-O bonds are broken simultaneously. Moreover, this new method allowed the observation of the concerted break up, $N_2O^{3+} \rightarrow N^+ + N^+ + O^+$, and also stepwise break up through the channel $N_2O^{3+} \rightarrow N^+ + NO^{2+} \rightarrow N^+ + N^+ + O^+$.

In this study, we use the FEMPULS technique with laser pulse duration from 7 to 500 fs and applying 3D-ion momentum coincidence measurements of dissociative ionization in order to study the dynamics of N_2O in the ionization states N_2O^{n+} (n = 3-6). The aim of the work is to search for new stepwise processes and to understand the dynamics of the molecular dissociation process during the laser pulse. We will also compare the importance of charge resonance enhanced ionization for the asymmetric N_2O molecule, to that observed and discussed (chapter 4) previously for the symmetric isoelectronic CO_2 molecule.

5.2 Experimental Apparatus

Our experimental setup has been presented previously in detail in the experimental section (chapter 2). Briefly, a multi KHz Titanium-Sapphire femtosecond laser at the ALLS produced pulses at 800nm and 35 fs. By propagating the laser beam through a hollow core fibre (HCF) filled with Argon and applying dispersion compensation using chirped mirrors, we were able to generate few-cycle pulses (7 fs). Moreover, by putting the HCF under vacuum, we can generate different pulse durations from 35 to 500fs, by applying second order dispersion ($\Phi^{(2)}(fs^2)$) from an acousto-optic programmable dispersive filter (Dazzler) located in the stretcher of the Titanium-Sapphire amplifier. This is a legitimate method where multiple ionization and high field molecular physics are under investigation. Chirp effects on fragmentation of singly ionized complex molecules have been examined by a number of investigators, and the conclusion of careful and systematic experiments [110] [111] indicated that quadratic chirp is significant only in its influence on the pulse length. In other words the final dissociation products are determined by the pulse length only and not by the sign of the linear frequency chirp. Deviations from this general pattern have been observed but only on the 1% level, attributed to pump and dump effects on small populations of specific fragment channels [110]. This is not surprising in the near IR where photons are neither resonant with the electronic nor the

rovibrational levels, and so control through simple chirp direction is not favored in small molecules. Control of molecules has been pursued for a number of years with various techniques such as adiabatic rapid passage (ARP) using visible to UV light [113] and vibrational ladder climbing, resulting in chirped pulse dissociation being only accessible in the mid IR [114]. In the near IR it has been possible to pursue control, but only by employing a more complex, difference frequency method in Raman chirped adiabatic passage (RCAP) [115]. This gives us great confidence that employing quadratic phase from a Dazzler is only affecting molecular dynamics through the influence of pulse length.

A parabolic mirror (f = 10 cm) focused the laser pulses on to a well-collimated supersonic jet of N_2O and a uniform electric field directed the fragment ions toward a time and position sensitive delay-line detector (RoentDek Handels GmbH). This allows us to determine the full 3D momenta of all the ions produced in Coulomb explosion in coincidence. If the total momentum of the detected fragments was close to zero ($< 5\times10^{-23}$ kg·m/s), then we considered that they came from a single molecule.

In order to deal with the degeneracy in position of the two N ions, we have further developed the algorithm of Wales et al [37] to allow for the existence of simultaneous molecular identifications for any set of three ions which originate from a single molecule. This correction is necessary even for count rates lower than one molecule per laser shot, but in practice we can handle high count rates of several molecules per laser shot.

5.3 TOF spectrum for dissociation along and perpendicular to the laser field polarization

Figure 5-2 shows a comparison between TOF spectra for 7 fs laser pulses with intensity I = 4×10^{15} W/cm^2, and 200 fs, 4×10^{14} W/cm^2 pulses.

The first observation is that the much higher peak intensity at 7 fs does not result in higher ionization states with the ratios of N^{2+}/N^+ and O^{2+}/O^+ very similar for the two plots. This confirms that ionization of N_2O to high charge states is much easier for multi-cycle pulses, i.e. CREI is suppressed with few-cycle pulses [66]. In addition, for 200 fs duration pulses, the O^{2+} peaks are more distinct than those at 7 fs which indicates higher kinetic energy release for the shorter pulse. Furthermore at 200 fs the backward O^{2+} peak is relatively narrow and distinct from the other doubly charged fragment ions, whereas for the 7 fs pulse, the peak is wide and merges with the other peaks. This is because alignment of the molecule with the laser field (and thus the TOF axis) becomes much less important with few cycle pulses, resulting in ions with reduced momentum component along the TOF axis.

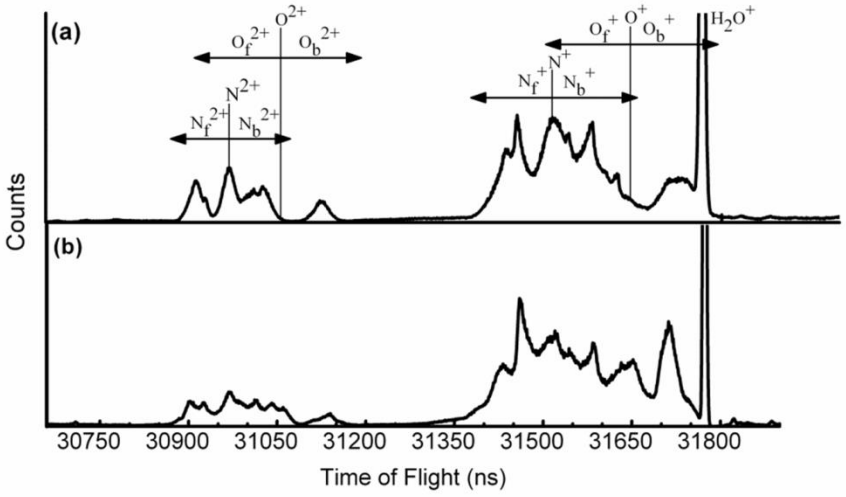

Figure 5-2 TOF spectra for N_2O at (a) 200 fs, I = 4×10^{14} W/cm^2, and (b) 7 fs, I = 4×10^{15} W/cm^2. Vertical lines indicate the flight time for an ion of zero initial momentum along the TOF axis and the horizontal arrows indicate the range of arrival times observed for the fragment ion, subscripts f and b indicate forward moving and backward moving ions.

5.4 Intensity dependence of the peak position of KER release

In order to establish that it is the pulse duration which is the dominant factor modifying the dynamics as we change the pulse shape, and not the peak intensity which is clearly also changing, we compare spectra recorded at different intensities. Figure 5-3 shows the KER for the 3+ ionization channel (1, 1, 1) of N_2O at (a) 7 fs, (b) 100 fs, and (c) the (2, 2, 2) channel of CO_2 for comparison. In each case, change in intensity by a factor of two gives rise to minimal difference in the shape of the KER distribution.

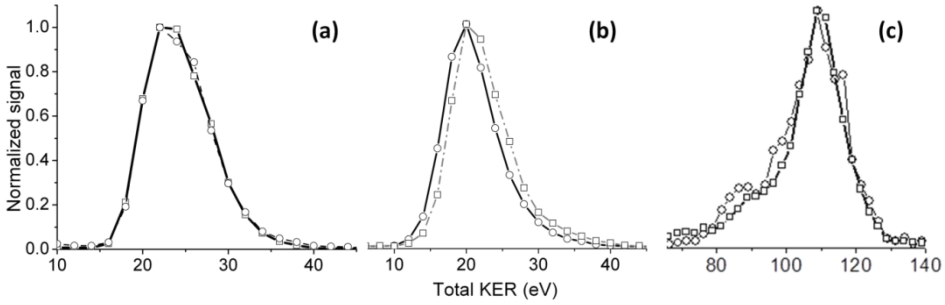

Figure 5-3 KER for the fragmentation of N_2O at different intensities (a) N_2O (1, 1, 1) channel with 7 fs pulses for I = 2×10^{15} W/cm^2 (circles) and 4×10^{15} W/cm^2 (squares), (b) N_2O (1, 1, 1) channel with 100 fs pulses for I = 3.5×10^{14} W/cm^2 (circles) and 7×10^{14} W/cm^2 (squares) and for comparison (c) CO_2 (2, 2, 2) channel with 7 fs pulses for I = 2×10^{15} W/cm^2 (circles) and 1.2×10^{15} W/cm^2 (squares).

5.5 Dalitz plots for channel (1, 1, 1)

In order to track the possible molecular dissociation channels for N_2O^{n+}, we use the well-established Dalitz plot technique [96] [18]. This technique has been successfully used not only for symmetrical molecules such as CO_2 [26], but has recently been shown to work with the asymmetric molecule OCS,[37] and is therefore appropriate for N_2O. Figure 5-4 shows the Dalitz plots and depicts the (1, 1, 1) channel for 7 fs pulse duration and shows a number of features. In this plot, the y-axis shows the fraction of energy carried by the middle nitrogen ion (N_m^+) while the x-axis shows the difference in the fraction of energy between the terminal nitrogen (N_t^+) and oxygen ions. Each point of this plot represents a specific arrangement of the momentum vectors (Figure 5-4 (a)). The Dalitz plot therefore works best when the three ions are each distinct and can be explicitly assigned. This means that for N_2O we must attempt to distinguish between the two N ions. Our data acquisition process designates

three TOF regions, one for the nitrogen ion moving toward the detector (the detector axis is aligned with the laser polarization) which we deduce to be the terminal ion N_t, one for the nitrogen ion with near zero velocity component along the detector axis, which we deduce is the middle ion N_m, and one for the oxygen ion moving away from the detector. In the case where the molecule breaks up with both bonds cleaving at the same time in a concerted process, these designations are reliable especially for long pulses where the molecules are predominantly aligned with the laser polarization (and therefore to the TOF axis). In the case of N_2O, even if the molecule breaks up from a linear geometry, the middle nitrogen will have non-zero momentum and energy, positioning the equilibrium geometry (calculated using GAMESS) at ($x = 0.0183$, $y = -0.326$). The geometry of the molecule and the momentum vectors which result from break up are of course related. Bending of the molecule in a concerted dissociation process results in a reduced angle between the momentum vectors of the outer ions, and this has the effect of imparting more momentum to the middle nitrogen ion. This process is associated with approximately vertical changes from the equilibrium point on the Dalitz plot. Points further separated horizontally from the main distribution represent increasing amounts of asymmetry in bond length, and are indicative of stepwise processes. This represents spreading of the wave packet in terms of the two bond coordinates, i.e. increasingly asymmetric bond distributions. Note that the Dalitz method does not distinguish between KER; it only cares about the distribution of kinetic energy within the molecule. As shown by [18] the stepwise channels may result from lower KER than the concerted processes. Figure 5-4 (b) depicts the (1, 1, 1) channel for 7 fs pulse duration and shows a number of features. The peak in signal density is close to the region expected from the nearly linear equilibrium geometry. However the gray oval indicates that there is a distribution of concerted processes which result from molecules of varying bend angles. Break up which involves production of a metastable NO^{2+} ion appears as data along a diagonal indicated by the yellow long dashed oval. The designation of this channel is straightforward to make, and can be modeled as a rigid NO^{2+} molecule which rotates as it separates from the N^+ ion [18], followed by a Coulombic dissociation at a later time. The uniform nature of the branch stretching to the edge of the Dalitz plot indicates that the NO^{2+} ion is metastable for a time which is long compared to its rotational period. We will refer to these diatomic ions as metastable, to distinguish them from the ions which reach the detector intact, which we will refer to as stable (although they are in fact quasi bound), and the ions which dissociate on the timescale of the laser pulse which may participate in concerted bond stretching processes. The process was previously observed for 60 fs pulse duration [104] where it was the only stepwise process observed.

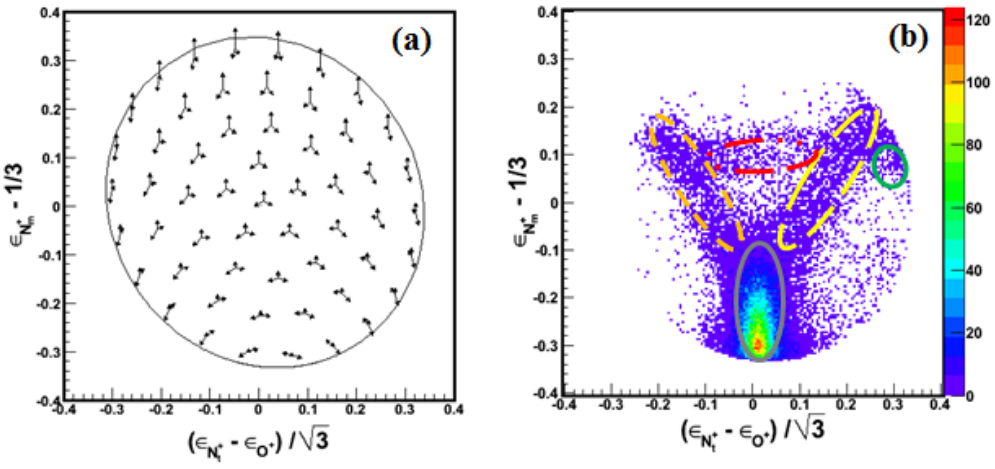

Figure 5-4 Full Dalitz plot for the (1, 1, 1) channel of N_2O at 7 fs, (a) Map of momentum vectors; (b) The gray oval represents the concerted processes in which bonds break together, The dashed orange oval on the left side represents the stepwise processes for $N_2O^{3+} \rightarrow N_2^{2+} + O^+ \rightarrow N^+ + N^+ + O^+$, and the long dashed yellow oval on the right side represents the stepwise processes for $N_2O^{3+} \rightarrow N^+ + NO^{2+} \rightarrow N^+ + N^+ + O^+$. The red dashed dot oval represents the same process as the yellow region but with the central and the terminal N ions misidentified. The green circle represents false coincidences from low momentum O^+ originating from H_2O.

A striking second stepwise process however appears here, which proceeds via the N_2^{2+} moiety indicated by the orange dashed diagonal oval. Again this process can be modeled by the breaks up of a rigid rotor and is simple to identify. This is the first time that fragmentation of N_2O into a metastable N_2^{2+} ion has been reported. The two nitrogen ions – the terminal ion N_t^+ and the middle ion N_m^+ – produced in the (1, 1, 1) channel are identical, and therefore in certain circumstances it is impossible to determine which of the two is the N_t^+ and which is the N_m^+ when detected in coincidence. For the concerted channel, the position can be inferred because the middle ion is released with low momentum while the end ion has high momentum in the opposite direction to the oxygen ion, but for a stepwise channel, ambiguity can develop due to rotation of the metastable molecular ion during dissociation. The Dalitz plot which explicitly requires a distinction between the terminal ions and the central ion is therefore sensitive to this ambiguity. In Figure 5-4 (b) the red dashed dot oval results from incorrect identification of the nitrogen ions from the NO^{2+} stepwise channel. Further investigation of the origin of this ambiguity reveals that it occurs when the initial orientation of the molecule is perpendicular to the laser polarization and the TOF axis. One final

region where persistent false coincidences occur is shown by a green circle. Here low energy N_2O explosion events produce low momentum O^+ ions, which are difficult to distinguish from those originating from H_2O which is present as a background gas, such that there is approximately one molecule in the focus for every laser shot.

5.6 Dalitz plots and the problematic (1, 1, 1) channel

It is important to understand how the limited TOF ranges selected to represent the (1, 1, 1) channel in the previous section, restrict both the alignment and orientation of molecules which can contribute to the Dalitz plot. For example in terms of TOF the identification of terminal and middle nitrogen ion is clear, the terminal ion must be heading toward the detector at the point of Coulomb explosion and the middle ion must be heading away from the detector, how is it possible then to identify molecules for which the nitrogen ions have switched places in the stepwise channel? In order to investigate this, we divide the plot up into several regions and attempt to visualize the metastable break up processes in the (1, 1, 1) channel, and determine for which orientations they are visible and for which they cause incorrect identification. Figure 5-5 shows a central Dalitz plot of channel (1, 1, 1) for 7fs pulses as before. In order to do this, for each region we show the average TOF spectrum, colored arrows show the TOF window, blue for N_t^+ forward, red for N_m^+ backward, and light brown for O^+ backward. The red dashed vertical lines show the zero TOF (time for an ion with zero initial momentum along with TOF axis) for N^+ (left) and O^+ (right). Furthermore, we chose selected orientations and alignment for each break up process and show a schematic of the molecule at the point of explosion. The momentum figures, Figure 5-5 (a_1)-(f_1) schematically, show all momentum vectors of the three fragment ions for the selected process with its specific orientation and alignment. The arrival times of each ion from the process are superimposed on the average TOF spectrum. For the specific region of the Dalitz plot (Figure 5-5 (a_2)-(f_2)) blue, red, and light brown bars represent flight times of N_t^+, N_m^+, and O_b^+ respectively. When these bars appear in a window (region) designated by the arrows of the same color it indicates a correct identification. When there is a mismatch it indicates an incorrect identification.

5.6.1 Correct identification of the NO^{2+} metastable channel

The red dashed line oval region on the Dalitz plot is depicted schematically in Figures 5-5 (a_1)-(a_2). The stepwise process $NO^{2+} + N_t^+ \rightarrow N_t^+ + N_m^+ + O^+$ is shown for a molecule aligned with the E field of the laser pulse when the metastable NO^{2+} has rotated less than 90 degrees. As Figure 5-5 (a_1)

shows, N_t^+ with a large momentum is directed toward the PSD, causing it to arrive early in the TOF. N_m^+ is directed in the direction of the PSD but because of low momentum toward the PSD, arrives later than N_t^+. O^+ has large momentum and is slightly directed in the opposite direction to the PSD (O^+ backwards). As Figure 5-5 (a_2) shows, the colored bars of the individual arrival times appear in the expected TOF ranges, and represent the ions correctly identified.

The black dashed oval region is depicted schematically in Figures 5-5 (b_1)-(b_2). The stepwise process $NO^{2+} + N_t^+ \rightarrow N_t^+ + N_m^+ + O^+$ is shown for a molecule aligned with the E field of the laser pulse when the metastable NO^{2+} has rotated more than 90 degrees. As Figure 5-5 (b_1) shows, both N_t^+ and N_m^+ have high momentum and O^+ has low momentum. Furthermore, the momentum of N_t^+ is directed toward the PSD, causing it to arrive early in the TOF, while N_m^+ is largely directed in the opposite direction and arrives later. Figure 5-5 (b_2) shows the average flight time for this selected region where the colored bars appear in the correct TOF regions indicate that this channel is visible for vertical alignment even when this NO^{2+} metastable has rotated more than 90 degrees. This is important because for most pulse lengths molecules aligned with the laser polarization are more prevalent.

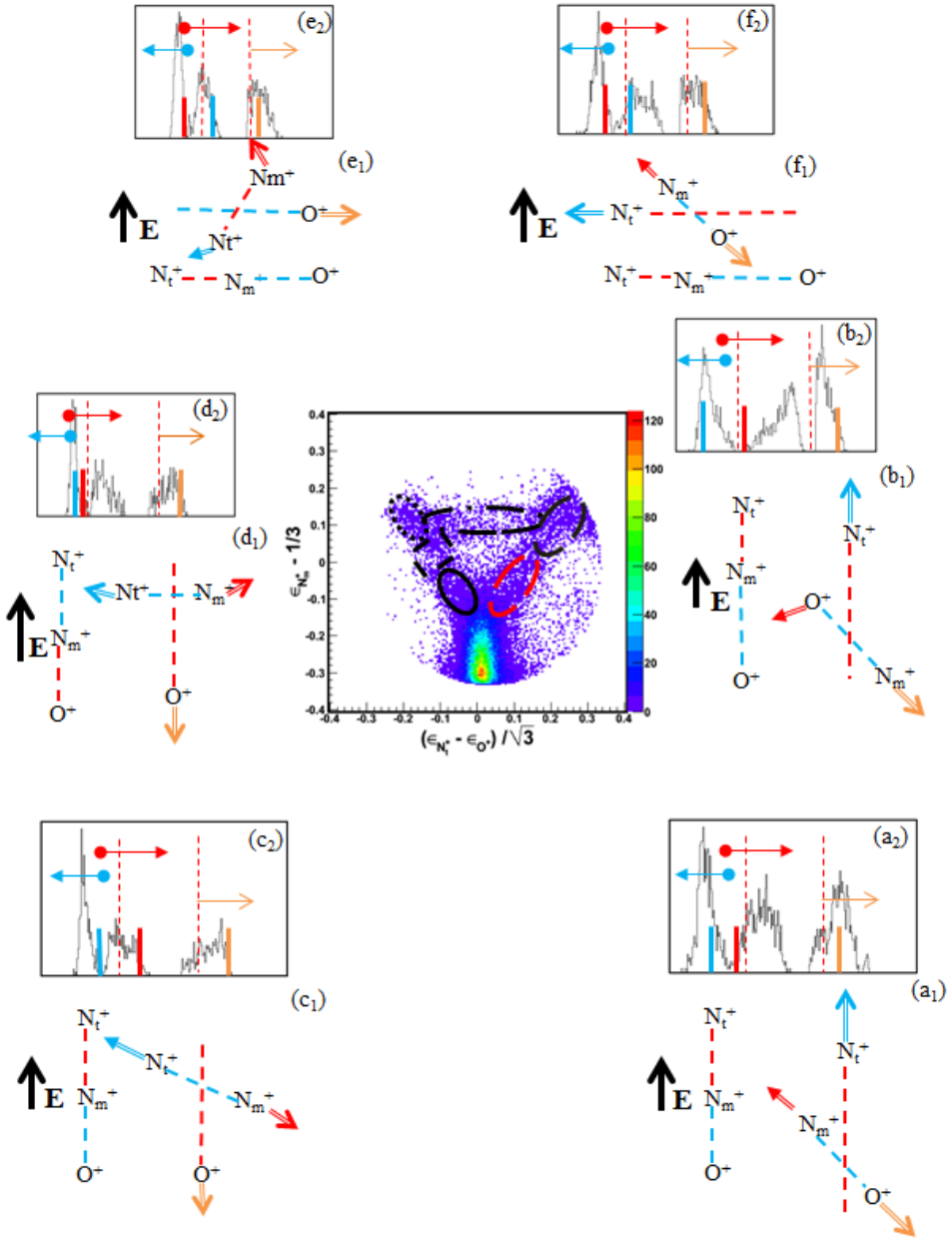

Figure 5-5 Dalitz Plot in the center, momentum vectors of the three fragment ((a_1)-(f_1)), and average TOF spectrum ((a_2)-(f_2)) N_2O (1, 1, 1) channel, colored arrows show the TOF window, the dashed vertical lines show the zero TOF

5.6.2 Correct identification of the stepwise N_2^{2+} (rotation less than 90 degrees)

The black solid oval region of the Dalitz plot is pictured schematically in Figure 5-5 (c_1)-(c_2). The stepwise process $N_2^{2+} + O^+ \rightarrow N_t^+ + N_m^+ + O^+$ is shown for a molecule aligned with the E field of the laser pulse when the metastable N_2^{2+} has rotated less than 90 degrees. As Figure 5-5 (c_1) shows, O^+ has high momentum and is largely directed in the opposite direction of the PSD. Furthermore, N_m^+ is largely directed in the opposite direction and N_t^+ is directed toward the PSD, causing it to arrive early in the TOF than N_m^+ does. Figure 5-5 (c_2) shows that the colored bars of individual ions appearing in the expected TOF ranges indicate that this channel is correctly identified.

The black dashed square region on the Dalitz plot is pictured in Figures 5-5 (d_1)-(d_2). The stepwise process $N_2^{2+} + O^+ \rightarrow N_t^+ + N_m^+ + O^+$ is shown for a molecule aligned with the E field while the metastable N_2^{2+} has rotated almost 90 degrees. As Figure 5-5 (d_1) shows, O^+ is largely directed in the opposite direction to the PSD. While both N_t^+ and N_m^+ have high momentum and fragment nearly horizontally in opposite direction to each other with a small momentum component toward the PSD, As a result, the arrival time of both fragment ions N_t^+ and N_m^+ will be close to the zero TOF for N^+ Figure 5-5 (d_2). This small time difference between the arrivals of both ions causes a detection issue due to the PSD's dead-time. After the first ion arrives, the PSD requires 10 nanoseconds to re-enable detection. Because of this gap, if the arrival time of the second ion is in the dead time range, as in this case, the second ion will not be detected. Lack of statistics in the black square region is a good indicator of this detection problem.

5.6.3 False identification in black dotted region

The black dotted oval region on the Dalitz plot is represented in Figures 5-5 (e_1)-(e_2). The stepwise process $N_2^{2+} + O^+ \rightarrow N_t^+ + N_m^+ + O^+$ is shown for a molecule aligned perpendicularly with the E field. In this region the metastable N_2^{2+} has rotated less than 90 degrees. As Figure 5-5 (e_1) shows, O^+ has high momentum perpendicular to the PSD, causing it to arrive close to the O^+ zero TOF line. Importantly for this geometry N_t^+ fragments away from the detector and N_m^+ fragments toward the detector. The colored bars in Figure 5-5 (e_2) are therefore switched leading to false identification.

The black dash dotted oval region on the Dalitz plot is depicted in Figures 5-5 (f_1)-(f_2) and represents the stepwise process $NO^{2+} + N_t^+ \rightarrow N_t^+ + N_m^+ + O^+$. Here we show a molecule aligned perpendicularly with the E field when the metastable NO^{2+} has rotated less than 90 degrees. As Figure 5-5 (f_1) shows N_t^+ has fragmented close to horizontally, with high momenta and arrival close to the zero TOF for nitrogen. N_m^+, however, fragments with momenta directed towards the PSD, causing it

to arrive much earlier in the TOF than it does in Figure 5-5 (a_1). O^+ fragments backwards in the spectrometer again, arriving late in the TOF. As Figure 5-5 (f_2) shows, the blue color bar appears in the red arrow region, this indicates that this channel is not visible for horizontal alignment when this NO^{2+} metastable has rotated by less than 90 degrees. The fact that N_t^+ appears in the TOF where we expect N_m^+ and vice versa results, in the identities of these ions being switched which is why the events appear in this region as incorrect identifications and not in the expected region.

5.7 Dalitz plots (1, 1, 1) channel as pulse length varied from 7-500fs

Figure 5-6 shows the progression of the (1, 1, 1) channel as the laser pulse length is varied from 7 fs to 500 fs. Firstly from 7 fs to 60 fs there is a clear drop off in both the stepwise channels, and in particular the almost complete disappearance of the channel which proceeds via the metastable N_2^{2+}. This is clear by observing the region around $x = -0.2$, $y = 0.1$ which at 7 fs is rich in data from the N_2^{2+} channel. By 60 fs this region is almost devoid of signal, while the NO^{2+} signal near $x = 0.2$, $y = 0.1$ remains strong. This result is consistent with the result for 60 fs pulse duration is obtained by Yamanouchi group [104].

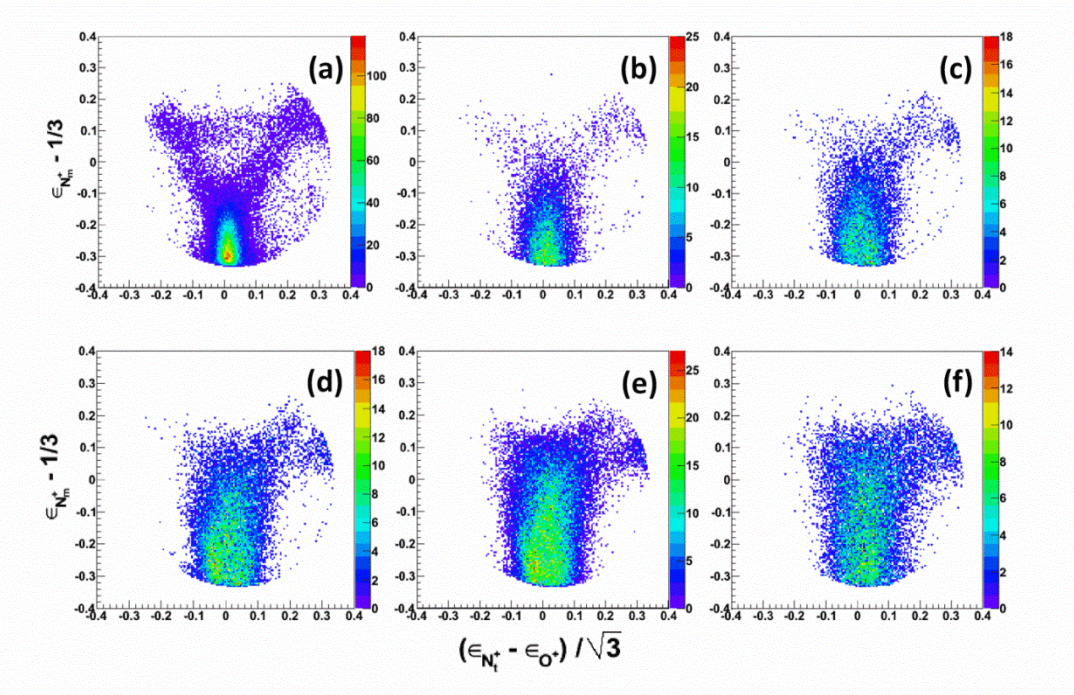

Figure 5-6 Dalitz plots, (a) 7 fs, (b) 30 fs (c) 60 fs (d) 100 fs (e) 200 fs and (f) 500 fs for the (1,1,1) channel (I between 4×10^{15} and 2.5×10^{14} W/cm^2). Noticeable are the near dissapearance of the channel $N_2O^{3+} \rightarrow N_2^{2+} + O^+ \rightarrow N^+ + N^+ + O^+$ above 60 fs and the continuing presence of the $N_2O^{3+} \rightarrow N^+ + NO^{2+} \rightarrow N^+ + N^+ + O^+$ with increasing pulse length

5.7.1 Identification of two stable $N_2^{2+} + O^+$ and $NO^{2+} + N^+$ channel as the pulse length changed 7-500fs

Before we examine the physics behind this phenomenon, we should verify that the drop in signal is not solely due to the inability to distinguish the degenerate nitrogen ions from the stepwise channel for long pulses. In order to do this, we identify two channels which give rise to dications that are stable on the timescale of our detection system, $N_2^{2+} + O^+$ and $NO^{2+} + N^+$, which are not subject to any detection ambiguity. By monitoring the ratio of these two channels as a function of pulse duration, we can see if the decrease in the metastable N_2^{2+} is reflected in the behavior of the stable channel. Figure 5-7 shows that the stable N_2^{2+} channel does indeed display the same dramatic decline as we see in the metastable N_2^{2+} channel, confirming the trend visible in the Dalitz plots.

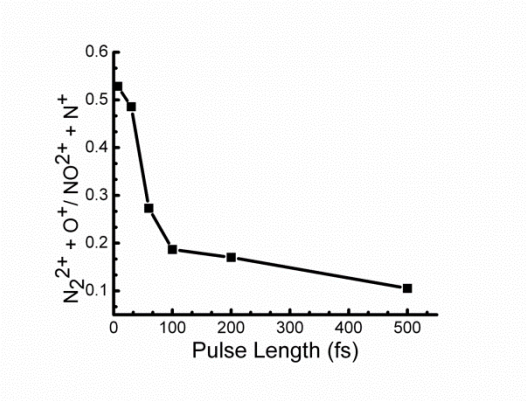

Figure 5-7 Ratio of channel N_2^{2+} + O^+ to NO^{2+} + N^+ as a function of pulse duration from 7 to 500 fs.

The stable N_2^{2+} shows only a small drop from 7 to 30 fs but a dramatic decline between 30 and 60 fs echoing the behavior of the metastable channel which completely disappears above 30 fs. It should be noted though that the stable ion channel does not decline to zero, indicating there is likely some overestimate of the drop in the metastable channel. As can be seen in Figure 5-8 the explanation for the decline in both stable and metastable species of N_2^{2+} seems likely associated with the characteristics of the attractive quasibound $^1\Sigma^+$ state of the molecular dication, which has a depth of 2 eV compared to 3.8 eV for the $^2\Sigma^+$ state of NO^{2+} [104].

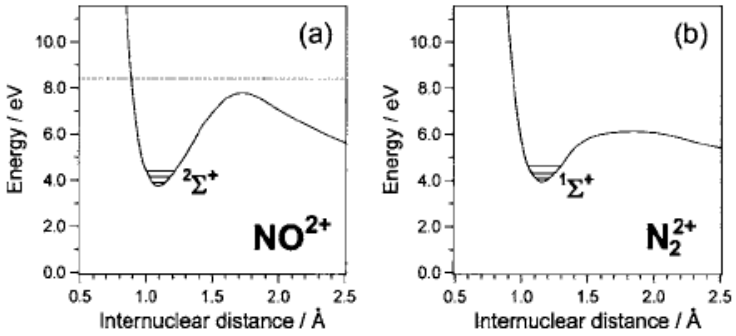

Figure 5-8 (a) Numerical calculation of the potential energy curve of $^2\sum^+$ state of NO^{2+}, (b) The numerical calculation of the potential energy curve of $^1\sum^+$ state of N_2^{2+}, The dotted line corresponds to the internal energy of NO^{2+} produced after the first step of the sequential process (Reprinted with permission from [104])

The barriers of both states are peaked at nuclear separations close to 1.7A. N_2^{2+} may be vulnerable to dissociation for pulses longer than 10 fs, when the high vibrational states of N_2^{2+} can explore longer bound distances where bond softening and enhanced ionization can occur, but there is little reason to suppose that the low vibrational levels which populate the stable N_2^{2+} channel would be affected in the same way. In fact, N_2^{2+} is quite stable against dissociation by very long pulses including picoseconds pulses [53]. To attempt to better understand the origins of the decreasing N_2^{2+} signal, we must consider the dynamics of the molecule as it is represented on the Dalitz plots, and in the KER distributions.

For pulses longer than 60 fs, in addition to the disappearance of the N_2^{2+} branch there is a progressive vertical shift in the plots of Figure 5-6, indicating more bend geometries are developing in the laser field with time. This second phenomenon can be explained by the interaction of the laser field with the precursor states. As with CO_2, bending in the 3+ charge state for longer pulses can be attributed to the wave packet on the 2+ state experiencing a driving force from the laser, along the bending coordinate [26]. The theoretical prediction of this process in CO_2^{6+} also predicted a correlation of the bending process with stretching of the bonds. For N_2O, there has already been an indication that there is a relationship between bending and stretching, but only from measurements at a fixed 60 fs pulse duration [104]. To be able to observe this experimentally we must measure the KER, as stretching is generally associated with a reduction in the energy released from break up through the Coulomb interaction. In order to consider the stretching of the molecule as a function of pulse duration, we need to measure the KER for the 3+ state and the higher ionization channels which we observe.

5.8 KER for the N_2O^{4+}, (2, 1, 1) and (1, 2, 1) channels

To measure the KER for the 4+ molecule, we need to consider the two observed break up channels (2, 1, 1) and (1, 2, 1). For these channels, we are able to use the sensitivity of the Dalitz plot to ion positions within the molecule to help us make channel resolved KER measurements for the first time. There is again an issue of the indistinguishable nature of N_m^+ and N_t^+, and in addition N_m^{2+} and N_t^{2+} are also indistinguishable. This issue meant that previous studies of N_2O could not detect the difference in KER for the (2, 1, 1) and (1, 2, 1) channels [103]. From a purely Coulombic approximation, in which the ions are treated as point like particles at the equilibrium bond lengths, the KER for the (1, 2, 1) channel should be higher than the (2, 1, 1). By turning the degeneracy sensitivity of the Dalitz plot to our advantage, we can confirm this.

Using data from the 7 fs pulses, we start with coincidence data which has a zero momentum sum for N^{2+}, N^{+} and O^{+}. We construct the Dalitz plot from this data in Figure 5-9 (a), assuming that the N^{2+} ion is the terminal ion and the N^{+} is the middle ion. The plot shows three distinct features. Firstly, a central region represents geometries close to equilibrium for the (2, 1, 1) channel; secondly, a diagonal region stretching to the top right represents the stepwise channel $N_2O^{4+} \rightarrow N^{2+} + NO^{2+} \rightarrow N^{2+} + N^{+} + O^{+}$ reported here for the first time, and thirdly, a region on the top left which looks similar to the main concerted region but rotated by 120 degrees. This is a signature that two of the ions have been incorrectly assigned for some of the coincidence events. These are the N_t^{2+} and the N_m^{+} which should be N_m^{2+} and the N_t^{+}. In other words this is a clear signal from channel (1, 2, 1) and the Dalitz plot has lifted the degeneracy which was previously present between the nitrogen ions. It is trivial to generate the correct Dalitz plot for this channel by employing a so-called cut or filter, in which everything above and left of a diagonal line (bottom left to top right) is reclassified in terms of which is the end nitrogen ion, and which is the middle nitrogen ion. We are fortunate that there is no stepwise channel linking the two concerted processes in Figure 5-9 (a) as this would make the designation problematic, but since this would represent a very asymmetric channel N_2^{3+} and O^{+}, it is not surprising that it is absent. Figure 5-9 (b) and (c) show the results of this cut with the ion positions correctly reassigned. The vertical shape of the concerted island representing the (1, 2, 1) channel clearly contrasts with the slanted island for the asymmetric (2, 1, 1) channel.

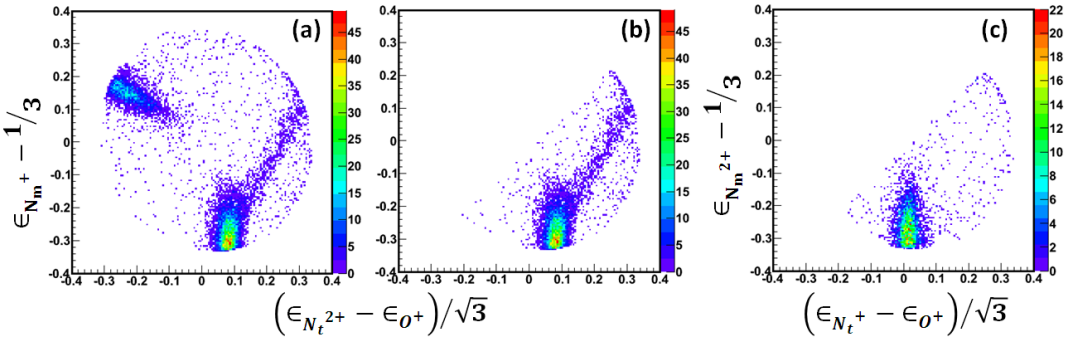

Figure 5-9 (a) Dalitz plot of (2, 1, 1) channel for 7 fs which shows the presence of incorrectly identified coincidences from the (1, 2, 1) channel (top left), (b) cut plot showing only (2 ,1, 1) data and (c) incorrectly identified data from the cut plot, with the designation of the nitrogen ions correctly reasigned, showing the (1, 2, 1) channel.

Figure 5-10 shows the KER distributions for (2, 1, 1) and (1, 2, 1) channels. A broad distribution is visible with a peak at approximately 32.5 eV which is a combination of both channels. Once the cut is made in the Dalitz plot, the KER distributions for the (1, 2, 1) channel and (2, 1, 1) channel can be distinguished as shown in Figure 5-10 in the case of 200 fs pulses.

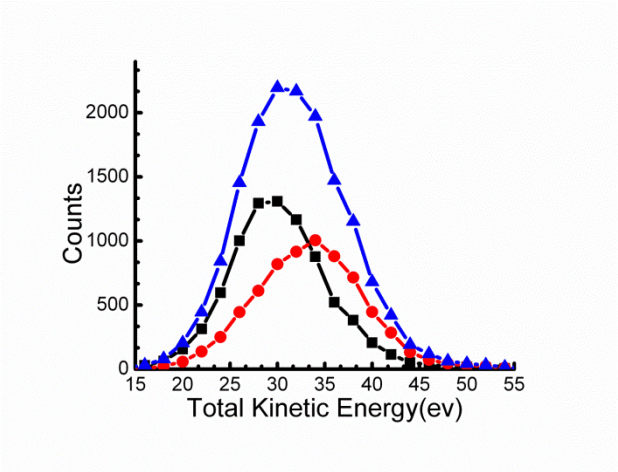

Figure 5-10 KER at 200 fs for the (2, 1, 1) (black squares) and the (1, 2, 1) (red circles) channels. The blue triangles show the combined KER.

The two distributions have different energy peaks, with (2, 1, 1) peaking at 30 eV (CE from equilibrium is 49.53 eV), which is lower than the peak for (1, 2, 1) at 35eV (CE form equilibrium is 56.15 eV). This trend is in agreement with the energies expected from the simple CE picture which treats the ions as point like particles, but both energies are significantly lower than those expected from equilibrium.

5.9 Percentage of Coulombic KER

A convenient way to compare the detected channels with each other on the same graph is to define a ratio of the observed KER to that expected from the idealised CE case from equilibrium, and plot it as a function of pulse duration. From this we can determine the stretching which takes place during the laser pulse. This ratio would be expected to come close to 100% for an ionization processes which happens on a short enough timescale, for which the molecule does not have time to stretch during ionization. This is observed experimentally in the case when highly charged ions are used to initiate ionization [79]. For these interactions the time taken to remove all of the electrons is of the order of a femtosecond and some channels release energy higher than the Coulombic energy. We expect that for

7 fs pulses, the N_2O molecule should stretch very little so that for this pulse length the observed channels should have their highest ratios. For longer pulses, if there is a coupling between bending and stretching as predicted [25] and observed for CO_2, then the KER should decrease due to stretching of the molecular bonds [26], in concert with the bending apparent in the Dalitz plots.

For 7 fs pulses there is insufficient time to stretch significantly, and we can deduce that any channel which has an especially low ratio, has in fact originated from a potential which is significantly non-Coulombic, as is the case for the 3+ state of CO_2 [26]. Furthermore, for CO_2 the energy released for the (1, 1, 1) channel did not decrease significantly with increasing pulse length, but stayed at a level characteristic of the barrier position in the quasibound ground state. Figure 5-11 presents the KER as a percentage of CE versus pulse duration for different final channels. For the (1, 1, 1), (1, 2, 1) and (2, 1, 1) channels we find that at 7 fs, the percentage released is considerably lower than (2, 2, 2), indicating that the potentials is non-Coulombic; furthermore, for the (1, 1, 1) channel the ratio does not decrease until the pulse length is increased beyond 30fs.

We can compare this behavior with that exhibited by CO_2 for this channel [26], also shown in figure 5-11 for comparison. As mentioned above the KER varies little with increasing pulse length. We previously attributed this to the shape of the CO_2^{3+} potential which has a non-Coulombic quasi bound region resembling a saddle point [25]. Asymmetric stretching leads to lower energy on either side of the saddle point, but concerted bond stretching encounters a shallow minimum followed by a maximum before becoming Coulombic at long distance. This leads to energy release characteristic of the potential maximum and independent of the bond length when the dissociative wave packet is deposited on the 3+ potential. For N_2O this phenomenon seems to occur up to 30 fs, indicating that although the 3+ potential has a barrier, it is closer to equilibrium than for CO_2, as characterized by the higher percentage KER for 7 fs (77% compared to 70% for CO_2). For pulses longer than 30 fs the energy decreases significantly, implying that expansion of bonds during the 1+ and 2+ states is sufficient on timescales longer than 30 fs to overcome this barrier. For CO_2 this is not the case as the energy release from the 3+ channel is quite independent of pulse duration, indicating that the molecule stretches less on lower charge states than N_2O for long pulses. This means that for N_2O, at pulses of 60 fs and longer, the 3+ dissociation channels (concerted and stepwise) are all starting from a position of stretched bond length and decreased bend angle. Such behavior is consistent with the theoretical predictions [25] for CO_2 in which coupling between the laser and the 2+ ion gives rise to concerted stretching of the bonds along with bending. This gives us a clue as to the true nature of the change in abundance, with pulse length, of the stepwise channels of N_2O^{3+}. The reduction in N_2^{2+}

channels for pulses of 60 fs and longer is a result of the inhibition of asymmetric stretching due to the expansion of the bonds of N_2O along the concerted coordinate. The shallower form of the asymptotic N_2^{2+} potential is still significant however. When both bonds are expanding and the nuclear wave packet has enough momentum along the concerted bond expansion coordinate to overcome the local maximum, some amplitude still leaks down the steeper NO^{2+} side of the saddle point potential, but little follows the shallower N_2^{2+} side. The decreasing energy behavior of the (1, 1, 1) channel indicates that the molecule reaches a region in which the potential is Coulombic along the concerted coordinate after 30 fs, in agreement with the disappearance of the N_2^{2+} metastable channel and the dramatic drop in the stable N_2^{2+} channel.

For CO_2 we showed that CREI was possible from the 3+ state and concluded that due to the lack of stretching below 3+, CREI was not possible from lower charge states. The current observation of the decrease in energy for the N_2O (1, 1, 1) channel for longer pulses implies that significant motion is possible on the 1+ and 2+ states for CREI to occur between 2+ and 3+. In order to deduce the relative importance of CREI for this step compared to higher steps, we need to look at the pattern of percentage CE for the higher channels. Firstly, for the shortest pulses the highest channel observed (2, 2, 2) is close to Coulombic (87%) as observed for other triatomic molecules [26], [64], [74] making it a good candidate for imaging the equilibrium molecular structure.

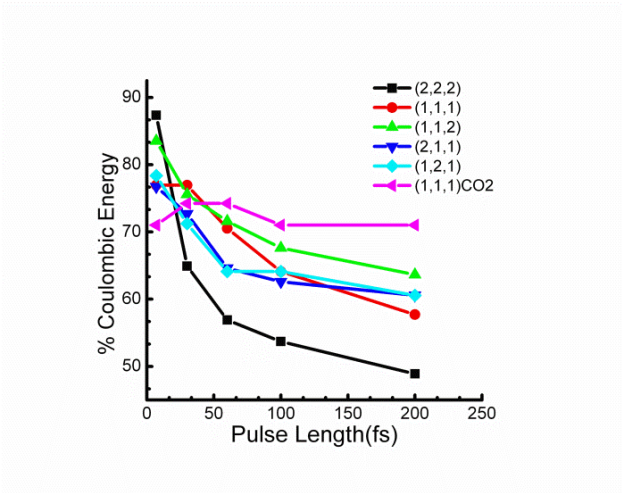

Figure 5-11 Energy released as a percentage of that expected from Coulomb explosion (CE) at the equilibrium geometry of N_2O as a function of the final charge states and pulse duration, with the (1, 1, 1) channel of CO_2 for comparison

For all higher channels the decrease in percentage CE becomes less as the pulse duration increases, indicating that CREI is taking place and that the final ionization step is occurring closer to a "critical distance". For (1, 1, 1) however, when pulses are longer than 35 fs, the slope of the decrease is more pronounced than all other channels, indicating that although bond expansion is significant on the 1+ and 2+ charge states, CREI to the 3+ state is weaker than for higher channels.

5.10 Conclusion

By using the FEMPULS technique in conjunction with the Dalitz plotting method, we have been able to reveal new aspects of the dissociative ionization dynamics of N_2O in intense femtosecond laser pulses. A new stepwise channel has been revealed for the 3+ state which involves a metastable N_2^{2+} intermediate, and a stepwise channel for the 4+ state has also been observed for the first time. In addition, we have been able to deduce the short range dynamics which lead to the changing production of stable and metastable N_2^{2+} fragments with laser pulse length. In terms of CREI we have been able to show that unlike the CO_2 case, the molecule can stretch significantly on the 1+ and 2+ states, but that CREI is not as significant below the 3+ state, indicating that this is still an important doorway state to higher ionization.

Chapter 6
Conclusions and future work

6.1 Summary

In conclusion, by using the FEMPULS technique, KER measurement, in conjunction with the Dalitz and Newton plotting method, we have been able to reveal new aspects of the dissociation and ionization dynamics of CO_2 and N_2O in an intense femtosecond laser pulse. We have made the first clear systematic measurements and provided interpretation of the effect of laser pulse duration on dissociation and ionization to high charge states for a polyatomic molecule, CO_2 and N_2O. In the case of CO_2 by changing the pulse duration, we have been able to definitively measure the molecular geometry where CREI occurs ($R_{CO} \approx 2.1$ Å and $\theta_{OCO} \approx 163^o$). The experimental results clearly indicate the importance of dissociation dynamics on the CO_2^{3+} charge state leading to structural deformation observed in the higher charge states. As the CO_2^{3+} breaks apart, the numerical simulations clearly show that the ionization rate increases rapidly when the molecule is aligned along the laser polarization axis because of strongly coupled CR states ($3\sigma_u \rightarrow 5\sigma_g$). This requires that enough time is given to CO_2^{3+} and subsequent charge states to stretch up to the critical distance of $R_{CO} \sim 2.1$ Å, a condition satisfied with laser pulse duration equal to or longer than 100 fs.
In the case of N_2O also, a new stepwise channel has been revealed for the 3+ state which involves a metastable N_2^{2+} intermediate, and a stepwise channel for the 4+ state has also been observed for the first time. In addition, we have been able to deduce the short range dynamics which lead to the changing production of stable and metastable N_2^{2+} fragments with laser pulse length. In terms of CREI we have been able to show that unlike the CO_2 case, the molecule can stretch significantly on the 1+ and 2+ states, but that CREI is not as significant below the 3+ state, indicating that this is still an important doorway state to higher ionization.

6.2 Future Work

In this work, firstly we have compared our experimental work with calculations of the ionization rate of CO_2^{3+} as a function of R_{CO} and found that the electronic charge resonance is the physics behind enhanced ionization to calculate. The same technique using nonlinear non-perturbative TDDFT and incorporating the Statistical average of orbital potential (SAOP) local density potential can be implemented for the N_2O molecule to understand the physics of CREI. Secondly, the results of our study led to reconstruction of the geometry of CO_2 molecule. This could be a potential subject of

research to describe and reconstruct the geometry of N_2O molecule. This is a non-trivial step requiring careful rewriting of the geometry reconstruction code. Thirdly, pump-probe techniques can be utilized to achieve higher precision in description of the molecules' structure, dynamics, and ionization of disconsolation. Finally, the research group at university of Waterloo has used HCI impact technique for characterization of molecular structure, dynamics, and dissociation mechanism of N_2O, CO_2, and OCS with collaboration with TMU group in Tokyo, Japan. Data analysis and interpretation of this work can be compared with the results presented in this thesis. In order to add to the comparisons already discussed here this can provide precious information on the applicability of each method for specific molecular characterizations.

Bibliography

[1] G. Herzberg, *Molecular Spectra and Molecular Structure: Spectra of Diatomic Molecules.*, Second edi. Krieger Publishing, 1989.

[2] G Herzberg, *Molecular Spectra and Molecular Structure: Infrared and Raman Spectra of Polyatomic Molecules*. Krieger Publishing, 1991.

[3] G. Herzberg, *Molecular Spectra and Molecular Structure: Electronic Spectra and Electronic Structure of Polyatomic Molecules.*, Second edi. Krieger Publishing, 1991.

[4] D. Strickland and G. Mourou, "Compression of amplified chirped optical pulses," *Optics Communications*, vol. 56, no. 3, pp. 219–221, 1985.

[5] D. Gemmell, J. Remillieux, J. Poizat, M. Gaillard, R. Holland, and Z. Vager, "Evidence for an Alignment Effect in the Motion of Swift Ion Clusters through Solids," *Phys. Rev. Lett.*, vol. 34, no. 23, pp. 1420–1424, 1975.

[6] Z. Vager, D. Gemmell, and B. Zabransky, "Dissociation of fast HeH+ iona traversing thin foils," vol. 14, no. 2, pp. 638–641, 1976.

[7] W. Pietsch, D. Gemmell, P. Cooney, E. Kanter, D. Kurath, A. Ratkowski, Z. Vager, and B. Zabransky, "The transmission of fast molecular ions through thin foils," *Nuclear Instruments and Methods*, vol. 170, pp. 61–66, 1980.

[8] Z. Vager, R. Naaman, and E. Kanter, "Coulomb explosion imaging of small molecules," *Science (New York, N.Y.)*, vol. 244, no. 4903, pp. 426–431, Apr. 1989.

[9] J. Levin, H. Feldman, A. Baer, D. Ben-Hamu, O. Heber, D. Zajfman, and Z. Vager, "Study of Unimolecular Reactions by Coulomb Explosion Imaging: The Nondecaying Vinylidene," *Physical Review Letters*, vol. 81, no. 16, pp. 3347–3350, Oct. 1998.

[10] H. Kreckel, S. Krohn, L. Lammich, M. Lange, J. Levin, M. Scheffel, D. Schwalm, J. Tennyson, Z. Vager, R. Wester, A. Wolf, and D. Zajfman, "Vibrational and rotational cooling of H3+," *Physical Review A*, vol. 66, no. 5, p. 052509, Nov. 2002.

[11] U. Werner, B. Siegmann, H. Lebius, B. Huber, and H. Lutz, "Multiple ionization and fragmentation of CH4 in collisions with slow highly charged ions," *Nuclear Instruments and Methods in Physics Research Section B: Beam Interactions with Materials and Atoms*, vol. 205, pp. 639–642, May 2003.

[12] J. Becker, K. Beckord, U. Werner, and H. Lutz, "A system for correlated fragment detection in dissociation experiments," *Nuclear Instruments and Methods in Physics Research Section A: Accelerators, Spectrometers, Detectors and Associated Equipment*, vol. 337, no. 2–3, pp. 409–415, Jan. 1994.

[13] U. Werner, J. Becker, T. Farr, and H. Lutz, "How molecules and clusters explode," *Nuclear Instruments and Methods in Physics Research Section B: Beam Interactions with Materials and Atoms*, vol. 124, no. 2–3, pp. 298–302, Apr. 1997.

[14] A. Reinköster, B. Siegmann, U. Werner, B. AHuber, and H. Lutz, "Multi-fragmentation of C60 after collisions with Arz+ ions," *Journal of Pysics B: Atomic, Molecular and Optical Physics*, vol. 35, no. 02, pp. 4989–4997, 2002.

[15] B. Siegmann, U. Werner, H. O. Lutz, and R. Mann, "Complete Coulomb fragmentation of CO2 in collisions with 5.9 MeV u−1 Xe18+ and Xe43+," *J. Phys B: At. Mol. Opt. Phys.*, vol. 35, no. 02, pp. 3755–3765, 2002.

[16] U. Werner, K. Beckord, J. Becker, H. O. Folkerts, and H. O. Lutz, "Ion-impact-induced fragmentation of water molecules," *Nuclear Instruments and Methods in Physics Research Section B: Beam Interactions with Materials and Atoms*, vol. 98, no. 1–4, pp. 385–388, May 1995.

[17] J. Sanderson, T. Nishide, H. Shiromaru, Y. Achiba, and N. Kobayashi, "Near-Coulombic behavior in the dissociative ionization of CO2 due to impact by Ar8+," *Physical Review A*, vol. 59, no. 6, pp. 4817–4820, 1999.

[18] N. Neumann, D. Hant, Lp. Schmidt, J. Titze, T. Jahnke, A. Czasch, M. S. Schöffler, K. Kreidi, O. Jagutzki, H. Schmidt-Böcking, and R. Dörner, "Fragmentation Dynamics of CO23+ Investigated by Multiple Electron Capture in Collisions with Slow Highly Charged Ions," *Physical Review Letters*, vol. 104, no. 10, p. 103201, Mar. 2010.

[19] J. Posthumus, L. Frasinski, A. J. Giles, and K. Codling, "Dissociative ionization of molecules in intense laser fields: a method of predicting ion kinetic energies and appearance intensities," *Journal of Physics B: Atomic, Molecular and Optical Physics*, vol. 28, pp. L349–L353, 1995.

[20] L. Frasinski, K. Codling, and P. Hatherly, "Covariance mapping: A correlation method applied to multiphoton multiple ionization," *Science*, vol. 246, no. 4933, pp. 1029–1031, 1989.

[21] C. Cornaggia, "Large-amplitude nuclear motions in the laser-induced Coulomb explosion of carbon dioxide molecules," *Physical review. A*, vol. 54, no. 4, pp. R2555–R2558, Oct. 1996.

[22] A. Hishikawa, H. Hasegawa, and K. Yamanouchi, "Sequential three-body Coulomb explosion of CS2 in intense laser fields appearing in momentum correlation map," *Chemical physics letters*, vol. 361, no. July, pp. 245–250, 2002.

[23] F. Légaré, K. F. Lee, I. V. Litvinyuk, P. W. Dooley, S. S. Wesolowski, P. R. Bunker, P. Dombi, F. Krausz, A. D. Bandrauk, D. M. Villeneuve, and P. B. Corkum, "Laser Coulomb-explosion imaging of small molecules," *Physical Review A*, vol. 71, p. 013415, Jan. 2005.

[24] A. Matsuda, E. J. Takahashi, and A. Hishikawa, "Dalitz plot analysis of Coulomb exploding O3 in ultrashort intense laser fields.," *The Journal of chemical physics*, vol. 127, no. 11, p. 114318, Sep. 2007.

[25] Y. Sato, H. Kono, S. Koseki, and Y. Fujimura, “Description of molecular dynamics in intense laser fields by the time-dependent adiabatic state approach: application to simultaneous two-bond dissociation of CO2 and its control,” *Journal of the American Chemical Society*, vol. 125, no. 26, pp. 8019–831, Jul. 2003.

[26] I. Bocharova, R. Karimi, E. F. Penka, J. P. Brichta, P. Lassonde, X. Fu, J. C. Kieffer, A. D. Bandrauk, I. Litvinyuk, J. H. Sanderson, and F. Légaré, “Charge Resonance Enhanced Ionization of CO2 Probed by Laser Coulomb Explosion Imaging,” *Physical Review Letters*, vol. 107, no. 6, p. 063201, Aug. 2011.

[27] J. Ullrich, R. Moshammer, R. Dörner, O. Jagutzki, V. Mergel, H. Schmidt-Böcking, and L. Spielberger, “Recoil-ion momentum spectroscopy,” *Journal of Physics B: Atomic, Molecular and Optical Physics*, vol. 30, no. 13, pp. 2917–2974, Jul. 1997.

[28] B. Siegmann, U. Werner, H. Lutz, and R. Mann, “Multiple ionization and fragmentation of H2O in collisions with fast highly charged Xe ions,” *Journal of Physics B:Atomic Molecular and Optical Physics*, vol. 34, pp. L587–L593, 2001.

[29] W. C. Wiley and I. H. McLaren, “Time-of-Flight Mass Spectrometer with Improved Resolution,” *The Review of Scientific Instruments*, vol. 26, no. 12, p. 1150, 1955.

[30] T. Mizogawa, H. Shiromaru, M. Sato, and Y. Ito, “A two-dimensional position-sensitive ion detector based on modified backgammon method with weighted-coupling capacitors,” *International Journal of Mass Spectrometry*, vol. 215, no. 1–3, pp. 141–149, Apr. 2002.

[31] H. Werner and P. Knowles, “A second order multiconfiguration SCF procedure with optimum convergence,” *The Journal of Chemical Physics*, vol. 82, no. 11, p. 5053, 1985.

[32] U. Brinkmann, A. Reinkoster, B. Siegmann, U. Werner, H. Lutz, and R. Mann, “Ion-impact induced multiple ionization and fragmentation of N2,” *Physica Scripta*, vol. T80B, no. 10.1238, pp. 171–172, 1999.

[33] L. Adoui, M. Tarisien, J. Rangama, P. Sobocinsky, A. Cassimi, J. Chesnel, F. Fremont, B. Gervais, A. Dubois, M. Krishnamurthy, S. Kumar, and D. Mathur, “HCI-Induced Molecule Fragmentation: non-Coulombic Explosion and Three-Body Effects,” *Physica Scripta*, vol. T92, no. 1, pp. 89–95, 2001.

[34] T. Mizogawa, Y. Awaya, Y. Isozumi, R. Katano, S. Ito, and N. Maeda, “New readout technique for two-dimensional position-sensitive detectors,” *Nuclear Instruments and Methods in Physics Research*, vol. A312, pp. 547–552, 1992.

[35] H. Shiromaru, T. Nishide, J. Sanderson, Y. Achiba, and N. Kobayashi, “Dissociation scheme of highly charged triatomic molecules,” *Physica Scripta*, vol. T80, pp. 110–113, 1999.

[36] M. T. Muranaka, “Dynamique de la fragmentation de molécules tri-atomiques: contribution de la géométrie Membres,” Universite de Caen/Basse-Normandie, 2006.

[37] B. Wales, T. Motojima, J. Matsumoto, Z. Long, W. K. Liu, H. Shiromaru, and J. H. Sanderson, "Multiple ionization and complete fragmentation of OCS by impact with highly charged ions Ar4+ and Ar8+ at 15 keV q−1," *Journal of Physics B: Atomic, Molecular and Optical Physics*, vol. 45, no. 4, p. 045205, Feb. 2012.

[38] K. Yamakawa, C. Barty, H. Shiraga, and Y. Kato, "Generation of a High-Energy Picosecond Laser Pulse with a High-Contrasr Ratio by Chireped-Pulse Amplification," *IEEE Jornal of Quantum Electronics*, vol. 27, no. 2, pp. 288–294, 1991.

[39] J. Squier, F. Salin, G. Mourou, and D. Harter, "100-fs pulse generation and amplification in Ti:Al2O3.," *Optics letters*, vol. 16, no. 5, pp. 324–6, Mar. 1991.

[40] T. Brabec and F. Krausz, "Intense few-cycle laser fields: Frontiers of nonlinear optics," *Reviews of Modern Physics*, vol. 72, no. 2, pp. 545–591, Apr. 2000.

[41] B. Bransden and C. Joachain., *Physics of atoms and molecules*. 2003.

[42] L. Keldysh, "Ionization in the field of a strong electromagnetic wave," *Soviet Physics JETP*, vol. 20, no. 5, pp. 1307–1314, 1965.

[43] M. Wegener, "Extreme nonlinear optics," in *NATO-Advanced-Study-Institute on Frontiers of Optical Spectroscopy*, 2005, pp. 93–186.

[44] K. Codling and L. Frasinski, "Dissociative ionization of small molecules in intense laser fields," *J. Phys. B At. Mol. Opt. Phys.*, vol. 26, no. 5, pp. 783–809, 1993.

[45] C. Cornaggia, J. Lavancier, D. Normand, J. Morellec, and P. Agostini, "Multielectron dissociative ionization of diatomic molecules in an intense femtosecond laser field," *Physical Review A*, vol. 44, no. 7, pp. 4499–4505, 1991.

[46] J. Posthumus, K. Codling, L. Frasinski, and M. Thompson, "The Field-Ionization, Coulomb Explosion of Diatomic Molecules in Intense Laser Fields," *Laser Physics*, vol. 7, no. 3, pp. 813–825, 1997.

[47] C. Cornaggia, M. Schmidt, and D. Normand, "Coulomb explosion of CO2 in an intense femtosecond laser field," *J. Phys, B: At. Mol. Opt. Phys.*, vol. 27, pp. L123–L130, 1994.

[48] T. Seideman, M. Ivanov, and P. Corkum, "The use of intense-field ionization in time-resolved measurements," *Chemical Physics Letters*, vol. 252, no. 3–4, pp. 181–188, Apr. 1996.

[49] T. Seideman, M. Y. Ivanov, and P. B. Corkum, "Role of Electron Localization in Intense-Field Molecular Ionization," *Physical Review Letters*, vol. 75, no. 15, pp. 2819–2822, Oct. 1995.

[50] T. Zuo and A. D. Bandrauk, "Charge-resonance-enhanced ionization of diatomic molecular ions by intense lasers," *Physical Review A*, vol. 52, no. 4, pp. R2511–R2514, 1995.

[51] K. Codling, L. Frasinski, and P. Hatherly, “Multiphoton ionisation of H2 and D2 using an intense sub-picosecond laser,” *J. Phys. B: At. Mol. Opt. Phys.*, vol. 21, pp. L433–L438, 1988.

[52] K. Codling, L. Frasinski, and P. Hatherly, “Multiphoton Ionization of H2 and D2 Using an Intense Subpicosecond Laser,” *J. Phys. B: At. Mol and Opt. Phys.*, vol. 20, no. 15, pp. L433–L438, 1987.

[53] L. J. Frasinski, K. Codling, P. Hatherly, J. Barr, I. N. Ross, and W. T. Toner, “Femtosecond Fynamics of Multielectron Dissociative Ionization by Use of a Picosecond Laser,” *Physical review Letters*, vol. 58, no. 23, pp. 2424–2427, 1987.

[54] L. Quaglia and C. Cornaggia, “Experimental evidence of excited multicharged atomic fragments coming from laser-induced coulomb explosion of molecules,” *Physical review letters*, vol. 84, no. 20, pp. 4565–4568, May 2000.

[55] A. Bandrauk and J. Ruel, “Charge-resonance-enhanced ionization of molecular ions in intense laser pulses: Geometric and orientation effects,” *Physical Review A*, vol. 59, no. 3, pp. 2153–2162, 1999.

[56] A. Hishikawa, A. Iwamae, and K. Yamanouchi, “Ultrafast Deformation of the Geometrical Structure of CO2 Induced in Intense Laser Fields,” *Physical Review Letters*, vol. 83, no. 6, pp. 1127–1130, Aug. 1999.

[57] C. Cornaggia, “Role of the molecular electronic configuration in the Coulomb fragmentation of N2, C2H2 and C2H4 in an intense laser field,” *J. Phys. B: At. Mol . Ot. Phys.*, vol. 25, pp. L415–L422, 1992.

[58] A. Hishikawa, A. Iwamae, K. Hoshina, M. Kono, and K. Yamanouchi, “Mass-resolved two-dimensional momentum imaging of the Coulomb explosion of N2 and SO2 in an intense laser field,” *Chemical physics Ltters*, vol. 282, pp. 283–291, 1998.

[59] J. Sanderson, A. El-Zein, W. Bryan, W. Newell, A. Langley, and P. Taday, “Geometry modifications and alignment of H2O in an intense femtosecond laser pulse,” *Physical Review A*, vol. 59, no. 4, pp. R2567–R2570, Apr. 1999.

[60] C. Cornaggia, M. Schmidt, and D. Normand, “Laser-induced nuclear motions in the Coulomb explosion of C2H2+ ions,” *Physical Review A*, vol. 51, no. 2, pp. 1431–1437, 1995.

[61] P. Hering and C. Cornaggia, “Production of multicharged atomic ions from laser-induced multiple ionization of small molecules,” *Physical Review A*, vol. 57, no. 6, pp. 4572–4580, Jun. 1998.

[62] A. Hishikawa, A. Iwamae, K. Hoshina, M. Kono, and K. Yamanouchi, “Coulomb explosion dynamics of N2 in intense laser field by mass-resolved momentum imaging,” *Chemical Physics*, vol. 231, pp. 315–329, 1998.

[63] A. Hishikawa, A. Iwamae, and K. Yamanouchi, "Ultrafast Deformation of the Geometrical Structure of CO2 Induced in Intense Laser Fields," *Physical Review Letters*, vol. 83, no. 6, pp. 1127–1130, Aug. 1999.

[64] H. Hasegawa, A. Hishikawa, and K. Yamanouchi, "Coincidence Imaging of Coulomb Explosion of CS2 in Intense Laser Fields," *Chemical Physics Letters*, vol. 349, no. 23, pp. 57–63, 2001.

[65] A. Iwasaki, A. Hishikawa, and K. Yamanouchi, "Real-time probing of alignment and structural deformation of CS2 in intense nanosecond laser fields," *Chemical physics letters*, vol. 346, pp. 379–386, 2001.

[66] F. Légaré, I. V Litvinyuk, P. W. Dooley, F. Quéré, A. D. Bandrauk, D. M. Villeneuve, and P. B. Corkum, "Time-Resolved Double Ionization with Few Cycle Laser Pulses," *Physical Review Letters*, vol. 91, no. 9, p. 093002, Aug. 2003.

[67] P. Dooley, I. Litvinyuk, K. Lee, D. Rayner, M. Spanner, D. Villeneuve, and P. Corkum, "Direct imaging of rotational wave-packet dynamics of diatomic molecules," *Physical Review A*, vol. 68, no. 2, p. 023406, Aug. 2003.

[68] A. Hishikawa, E. J. Takahashi, and A. Matsuda, "Electronic and Nuclear Responses of Fixed-in-Space H2S to Ultrashort Intense Laser Fields," *Physical Review Letters*, vol. 97, no. 24, p. 243002, Dec. 2006.

[69] M. W. Schmidt, K. K. Baldridge, J. A. Boatz, S. T. Elbert, M. A. Gordon, J. H. Jensen, S. Koseki, N. Matsunaga, K. A. Nguyen, S. Su, T. L. Windus, M. Dupuis, and J. A. Montgomery, "General atomic and molecular electronic structure system," *Journal of of Computational Chemistry*, vol. 14, no. 11, pp. 1347–1363, 1993.

[70] J. P. Brichta, S. J. Walker, R. Helsten, and J. H. Sanderson, "Ultrafast imaging of multielectronic dissociative ionization of CO2 in an intense laser field," *J. Phys. B: At. Mol. and Opt. Phys.*, vol. 40, no. 1, pp. 117–129, Jan. 2007.

[71] R. Allemand and G. Thomas, "Nouveau Detecteur de Localisation," *Nuclear Instruments and Methods*, vol. 137, pp. 141–149, 1976.

[72] W. A. Bryan, J. H. Sanderson, A. El-Zein, W. R. Newell, P. F. Taday, and A. J. Langley, "Laser-induced Coulomb explosion, geometry modification and reorientation of carbon dioxide," *J. Phys. B: AtoM. Mol. Opt. Phys.*, vol. 33, no. 4, pp. 745–766, Feb. 2000.

[73] F. Légaré, K. F. Lee, A. D. Bandrauk, D. M. Villeneuve, and P. B. Corkum, "Laser Coulomb explosion imaging for probing ultra-fast molecular dynamics," *J. Phys B: Atom. Mol. Opt. Phys.*, vol. 39, no. 13, pp. S503–S513, Jul. 2006.

[74] F. Légaré, K. F. Lee, I. V Litvinyuk, P. W. Dooley, A. D. Bandrauk, D. M. Villeneuve, and P. B. Corkum, "Imaging the time-dependent structure of a molecule as it undergoes dynamics," *Physical Review A*, vol. 72, no. 5, p. 052717, Nov. 2005.

[75] A. Siegman, *Lasers*. 1995.

[76] J. T. Verdeyen, *Laser Electronics*. 2000.

[77] X. M. Tong, Z. X. Zhao, and C. D. Lin, "Probing Molecular Dynamics at Attosecond Resolution with Femtosecond Laser Pulses," *Physical Review Letters*, vol. 91, no. 23, p. 233203, Dec. 2003.

[78] P. W. Dooley, "Molecular Imaging Using Femtosecond Laser Pulses," McMaster University, Hamilton, Ontario, Canada, 2003.

[79] B. Wales, E. Bisson, R. Karimi, J. C. Kieffer, F. Légaré, and J. H. Sanderson, "A coincidence detection algorithm for improving detection rates in coulomb explosion imaging," *Nuclear Instruments and Methods in Physics Research A: Accelerators, Spectrometers, Detectors and Associated Equipment*, vol. 667, pp. 11–15, Mar. 2012.

[80] H. Gmbh, "MCP Delay Line Detector Manual RoentDek Handels GmbH." pp. 1–96.

[81] I. A. Bocharova, "Laser Coulomb Explosion Imaging of Molecular Dynamics," Kansas State University, Manhattan, Kansas, 2009.

[82] Developed at Cearn, "Root Softwer," *Cearn*, 2010. .

[83] B. Wales, "Improvements to detection efficiency and measurement accuracy in Coulomb Explosion Imaging experiments," Waterloo University, 2012.

[84] J. Itatani, J. Levesque, D. Zeidler, H. Niikura, H. Pépin, J. C. Kieffer, P. B. Corkum, and D. M. Villeneuve, "Tomographic imaging of molecular orbitals.," *Nature*, vol. 432, no. 7019, pp. 867–71, Dec. 2004.

[85] T. Zuo, A. Bandrauk, and P. Corkum, "Laser-induced electron diffraction: a new tool for probing ultrafast molecular dynamics," *Chemical physics letters*, vol. 259, pp. 313–320, 1996.

[86] M. Meckel, D. Comtois, D. Zeidler, a Staudte, D. Pavicic, H. C. Bandulet, H. Pépin, J. C. Kieffer, R. Dörner, D. M. Villeneuve, and P. B. Corkum, "Laser-induced electron tunneling and diffraction.," *Science (New York, N.Y.)*, vol. 320, no. 5882, pp. 1478–82, Jul. 2008.

[87] A. Hishikawa, A. Matsuda, M. Fushitani, and E. Takahashi, "Visualizing Recurrently Migrating Hydrogen in Acetylene Dication by Intense Ultrashort Laser Pulses," *Physical Review Letters*, vol. 99, no. 25, p. 258302, Dec. 2007.

[88] C. Cornaggia, "Ultrafast Coulomb explosion imaging of molecules," *Laser Physics*, vol. 19, no. 8, pp. 1660–1670, Jul. 2009.

[89] M. Schmidt, D. Normand, and C. Cornaggia, "Laser-induced trapping of chlorine molecules with pico-and femtosecond pulses," *Physical Review A*, vol. 50, no. 6, pp. 5037–5045, 1994.

[90] C. Siedschlag and J. Rost, “Enhanced ionization in small rare-gas clusters,” *Physical Review A*, vol. 67, no. 1, p. 013404, Jan. 2003.

[91] S. Chelkowski and a D. Bandrauk, “Two-step Coulomb explosions of diatoms in intense laser fields,” *Journal of Physics B: At. Mol. Opt. Phys.*, vol. 28, no. 23, pp. L723–L731, Dec. 1995.

[92] A. Staudte, D. Pavičić, S. Chelkowski, D. Zeidler, M. Meckel, H. Niikura, M. Schöffler, S. Schössler, B. Ulrich, P. . Rajeev, T. Weber, T. Jahnke, D. M. Villeneuve, A. D. Bandrauk, C. L. Cocke, P. B. Corkum, and R. Dörner, “Attosecond Strobing of Two-Surface Population Dynamics in Dissociating H2+,” *Physical Review Letters*, vol. 98, no. 7, p. 073003, Feb. 2007.

[93] L. Frasinski and P. Hatherly, “Multielectron dissociative ionization of CO2 in intense laser fields,” *Journal of Physics B: At. Mol. Opt. Phys.*, vol. 27, pp. L109–L114, 1994.

[94] S. V Menon, J. P. Nibarger, and G. N. Gibson, “A framework for understanding molecular ionization in strong laser fields,” *J. Phys B: At. Mol. Opt. Phys.*, vol. 35, no. 02, pp. 2961–2974, 2002.

[95] B. Wales, R. Karimi, E. Bisson, B. S. MGiguère, T. Motojima, and R. Anderson, “Comparing coulomb explosion dynamics of multiply charged triatomic molecules after ionization by highly charged ion impact and few cycle femtosecond laser pulses,” *Physica Scripta*, no. Pending publication Augest 2013.

[96] R. Dalitz, “CXII. On the analysis of τ-meson data and the nature of the τ-meson,” *Philosophical Magazine*, vol. 44, pp. 1068–1080, 1953.

[97] J. P. Brichta, A. N. Seaman, and J. H. Sanderson, “Ultrafast imaging of polyatomic molecules with simplex algorithm,” *Computer Physics Communications*, vol. 180, no. 2, pp. 197–200, Feb. 2009.

[98] O. V Gritsenko, P. R. T. Schipper, and E. J. Baerends, “Approximation of the exchange-correlation Kohn–Sham potential with a statistical average of different orbital model potentials,” *Chemical physics letters*, vol. 302, pp. 199–207, 1999.

[99] E. P. Fowe and A. D. Bandrauk, “Nonlinear time-dependent density-functional-theory study of ionization and harmonic generation in CO2 by ultrashort intense laser pulses: Orientational effects,” *Physical Review A*, vol. 81, no. 2, p. 023411, Feb. 2010.

[100] G. Lagmago Kamta and a. Bandrauk, “Effects of molecular symmetry on enhanced ionization by intense laser pulses,” *Physical Review A*, vol. 75, no. 4, p. 041401, Apr. 2007.

[101] T. Zou, S. Chelkowski, and A. D. Bandrauk, “Harmonic generation by the H2+ molecular ion in intense laser fields,” *Phys. Rev. A*, vol. 48, no. 5, pp. 3838–3844, 1993.

[102] R. Karimi, E. Bisson, B. Wales, S. Beaulieu, M. Giguère, Z. Long, W. K. Liu, J. C. Kieffer, F. Légaré, and J. Sanderson, “N2O ionization and dissociation dynamics in intense femtosecond

laser radiation, probed by systematic pulse length variation from 7 to 500 fs.," *The Journal of chemical physics*, vol. 138, no. 20, p. 204311, May 2013.

[103] A. Hishikawa, A. Iwamae, K. Hoshina, M. Kono, and K. Yamanouchi, "Coulomb Explosion Dynamics of N2O in Intense Laser-Field: Identification of New Two-Body and Three-Body Fragmentation Pathways," *Res. Chem. Intermed.*, vol. 24, no. 7, pp. 765–784, Jan. 1998.

[104] M. Ueyama, H. Hasegawa, A. Hishikawa, and K. Yamanouchi, "Concerted and sequential Coulomb explosion processes of N2O in intense laser fields by coincidence momentum imaging.," *The Journal of chemical physics*, vol. 123, no. 15, p. 154305, Oct. 2005.

[105] D. Zeidler, a. Staudte, a. B. Bardon, D. M. Villeneuve, R. Dörner, and P. B. Corkum, "Controlling Attosecond Double Ionization Dynamics via Molecular Alignment," *Physical Review Letters*, vol. 95, no. 20, p. 203003, Nov. 2005.

[106] E. Gibson, A. Paul, N. Wagner, and D. Gaudiosi, "Coherent soft x-ray generation in the water window with quasi-phase matching," *Science*, vol. 302, pp. 95–98, 2003.

[107] S. Haessler, J. Caillat, W. Boutu, C. Giovanetti-Teixeira, T. Ruchon, T. Auguste, Z. Diveki, P. Breger, a. Maquet, B. Carré, R. Taïeb, and P. Salières, "Attosecond imaging of molecular electronic wavepackets," *Nature Physics*, vol. 6, no. 3, pp. 200–206, Jan. 2010.

[108] C. Vozzi, M. Negro, F. Calegari, G. Sansone, M. Nisoli, S. De Silvestri, and S. Stagira, "Generalized molecular orbital tomography," *Nature Physics*, vol. 7, no. 10, pp. 822–826, Jun. 2011.

[109] O. Smirnova, Y. Mairesse, S. Patchkovskii, N. Dudovich, D. Villeneuve, P. Corkum, and M. Y. Ivanov, "High harmonic interferometry of multi-electron dynamics in molecules," *Nature*, vol. 460, pp. 927–977, 2009.

[110] V. V Lozovoy, X. Zhu, T. C. Gunaratne, D. A. Harris, J. C. Shane, and M. Dantus, "Control of molecular fragmentation using shaped femtosecond pulses.," *The journal of physical chemistry. A*, vol. 112, no. 17, pp. 3789–812, May 2008.

[111] R. Itakura, K. Yamanouchi, T. Tanabe, T. Okamoto, and F. Kannari, "Dissociative ionization of ethanol in chirped intense laser fields," *The Journal of Chemical Physics*, vol. 119, no. 8, p. 4179, 2003.

[112] L. J. Frasinski, P. A. Hatherly, and K. Codling, "Multiphoton multiple ionisation of N 2 O probed by three-dimensional covariance mapping," *Physics Letters A*, vol. 156, no. 5, pp. 227–232, 1991.

[113] J. S. Melinger, S. R. Gandhi, A. Hariharan, D. Goswami, and W. S. Warren, "Adiabatic population transfer with frequency-swept laser pulses," *The Journal of Chemical Physics*, vol. 101, no. 8, p. 6439, 1994.

[114] S. Shim, D. Strasfeld, E. Fulmer, and M. Zanni, “Femtosecond pulse shaping directly in the mid-IR using acousto-optic modulation,” *Optics letters*, vol. 31, no. 6, pp. 838–840, 2006.

[115] J. Xia, J. Sanderson, W. K. Liu, and D. Strickland, “Experimental observation of Raman chirped adiabatic rapid passage,” *Journal of Physics B: At. Mol. Opt. Phys.*, vol. 36, no. 03, pp. L409–L414, 2003.